University of Oslo
Department of Physics
Faculty of Mathematics and Natural Sciences

The effects of spatial and temporal oscillations on hydrodynamic dispersion

Ivar Svalheim Haugerud

Spring 2021

Thesis submitted for the degree of Master of Science.

Abstract

As a solute spreads in a flowing liquid, the interplay between advection and diffusion can make the macroscopic dispersion order of magnitude larger than what can be predicted from the molecular diffusivity alone. This has lead to the concept of effective diffusion, which remains essential for describing the transport of pollutants and chemical agents in a wide range of natural systems and industrial applications. The aim of this thesis is to better understand how the macroscopic dispersion is influenced by spatial and temporal oscillations; that is, by spatial periodic modulations of the confining boundary and temporal oscillations in the driving force of the flow. To do so, we build on Brenner's theory of effective diffusion for steady incompressible flow in periodic channels. A discontinuous boundary roughness leads to recirculation zones at all boundary amplitudes, resulting in significantly enhanced dispersion for creeping flow. Contrary to previous research, increasing fluid inertia with rough boundaries is found to be able to both increase or decrease the dispersion depending on the Peclet number; a possible explanation of this phenomenon is proposed. Brenner's theory is generalised to time-dependent velocity fields to investigate single-frequency flow in channels with sinusoidal boundary profiles. A novel resonance phenomenon between the wavelength of the boundary roughness and the frequency of the oscillating driving force is found to maximise the dispersion; a physical explanation is given. Lastly, a reciprocity relation for symmetric transport properties under the reversal of creeping flow was generalised for the purpose of possible medical applications.

Takk

Newton sa en gang: «Hvis jeg har sett lenger, er det fordi jeg har stått på skuldrene til Eirik, Gaute og Knut Jørgen». Det kunne jeg ikke sagt bedre selv, og setter stor pris på alt dere har gjort for å gjøre denne oppgaven mulig. Særlig takk til Gaute for alle givende diskusjoner, og tips og hjelp jeg har fått i løpet av det siste året. (Også takk til Tuva for din deltagelse på møter, og for at du har latt Gaute veilede meg også.)

Takk til alle på PoreLab for at dere tok meg så godt imot da jeg begynte. Jeg kommer til å savne lunsjene, junior-forumene og pianobar med de faglige, og ikke-faglige, diskusjonene med Kristian, Vidar, Beatrice, Jonas og Louison.

Jeg vil også takke, i kronologisk rekkefølge, Oscar, Marlon, Håkon, Sveinung, Astrid, Ylva, Eline, Erlend, Torbjørn, Metin, og Cecilie for alle de hyggelige minnene etter fem år på Blindern. Tiden her ville ikke vært den samme uten dere. Lisa fortjener en stor takk for at hun har klart å gjøre et år med Korona og masterjobbing veldig fint.

Til slutt vil jeg takke familien min for at dere har hjulpet meg med alt mulig rart gjennom studiet, og for å ha gitt meg avbrekk fra livets kjas og mas. Og helt til slutt vil jeg takke lånekassen for å ha støttet meg gjennom hele studietiden, jeg står i stor gjeld overfor dere.

Contents

Abstract **iii**

Acknowledgments **v**

Contents **vi**

1 Introduction **1**

2 Theory **5**
2.1 Fluid dynamics . . . 5
2.1.1 The continuity equation . . . 6
2.1.2 Euler's equation and ideal fluids . . . 6
2.1.3 The Stokes equation and creeping flow . . . 7
2.1.4 The Navier–Stokes equations and the Reynolds number . . . 9
2.1.5 Stokes drag . . . 10
2.2 Non-equilibrium systems . . . 11
2.2.1 The Langevin equation . . . 11
2.2.2 The Fokker–Planck equation . . . 13
2.3 Advection-diffusion and effective diffusion coefficients . . . 15
2.3.1 Deriving the advection-diffusion equation . . . 15
2.3.2 Reciprocal relation for advection-diffusion . . . 17
2.3.3 Taylor–Aris dispersion . . . 18
2.3.4 Brenner's theory . . . 19

3 Numerical Methods **25**
3.1 The lattice-Boltzmann method . . . 25
3.1.1 Fundamentals . . . 26
3.1.2 Initialization and boundary conditions . . . 28
3.1.3 Updating scheme . . . 28
3.1.4 Simulating the advection-diffusion equation . . . 30
3.2 The finite element method . . . 31
3.2.1 Simple example . . . 32
3.2.2 More complicated equations . . . 34
3.2.3 FEniCS . . . 34

3.2.4 Time dependent equations . . . 35
3.2.5 Structure of program . . . 36
3.2.6 Comparison between the LBM and the FEM . . . 36
3.3 Random walks to simulate the advection-diffusion equation . . . 37

4 Results and Discussion **39**
4.1 Dispersion in channels with rough square boundary . . . 39
4.1.1 Velocity field . . . 40
4.1.2 Validation of Brenner solver . . . 40
4.1.3 Effective dispersion for creeping flow . . . 43
4.1.4 Effective dispersion for inertial flow . . . 44
4.1.5 Random walk analysis . . . 44
4.1.6 Discussion . . . 48
4.2 Dispersion with an oscillating force in channels with sinusoidal boundary . . . 54
4.2.1 Perturbation theory and time-dependent Brenner equations . . . 54
4.2.2 Velocity fields and pressure . . . 57
4.2.3 Comparison with numerical solutions . . . 59
4.2.4 Zeroth-order effective diffusion coefficient . . . 62
4.2.5 Contributing terms to higher-order effective dispersion . . . 65
4.2.6 First-order Brenner field . . . 66
4.2.7 Second-order Brenner field . . . 68
4.2.8 Numerical solutions of Brenner's equations . . . 69
4.2.9 Semi-analytic solutions for the effective diffusion coefficient . . . 75
4.2.10 Discussion . . . 76
4.3 Reciprocal relation for reversible flow . . . 83
4.3.1 Diffusion of matter versus diffusion of heat . . . 83
4.3.2 Optimizing injection method . . . 85
4.3.3 General injection methods . . . 86
4.3.4 Reciprocal relation for different transport scaling . . . 88
4.3.5 Reciprocal relation for time-dependent flow . . . 88
4.3.6 Symmetry of dispersion tensor under reversal of flow . . . 90
4.3.7 Discussion and possible applications . . . 92

5 Conclusion **95**

Appendicies **98**

A Derivation of time-dependent Brenner theory **101**

Bibliography **104**

Chapter 1

Introduction

From a sharp peak to uniformity, a solute injected into a flowing solvent evolves from one state of simplicity to another. In the irreversible transition between the extremal states, advection and diffusion work inseparably together to create complex behaviour and patterns. The diffusive spreading arises from the stochastic trajectories of the constituent particles, originating from microscopic collisions with the surrounding thermal fluid, independent of the bulk movement. External forces and pressure gradients result in the complicated dynamics of the encompassing fluid, which advects the solute along with its motion. After a sufficiently long time, the dispersion reaches its asymptotic regime, where the positional variance of the solute grows linearly in time. The proportionality is quantified by the dispersion tensor, which has become the standard for describing solute spreading in systems where the interplay of advection and diffusion is important, with applications ranging from the study of transport in blood [1–3] and groundwater systems [4, 5], sugar transport in plants [6–8], drug delivery [9–12], spreading of plastic in oceans [13–15], to the highly relevant dispersion of airborne droplets for spreading in disease transmission [16–18]. Therefore, dispersion has been the focus of much experimental, numerical and theoretical research. In Taylor's theory to calculate the effective diffusion [19], and Aris' [20] generalization, the flow field is assumed to be both stationary and axially invariant. However, most channels and pores in natural and industrial systems are not perfectly flat and many flows are unsteady and time-dependent, resulting in significant consequences for the dispersion [21–24].

The overarching goal of this thesis is to gain a better understanding of dispersion phenomena in complex geometries. In particular, using numerical and theoretical methods, we will investigate how spatial and temporal inhomogeneities influence the spreading dynamics and possibly lead to new mechanisms for dispersion. The goal will be reached by addressing three main research questions:

1: What is the role of a discontinuous boundary roughness for the dispersion in channel flow?

Most previous work on the effect of geometry has been done on smoothly varying aperture while neglecting fluid inertia. Bolster et al. [25] studied the dispersion of solutes in

channels with sinusoidal wall roughness under creeping flow conditions, using the method of moments. Here, the linearity of Stokes' equations and the analyticity of the boundary allowed for a perturbative approximation to the dispersion coefficient. Bouquain et al. [26] extended this work by investigating the effects of fluid inertia on the effective solute transport. Inertial effects are of both practical and theoretical interest, as they can result in low-velocity regions with self-connected streamlines, called recirculation zones (RZ). The RZ can trap the solute, resulting in significant consequences on the asymptotic dispersion. While RZ can occur in Stokes flow, they become more dominant with increasing fluid inertia and occur for much smaller geometrical constraints. From direct numerical simulations and experiments, it is well-known that flow behind a backwards-facing step, similar to the discontinuities of interest here, creates large recirculation zones [27]. Although the smooth single-wavelength roughness considered in Refs. [25, 26] represent a major step towards real-world applications, the wall roughness found in both natural rock fractures [28–30], soil [31, 32], diffusion-limited reactions [33, 34] and microfluidic devices [35, 36], such as the staggered herringbone mixer [37–39], do not obey the same smoothness, but contain jumps and often rugged shapes. Yoon et al. [30] recently applied random walk simulations to investigate the combined effect of a self-similar roughness and fluid inertia for a variety of advective transport rates, but their investigation never reached the asymptotic regime. In the absence of advection, smooth boundaries contribute a negative term linear in the boundary amplitude to the effective diffusion. This is in contrast to rough boundaries, which contribute quadratically [40]. Despite the ubiquity of rough surfaces, it is unclear exactly how fluid flow, especially with high inertia, will interplay with the discontinuous boundary roughness to influence the effective dispersion. The investigation of this research question is mainly numerical, using the finite element method (FEM) to solve Brenner's equations [41, 42], as the discontinuous geometry makes the perturbative approach prohibited. The goal is to find and understand the effective diffusion coefficient's dependency on the boundary amplitude, different advective and diffusive transport rates, and fluid inertia, in a channel with a periodic rough square boundary. The geometry is used as a simplified representation of generic rough walled channels that contain sharp notches and grooves of various sizes, e.g. discontinuous jumps in the boundary profile.

2: How does an oscillating driving force and boundary roughness interplay to influence the dispersion behaviour?

Unsteady flows contain more shear than their steady counterpart, increasing the mass transfer [43–46], and are therefore commonly applied to e.g. microfluidic devices and lab-on-a-chip technology [47, 48]. However, little theoretical modelling has been done on the topic, resulting in a lack of quantitative and physical understanding. Vedel et al. [43] found a closed-form analytical expression for the effective diffusion coefficient in a straight two-dimensional channel where the flow could consist of a general spectrum of frequencies, in agreement with experimental measurements. Pure experimental investigations have also been made for a broad range of single-frequency flow in flat channels [49]. This work, together with other research on single frequency flows in the transient regime with flat boundaries [22, 50, 51], has given a good understanding of dispersion with oscillating

flow. Still, the combined effect of a pulsating velocity field in a channel with varying aperture, which on its own is known to have drastic consequences on the dispersion, has to our knowledge not been studied. An investigation of the consequences of geometry should therefore be made for such flows. Additionally, dispersion in naturally occurring systems like transport in the lungs [52], air turbulence-induced oscillating flow in soil [53], nutrition transport in bone subject to oscillatory mechanical loading [21], and transfer of mass in polymer solutions [54] can exhibit both a varying boundary and an oscillating flow. This will be investigated for a sinusoidal boundary, which might result in richer dynamics, with interactions between the frequency of the fluid, the wavelength of the boundary, and the molecular diffusivity. The main goal of the investigation is to analyse and understand the combined effect of a varying boundary and an oscillating flow on the effective diffusion coefficient, and search for novel phenomena in the dispersion behaviour. To understand the system, we investigate it both analytically and numerically. A major stepping stone to this end is that Brenner's theory, hitherto only valid for steady flows, is generalised to time-dependent flows for the purpose of our investigation. A perturbative solution for a sinusoidally varying channel aperture is developed and benchmarked against a full numerical finite-element solution. This investigation will act as a first step towards establishing the laws of dispersion for time-dependent flow in rough geometries.

3: Can the reciprocal relation for hydrodynamic dispersion be extended to account for realistic injection scenarios?

Lastly, a general symmetric transport property on the form of a reciprocity relation for dispersion is investigated. For reversible creeping flow, the reciprocal relation [55] allows for the prediction of a concentration at a specific point in the fluid. A generalisation of previous work [55] on this relationship is investigated analytically and compared with numerical simulations using the lattice-Boltzmann method (LBM). The relation is relevant for medical applications, as it can be used to access and optimise the predicted concentration profile of, for example, chemotherapeutic agents in the context of cancer treatment at an otherwise inaccessible region [55]. Therefore, the generalisations are made with the goal of extending the applicability of the relation with such motivations in mind.

The outline of this thesis is as follows. To model hydrodynamic dispersion, the relevant aspects of fluid dynamics and non-equilibrium statistical mechanics are presented in chapter 2, where they are combined to derive the central equation of this thesis, the advection-diffusion equation. The lattice-Boltzmann and finite element methods used to model, simulate, and solve the presented theory are described in the following chapter. In chapter 4, the numerical and analytic results from each area of investigation are presented and discussed separately before general conclusions are drawn in the last chapter.

Chapter 2

Theory

This chapter introduces the relevant theoretical background for the thesis. We start with the continuum theory of fluid dynamics, ultimately deriving the Navier-Stokes equations and investigating the viscous drag force on a sphere moving through a fluid with a constant velocity. Throughout the thesis, the Navier-Stokes equations are used for finding the flow field governing the dispersion and are therefore of central importance. The microscopic theory of non-equilibrium systems is then discussed, beginning with the stochastic differential equation called the Langevin equation and its relation to the macroscopic viewpoint through the Fokker–Planck equation. Lastly, the hydrodynamics of Stokes drag and statistical mechanics of the Langevin and Fokker–Planck equation is combined to ultimately derive the advection-diffusion equation. Brenner's theory, which gives a general theoretical framework for calculating the effective diffusion coefficient in periodic environments, is derived and discussed.

2.1 Fluid dynamics

Fluid dynamics concerns itself with the macroscopic description of fluids. An arbitrary small volume on the macroscopic scale will always contain a large number of molecules, such that the fluid can be regarded as a continuum. The infinitesimal volume elements $\mathrm{d}V$ or surface elements $\mathrm{d}\boldsymbol{S}$ are therefore not infinitely small, but much smaller than the fluid under consideration, yet much larger than the distance between the molecules. Hence, the theory can be derived completely independently from any microscopic description or notion of atoms, although bottom-up approaches exist. To completely describe a fluid mathematically we need a function describing the fluid velocity $\boldsymbol{u}(\boldsymbol{r}, t)$, and a thermodynamic quantity spanning the fluid; either the pressure $P(\boldsymbol{r}, t)$ or the density $\varrho(\boldsymbol{r}, t)$. Combining this with an equation of state fully describes all fluid properties. The fluid is described in spatial coordinates $\boldsymbol{r}$, at a time t, where the position $\boldsymbol{r}$ is not following the fluid flow, but is fixed in a reference frame independent of the fluid.

In this section, the fundamental equations of fluid dynamics, which will be used throughout the thesis, are derived. For a more detailed description, I refer to the book *Fluid Mechanics* by Landau and Lifshitz [56], as their derivation will be followed.

2.1.1 The continuity equation

The mass contained inside an arbitrary region of space with volume V_0 is given by a volume integral over the density $\int_{V_0} \mathrm{d}V\,\varrho$. Mass flowing out of this region must pass through a small part of the total surface $\mathrm{d}\boldsymbol{S}$. The magnitude of the surface elements is the infinitesimal surface area, and direction is the surface norm. The fluid mass passing through this infinitesimal area per unit time, $\varrho\boldsymbol{u}\cdot\mathrm{d}\boldsymbol{S}$, is positive if the mass is flowing out of the volume. To find the net mass passing through the total surface area per unit time, we integrate this quantity over the surface area $\oint_{\partial V_0}\mathrm{d}\boldsymbol{S}\cdot\varrho\boldsymbol{u}$. Mass flux through the volume surface must result in a change of mass inside the volume, and can therefore be equated with the time derivative of the total mass

$$\partial_t \int_{V_0} \mathrm{d}V\,\varrho = -\oint_{\partial V_0} \mathrm{d}\boldsymbol{S}\cdot\varrho\boldsymbol{u}, \tag{2.1}$$

where the sign originates from our convention for the normal vector. By applying Gauss' law the surface integral is transformed to a volume integral

$$\partial_t \int_{V_0} \mathrm{d}V\,\varrho = -\int_{V_0} \mathrm{d}V\ \boldsymbol{\nabla}\cdot(\varrho\boldsymbol{u})\,. \tag{2.2}$$

We have not specified any properties of the volume, and the equality must therefore hold for an arbitrary choice of volume. Therefore, the terms inside each integral exactly equal each other

$$\partial_t\varrho + \nabla\cdot(\varrho\boldsymbol{u}) = 0. \tag{2.3}$$

This is the continuity equation, which describes the conservation of mass, and is one of the fundamental equations of fluid dynamics.

For many fluids, the density is approximately constant throughout the entire fluid volume during its motion; there is no compression or expansion of the fluid. The continuity equation then takes the simplified form

$$\nabla\cdot\boldsymbol{u} = 0. \tag{2.4}$$

Fluids satisfying this relation are called incompressible and equation (2.4) is a good approximation for most liquids, and even gases when the velocity is much smaller than the speed of sound [56].

2.1.2 Euler's equation and ideal fluids

Let us further consider the effects of external body forces $\boldsymbol{f}$ and pressure P on our general volume V_0. The total force $\boldsymbol{F}$ acting on the fluid is given by the volume integral of the body force, in addition to pressure differences across the volume

$$\boldsymbol{F} = \int_{V_0} \mathrm{d}V\,\varrho\boldsymbol{f} - \oint_{\partial V_0} P\,\mathrm{d}\boldsymbol{S} = \int_{V_0} (\varrho\boldsymbol{f} - \nabla P)\ \mathrm{d}V, \tag{2.5}$$

where the last equality is found from applying Gauss' law. Applying Newton's second law for the fluid element gives

$$\varrho \frac{\mathrm{d}\boldsymbol{u}}{\mathrm{d}t} = -\nabla P + \varrho \boldsymbol{f}. \tag{2.6}$$

By performing a volume integral on both sides, the standard form of Newton's second law is retrieved. The time derivative of the fluid velocity does not represent the rate of change at a fixed spatial point, but the rate of change for a specific fluid particle. To express the quantity in terms of fixed spatial coordinates, the total infinitesimal change is decomposed

$$\mathrm{d}\boldsymbol{u} = \partial_t \boldsymbol{u}\, \mathrm{d}t + \mathrm{d}\boldsymbol{r} \cdot \nabla\, \boldsymbol{u}. \tag{2.7}$$

The first term gives the change in velocity over time at a fixed point in space. While the second term represents the velocity difference between two points separated by the distance $\mathrm{d}\boldsymbol{r}$ traveled by the fluid particle during the time $\mathrm{d}t$. Dividing both sides by $\mathrm{d}t$, we find the material derivative

$$\frac{\mathrm{d}\boldsymbol{u}}{\mathrm{d}t} = \partial_t \boldsymbol{u} + \boldsymbol{u} \cdot \nabla\, \boldsymbol{u}. \tag{2.8}$$

Thus, Newton's second law for the fluid element takes the form

$$\partial_t \boldsymbol{u} + \boldsymbol{u} \cdot \nabla\, \boldsymbol{u} = -\frac{1}{\varrho} \nabla P + \boldsymbol{f}. \tag{2.9}$$

This is the second fundamental equation of fluid dynamics, known as Euler's equation. When deriving the equation, we have not taken the dissipation of energy through friction into account, which must be included for a complete description of the fluid. The internal friction arises from adjacent fluid layers moving relative to each other, and is quantified by the fluid viscosity. Fluids where the internal friction is negligible, meaning a small viscosity, are called ideal fluids.

In this thesis, we will not cover ideal fluids and therefore continue by deriving the viscosity's effect on the equation of motion.

2.1.3 The Stokes equation and creeping flow

Energy dissipation in a moving fluid is a consequence of the thermodynamic irreversibility of the fluid motion and is always present to some extent. To derive its effect, additional terms must be included in the equation of motion. By defining the momentum flux density tensor as the symmetric second-rank tensor

$$\Pi_{ik} = P\delta_{ik} + \varrho u_i u_k, \tag{2.10}$$

Euler's equation takes on the simplified form

$$\partial_t \left(\varrho v_i\right) = -\partial_{x_k} \Pi_{ik}, \tag{2.11}$$

where the external force f_i is excluded, and Einstein notation is implied. This equation describes the completely reversible momentum flux inside the fluid due to pressure gradients and mechanical transport of particles. The internal friction causes an additional term

describing the diffusive transfer of momentum from regions of high velocity to low velocity. This irreversible viscous transfer of momentum is included by adding a term called the viscous stress tensor σ'_{ik} to the momentum flux density tensor. From this, we can further define the stress tensor as

$$\sigma_{ik} \equiv -P\delta_{ik} + \sigma'_{ik}, \qquad \Pi_{ik} = \varrho u_i u_k - \sigma_{ik}. \tag{2.12}$$

The stress tensor describes the part of the momentum flux not due to advective transport. To find the equation of motion, the stress tensor must be established.

The internal friction of the fluid occurs due to different fluid particles, or fluid layers, moving relative to one another. Hence, the energy dissipation must depend on the spatial velocity gradients. Assuming small velocity gradients, a Taylor expansion to linear order can be made. There cannot be any constant terms as the friction must disappear for a constant velocity field. In addition, it must vanish under uniform rotation of angular frequency $\boldsymbol{\Omega}$, where $\boldsymbol{u} = \boldsymbol{\Omega} \times \boldsymbol{r}$. The most general rank two tensor satisfying the two criteria is given by

$$\sigma'_{ik} = \mu \left(\partial_{x_k} u_i + \partial_{x_i} u_k - \frac{2}{3}\delta_{ik}\partial_{x_l} u_l \right) + \zeta \delta_{ik} \partial_{x_l} u_l. \tag{2.13}$$

For an isotropic fluid, the coefficients of viscosity, μ and ζ, become constant and are assumed to be independent of the fluid velocity. It can further be shown [56] that they are both positive; $\mu > 0$ and $\zeta > 0$. The strange arrangement of different factors is made such that the left term of the tensor vanishes upon contracting the indices.

When the viscosity dominates over the inertia of the fluid, as will be explained in more detail later, we only need to include the stress tensor and external forces in the equation of motion

$$\nabla_i \sigma'_{ik} + f_k = 0. \tag{2.14}$$

Using the most general form of the stress tensor, the equation takes the form

$$\mu \nabla^2 \boldsymbol{u} + \left(\zeta + \frac{1}{3}\mu \right) \nabla \left(\nabla \cdot \boldsymbol{u} \right) + \boldsymbol{f} = \nabla P, \tag{2.15}$$

where constant coefficients of viscosity has been assumed. Combined with the incompressability equation (2.4), the above relation reduces to what is known as the Stokes equations

$$\mu \nabla^2 \boldsymbol{u} + \boldsymbol{f} = \nabla P, \tag{2.16}$$

which is another of the fundamental equations of fluid dynamics. The equation is simpler to solve than Euler's equation, and still has some interesting properties. Due to the lack of time derivatives there is no memory in the flow; if you stop pushing, the fluid will instantaneously respond. In addition, the flow is reversible, due to the fact that a change of sign in the force results in a sign change of the velocity field

$$\boldsymbol{f} \to -\boldsymbol{f} \qquad \Longrightarrow \qquad \boldsymbol{u} \to -\boldsymbol{u}. \tag{2.17}$$

Reversing the evolution of the pressure and forces result in the reversal of the flow, which can result in difficulties in mixing and swimming. For a further discussion on Stokes flow's strange or counter-intuitive properties, see Purcell's classical paper *Life at low Reynolds number* [57].

2.1.4 The Navier–Stokes equations and the Reynolds number

The full description of the fluid is found by including both Euler's and Stokes's contribution to the equation of motion simultaneously. This results in the Cauchy momentum equation, which describes all non-relativistic fluid phenomena at the macroscopic scale,

$$\varrho\left(\partial_t \boldsymbol{u} + (\boldsymbol{u}\cdot\nabla)\,\boldsymbol{u}\right) = -\nabla P + \mu\nabla^2\boldsymbol{u} + \left(\zeta + \frac{1}{3}\mu\right)\nabla\left(\nabla\cdot\boldsymbol{u}\right) + \boldsymbol{f}. \tag{2.18}$$

Most fluids, and all the fluids investigated in this thesis, can be regarded as incompressible [56], simplifying the equation greatly:

$$\varrho\left(\partial_t \boldsymbol{u} + (\boldsymbol{u}\cdot\nabla)\,\boldsymbol{u}\right) = -\nabla P + \mu\nabla^2\boldsymbol{u} + \boldsymbol{f}. \tag{2.19}$$

The above equation, combined with the continuity equation (2.3), are the Navier–Stokes equations (NSE). To uniquely determine a solution, the no-slip boundary condition is employed, meaning the velocity field is stationary on the boundary

$$\boldsymbol{u} = 0 \quad \text{on} \quad \partial\Omega, \tag{2.20}$$

which will be used throughout the thesis. For an incompressible fluid, the density ϱ and dynamic viscosity μ are the only free parameters of the fluid. The ratio between the two characterizes the fluid and defines the kinematic viscosity

$$\nu \equiv \frac{\mu}{\varrho}, \tag{2.21}$$

which shares the units of a diffusion coefficient. The kinematic viscosity represents the diffusion coefficient for the momentum of the fluid. The NS equation also contains the two unknowns functions, the pressure P/ϱ, and the velocity field, $\boldsymbol{u}$, with an average value U. Additionally, the shape and size of the geometry appear through the boundary conditions acting on the fluid. Let us suppose that the geometrical shape of the boundary is given, such that it is quantified by a single characteristic length l. One can show, using Buckingham's pi theorem, that there is only one dimensionless quantity that can be formed using the three parameters, which we call the Reynolds number

$$\mathrm{Re} \equiv \frac{\varrho l U}{\mu} = \frac{lU}{\nu}. \tag{2.22}$$

Flows with different viscosities and characteristic lengths that scale to the same Reynolds number are called *similar*. Similar flows are identical when written in terms of dimensionless quantities. This can easily be seen by expressing all factors in the NS equation by their characteristic value,

$$\mathrm{Re}\left(\partial_t \boldsymbol{u} + (\boldsymbol{u}\cdot\nabla)\,\boldsymbol{u}\right) = -\nabla P + \nabla^2\boldsymbol{u} + \boldsymbol{f}, \tag{2.23}$$

such that all parameters are dimensionless. Thus, if the Reynolds number is the same, the flow in its natural units is the same. We see that the Stokes equation is found for low

Reynolds number and Euler's equation for large Reynolds number, where the pressure and force need to be matched in each limit. At large values of the Reynolds number, inertial effects become important, and different parts of the fluid will move at different speeds and in different directions. This can ultimately result in parts of the fluid moving in the opposite direction of the overall flow, creating eddies or recirculation zones, dissipating kinetic energy. This type of fluid motion is no longer necessarily moving in layers and is therefore no longer laminar, but chaotic and aperiodic, meaning turbulent. The other limit exhibits the same properties discussed for the Stokes equation and is called creeping flow.

For non-steady flows, we get a second dimensionless number, in addition to the Reynolds number, called the Womersley number

$$\mathrm{Wo} \equiv \sqrt{\frac{\omega l^2}{\nu}}, \tag{2.24}$$

where ω is now the characteristic frequency of the flow. The Womersley number compares the time-scale of the external force, to the time-scale of the fluid response through momentum diffusion. For the velocity field to be similar for such flows, both the Reynolds and Womersley number must be the same. At low values of the Womersley number, the flow frequency is small enough for the momentum to diffuse to equilibrium at each time-step, such that the flow is reversible and in phase with the oscillating pressure gradient. For flow in channels, this results in Poiseuille flow multiplied by a factor oscillating in time. In the other limit, the frequency is large compared to the response time of the fluid, making the flow non-reversible and history-dependent. The flow is now out of phase with the pressure gradient and does not have time to develop fully. From the Womersley and Reynolds number, one can define the Strouhal number

$$\mathrm{St} \equiv \frac{l\omega}{U}, \tag{2.25}$$

relating the characteristic length to the advection length over a period.

2.1.5 Stokes drag

The Navier–Stokes equations can be exploited to find the velocity field around a spherical particle moving at a constant velocity relative to the fluid. For low Reynolds number, one can solve the Stokes equation (2.16) by assuming an incompressible flow (2.4). The velocity field at the boundary of the spherical particle must be zero (2.20), and the far-field flow is assumed to be unaffected by the particle, such that it is equal to a constant vector $\boldsymbol{v}$, in the particle's frame. Using the viscous stress tensor from equation (2.13), the total force acting on the spherical particle can be calculated by solving the surface integral over the sphere's boundary

$$\boldsymbol{F} = \oint_{\partial V} \mathrm{d}\boldsymbol{S} \cdot \boldsymbol{\sigma} = 6\pi\mu a \boldsymbol{v}, \tag{2.26}$$

where a is the radius of the sphere. The velocity vector $\boldsymbol{v}$ can either be interpreted as the particle's velocity or the velocity of the fluid in the particle's frame. The prefactor is often referred to as the drag coefficient:

$$\gamma \equiv 6\pi\mu a. \tag{2.27}$$

The advection-diffusion equation will later be derived for a particle subject to Stokes flow with a drag coefficient γ.

2.2 Non-equilibrium systems

The previous section concerned itself with a continuum description of fluids, where the individual particles and fluctuations are coarse-grained to continuous, non-fluctuating quantities. However, on smaller scales, the fluid can no longer be regarded as a continuum, and molecular fluctuations of the fluid will affect the dynamics of suspended particles. The Langevin approach models the fluctuations by adding noise terms in the equation of motion. Despite the fact that the fluctuating fluid can be described exactly by finding the trajectories of all the constituent particles, the approach contains too many irrelevant degrees of freedom. Therefore, we are not interested in a single realization of the fluctuating force and the resulting trajectories, but ensemble averages of many different realizations. The ensemble average can either be interpreted as performing the same experiment multiple times, or having one experiment with many particles which are far enough apart not to influence one another. Independently of the interpretation, the statistical properties of the noise have to be determined to relate the microscopic dynamics to the macroscopic observables. The Langevin equation and the Fokker–Planck equation give a physical explanation for diffusion phenomena and relate it to macroscopic observables. Combining both equations with the Navier-Stokes equations, they will later be applied to derive the central equation in this thesis, namely the advection-diffusion equation.

2.2.1 The Langevin equation

A particle immersed in a fluid will experience a frictional force, which can in its simplest form be modelled by the Stokes drag,

$$m\dot{v} = -\gamma v, \tag{2.28}$$

where γ is the friction coefficient (2.27). Although this equation is written for a one-dimensional system, the investigation can be extended to multiple dimensions. The solution of this equation gives the deterministic behaviour of the particle, whose velocity will be exponentially damped to zero from its initial value. This description is only valid when the particle's mass m is large enough for thermal fluctuations to be negligible. From the equipartition theorem [58], the thermal velocity is related to the fluid temperature T

$$\frac{1}{2}m\langle v^2\rangle = \frac{1}{2}k_B T, \tag{2.29}$$

where k_B is Boltzmann's constant. The thermal velocity of $\sqrt{k_B T/m}$ becomes relevant when its magnitude is similar to that of the particle's velocity. For such cases, the deterministic description (2.28) is not correct, and the thermal noise must be included in the model. In the Langevin equation, this is done by including a random force $\xi(t)$ on the particle

$$m\dot{v} = -\gamma v + \xi(t). \tag{2.30}$$

For the Langevin equation to be useful, the probabilistic properties of the noise term have to be determined. To do so, we will give three postulates and argue for why these are sensible from a physical standpoint. First, ξ is irregular and undetermined, but we can give definite statements about its ensemble average over many different realizations. It can therefore be treated as a stochastic process. Secondly, the properties of ξ are independent of v and act as an external force whose ensemble average vanishes $\langle \xi \rangle = 0$. Lastly, since the noise originates from collisions with individual fluid molecules, it must be history independent and vary rapidly,

$$\langle \xi(t)\xi(t') \rangle = \Gamma \delta(t - t'), \tag{2.31}$$

where Γ is a constant. The postulates can be summarized as the collisions being effectively instantaneous, uncorrelated and with no preferred direction. Here, instantaneous means much shorter than all other relevant time scales. When ξ satisfies the above properties, it is called a Langevin force [59]. Equivalently, since the noise results from many independent collisions, it follows from the central limit theorem that it must be Gaussian [60]. Additionally, any Gaussian variable is uniquely defined by its first two moments [59], such that the postulates above uniquely defines a Gaussian distribution.

The Langevin equation (2.30) can be solved exactly by multiplying both sides with $e^{\gamma t}$, and integrating over time, yielding

$$v(t) = v_0 e^{-\gamma t} + \int_0^t \mathrm{d}t' \xi(t') e^{-\gamma(t-t')}, \tag{2.32}$$

where the mass is set to unity without loss of generality. By taking the ensemble average of $v(t)$, the second term, representing the change in velocity due to the stochastic force from the fluid, disappears. We are therefore left with an exponential decay of the initial velocity. Another quantity of interest is the velocity autocorrelation function, found from squaring the above expression, taking the ensemble average and solving the integral:

$$\langle v^2(t) \rangle = v_0^2 e^{-2\gamma t} + \frac{\Gamma}{2\gamma} \left[1 - e^{-2\gamma t} \right], \tag{2.33}$$

where we have used the properties of the noise from equation (2.31). After a sufficiently long time, $t \gg 1/\gamma$, initial conditions become unimportant, and the velocity autocorrelation function is $\Gamma/2\gamma$. Equating this with the equipartition theorem (2.29) gives a value of the noise in terms of measurable physical quantities

$$\Gamma = 2\gamma k_B T. \tag{2.34}$$

Another quantity of interest is the mean-squared displacement, which we can calculate by performing a time integral over the velocity correlation function using (2.32)

$$\langle (x(t) - \langle x \rangle)^2 \rangle = \int_0^t \mathrm{d}t_1 \int_0^t \mathrm{d}t_2 \langle v(t_1) v(t_2) \rangle. \tag{2.35}$$

Solving this integral and using the value of γ from Stokes drag (2.27), gives a linear asymptotic time scaling of the positional variance, often referred to as the mean square displacement,

$$\langle (x(t) - \langle x \rangle)^2 \rangle \propto \frac{k_B T}{3\pi\mu a} \equiv 2D_m t, \tag{2.36}$$

where we have ignored all exponentially decaying terms. This relation is a fluctuation-dissipation relation, known as an Einstein relation, which defines the molecular diffusion coefficient D_m. The temperature of the fluid causes fluctuation in its constituent molecules, which gives rise to the stochastic movement of the particle. The particle then heats the fluid by dissipating its kinetic energy through fluid friction. The fluctuation-dissipation relation gives the non-equilibrium steady state between the particle and the fluid heat bath. Here we found that the mean square displacement grows linearly in time, and the diffusion coefficient yields the associated proportionality constant. In certain systems, the mean square displacement instead grows as t^α. Processes with $\alpha < 1$ are called subdiffusive, and a value of α between one and two are superdiffusive. Exponents larger than two is coined hyperballistic superdiffusion [61].

2.2.2 The Fokker–Planck equation

The stochastic nature of the Langevin equation emerges solely due to the fluctuating force. Taking the expectation value can then be interpreted as taking an average over many different realizations of the force, which we do not want to deal with explicitly. With this interpretation in mind, one can take the kinetic theory approach, and instead of finding the mechanical trajectory for a single realization of ξ, one can aim to find the evolution of a probability distribution function $P(\boldsymbol{x}, t)$. The probability distribution function is a probability density, such that $P(\boldsymbol{x}, t)\mathrm{d}^3\boldsymbol{x}$ gives the probability of finding the particle at a given position $\boldsymbol{x}$ at a time t, within the infinitesimal volume $\mathrm{d}^3\boldsymbol{x}$ centered at $\boldsymbol{x}$. The dynamics of the probability distribution is governed by a transition rate $W(\boldsymbol{x}'|\boldsymbol{x})$, which represents the transition probability from $\boldsymbol{x}$ to $\boldsymbol{x}'$ per volume per unit time. The instantaneous collisions with the fluid occur on too short time scales to be observed in the probabilities, and one expects the probability density to vary smoothly. The derivation performed here will follow a combination of standard literature on the topic: *The Fokker–Planck Equation* by Risken [62], *Non-equilibrium statistical physics* by Livi [63] and a review article on stochastic processes by Garcia [64].

Fokker and Planck originally proposed that the evolution of P can be written as a master equation [63], where the change in probability density is given by the difference in transition rates towards and away from x

$$\partial_t P(x,t) = \int \mathrm{d}^3x' \ \left[P(x',t)W(x|x') - P(x,t)W(x'|x)\right]. \tag{2.37}$$

The integral must be evaluated over the whole accessible space of the variable x, which does not necessarily represent the particle's position. Our derivation will be done for a scalar variable x, but can be extended to vectors, see for example Garcia [64]. We want a differential equation for the probability density instead of its current integro-differential

form. To do so, we perform a Taylor expansion of the transition rates. Since the transition rates over large distances should be infrequent, it is reasonable to assume that the transition rates decay rapidly to zero, from a non-zero value close to the initial position. This expansion can be performed in the parameter $\Delta \equiv x - x'$, and is called the Kramers–Moyal expansion [63]. To simplify the notation, we define

$$W(x|x') = W(x' + \Delta|x') \equiv W_\Delta(x') \quad \text{and} \quad W(x'|x) = W(x - \Delta|x) \equiv W_{-\Delta}(x), \tag{2.38}$$

such that the master equation takes the form

$$\partial_t P(x,t) = \int \mathrm{d}^3\Delta\, P(x',t) W_\Delta(x') - P(x,t) \int \mathrm{d}^3\Delta\, W_{-\Delta}(x). \tag{2.39}$$

We have limited our derivation to the case where the boundary terms are irrelevant, and vanish upon our coordinate transformation. With our assumption we can Taylor expand the transition probabilities of the first integral in our equation

$$\int \mathrm{d}^3\Delta P(x',t) W_\Delta(x') = P(x,t) \int \mathrm{d}^3\Delta\, W_\Delta(x) + \sum_{n=1}^{\infty} (-1)^n \frac{1}{n!} \partial_x^n \left[a^{(n)} P \right](x). \tag{2.40}$$

Where the $a^{(n)}$'s are the Moyal coefficients, sometimes referred to as jump moments

$$a^{(n)} \equiv \int \mathrm{d}^3\Delta\, W_\Delta(x) \Delta^n. \tag{2.41}$$

The first integral term of our expansion will cancel with the last term in the master equation upon a coordinate transformation, by changing the sign of Δ, and again using that the boundary terms vanish. This results in the Kramer-Moyal expansion of the master equation

$$\partial_t P(x,t) = \sum_{n=1}^{\infty} (-1)^n \frac{\Delta^n}{n!} \partial_x^n \left[a^{(n)} P \right](x). \tag{2.42}$$

Currently this description is completely equivalent to the the master equation. The Pawula theorem [62] states that if the Kramers-Moyal expansion continues further than to second order, infinitely many terms have to be included for the solution to satisfy the properties needed of a probability density. It is therefore a natural to choose to truncate the expansion at the second order, resulting in the celebrated Fokker–Planck equation

$$\partial_t P(x,t) = -\partial_x \left[a^{(1)} P \right](x,t) + \frac{1}{2} \partial_x^2 \left[a^{(2)} P \right](x,t). \tag{2.43}$$

The first and second term is called the drift and diffusion term, with $a^{(1)}$ and $a^{(2)}$ being respectively called the drift and diffusion coefficients. To solve for the evolution of the probability density, the coefficients must be determined. We do this by expressing the integral in equation (2.41) in terms of the coordinates instead of the relative distance

$$a^{(n)} = \int \mathrm{d}x' W(x'|x) \left(x' - x\right)^n. \tag{2.44}$$

For short timesteps τ, the transition probability density can approximately be written as [64]

$$P(x', t+\tau|x, t) = \delta(x'-x)\left(1 - a^{(0)}(x,t)\tau\right) + W(x'|x,t)\tau + \mathcal{O}(\tau^2), \tag{2.45}$$

where the first term gives the probability of the transition not taking place during the time interval τ, and the second term that it does take place. This rewrite can be solved for the transition probability $W(x'|x)$, such that the Moyal coefficient can be written as

$$a^{(n)} = \frac{1}{\tau}\int \mathrm{d}x' P(x', t+\tau|x,t)\left(x'-x\right)^n. \tag{2.46}$$

Thus one can write the coefficients, for small timesteps τ, as conditional averages over the n'th moment of x

$$a^{(n)} = \frac{1}{\tau}\langle (x(t+\tau) - x(t))^n \rangle. \tag{2.47}$$

With an equation of motion, for example the Langevin equation, the conditional averages can be calculated and used to find the Kramer-Moyal coefficients.

2.3 Advection-diffusion and effective diffusion coefficients

In the two previous sections, we have looked at the continuum description of fluids and processes outside of equilibrium. In this section, we combine the theory derived so far to study the combined effect of advection along streamlines found from solving the Navier-Stokes equations and the irreversible non-equilibrium spreading due to diffusion.

2.3.1 Deriving the advection-diffusion equation

For a particle subject to a stochastic force while moving through a viscous fluid with a relative velocity field u, the Langevin equation takes the form

$$m\dot{v} = -\gamma\left(v - u\right) + \xi(t). \tag{2.48}$$

Taking the overdamped limit, meaning inertial forces are vanishingly small compared to the frictional forces, the equation becomes

$$v = u + \frac{1}{\gamma}\xi(t). \tag{2.49}$$

It is assumed that the particle is small enough to have a negligible influence on the fluid flow, such that u is independent of the particle's position or momentum. The above equation can trivially be integrated to find the position at a time $t+\tau$

$$x(t+\tau) - x(t) = \tau u + \frac{1}{\gamma}\int_t^{t+\tau} \mathrm{d}t' \xi(t'). \tag{2.50}$$

The second term disappears upon taking the ensemble average over this quantity, resulting in the first order Kramer-Moyal coefficient $a^{(1)} = u$. A similar calculation for the second

moment yields $a^{(2)} = \langle \xi^2/\gamma^2 \rangle = 2k_BT/\gamma = 2D_m$ [62]. Using the derived forms for the Kramer-Moyal coefficients in the Fokker–Planck equation, and letting $\partial_x \to \nabla$ we find the advection-diffusion equation

$$\partial_t P(\boldsymbol{x}, t) = -\nabla \cdot (\boldsymbol{u} P) + \nabla^2 (D_m P). \tag{2.51}$$

Overdamped particles subject to a stochastic force in a moving fluid exhibiting Stokes drag satisfy the advection-diffusion equation.

The terms in the advection-diffusion equation have a clear physical interpretation, as the equation can be written as a continuity equation of advective and diffusive transport

$$\partial_t P = -\nabla \cdot \boldsymbol{j}_{\text{diff}} - \nabla \cdot \boldsymbol{j}_{\text{adv}}. \tag{2.52}$$

The diffusive current is from Fick's law, representing the fact that concentration gradients result in a flux of particles to even out concentration differences. The second term is an advective transport current from the passive probability following the streamlines of the fluid. The terms can be indentified as:

$$\boldsymbol{j}_{\text{diff}} = -D_m \nabla P, \qquad \boldsymbol{j}_{\text{adv}} = P\boldsymbol{u}. \tag{2.53}$$

If we further assume a constant molecular diffusion coefficient and incompressible flow, the advection-diffusion equation simplifies to

$$\partial_t P(\boldsymbol{x}, t) = -\boldsymbol{u} \cdot \nabla P + D_m \nabla^2 P. \tag{2.54}$$

By rescaling the probability density for the position of a single particle, it can be converted to a particle or heat concentration C. Performing this rescaling is done under the assumption that the concentration is dilute, such that interactions between particles are rare and will not affect the collective dynamics of the particles. Writing this equation on dimensionless form, we find

$$\partial_t C(\boldsymbol{x}, t) = -\text{Pe}\, \boldsymbol{u} \cdot \nabla C + \nabla^2 C, \tag{2.55}$$

where the ratio of advective and diffusive transport is quantified by the dimensionless Peclet number

$$\text{Pe} \equiv \frac{aU}{D_m}. \tag{2.56}$$

Dividing the Peclet number by the Reynolds number (2.22), we find another dimensionless number, the Schmidt number

$$\text{Sc} \equiv \frac{\nu}{D_m}, \tag{2.57}$$

which relates the diffusion of momentum, through the kinematic viscosity, with the diffusion of mass, through the molecular diffusion coefficient. For most cases, the diffusion of momentum is more efficient than diffusion of mass, creating a large value of the Schmidt number. The last dimensionless number used in this thesis acts as a Womersley number for the diffusion of mass instead of momentum

$$\text{Wo}_D \equiv \sqrt{\frac{\omega l^2}{D_m}} = \text{Wo}\sqrt{\text{Sc}}, \tag{2.58}$$

where it is expressed as a product between the two dimensionless numbers already defined. In addition to being without dimension, it is to our knowledge without a name. Therefore, we will refer to it as the diffusive Womersley number. At large values of Wo_D, particles do not have time to diffusive before the velocity field changes, making them follow the same streamline for a full period. Thus the advective transport over a period is always zero, and diffusion becomes the main transport mechanism. At small values, on the other hand, the diffusing particles can sample the velocity field at all points before the velocity changes.

2.3.2 Reciprocal relation for advection-diffusion

The reciprocal relation for advection diffusion can be derived from the advection-diffusion equation (2.54) itself [55]. To do this, we let the initial condition, of a Dirac-delta injection at $\boldsymbol{x}_A$ of a mass m_A at $t = 0$, be written directly in our differential equation

$$\partial_t C_A(\boldsymbol{x}, t) = -\boldsymbol{u}_A \cdot \nabla C_A + D\nabla^2 C_A + m_A \delta(\boldsymbol{x} - \boldsymbol{x}_A)\delta(t). \tag{2.59}$$

The concentration originating from an injection at $\boldsymbol{x}_A$ with the velocity field $\boldsymbol{u}_A$ is labeled C_A. For a stationary velocity field, we can take the time Fourier transformation of the equation

$$i\omega \tilde{C}_A = -\boldsymbol{u}_A \cdot \nabla \tilde{C}_A + D\nabla^2 \tilde{C}_A + m_A \delta(\boldsymbol{x} - \boldsymbol{x}_A), \tag{2.60}$$

where the tilde denotes the concentration in Fourier space. For an injection at $\boldsymbol{x}_B$, we would find the same equation with all the subscripts changed from A to B. Multiplying the above equation with the concentration originating from $\boldsymbol{x}_B$ in Fourier space $\tilde{C}_B$, we find

$$i\omega \tilde{C}_B \tilde{C}_A = -\tilde{C}_B \boldsymbol{u}_A \cdot \nabla \tilde{C}_A + D\tilde{C}_B \nabla^2 \tilde{C}_A + m_A \delta(\boldsymbol{x} - \boldsymbol{x}_A)\tilde{C}_B. \tag{2.61}$$

The same can be done for the equation with A and B interchanged. By subtracting the two from one another the left hand side cancels, yielding

$$\begin{aligned} m_A \delta(\boldsymbol{x} - \boldsymbol{x}_A)\tilde{C}_B - m_B \delta(\boldsymbol{x} - \boldsymbol{x}_B)\tilde{C}_A = \tilde{C}_B \boldsymbol{u}_A \cdot \nabla \tilde{C}_A - D\tilde{C}_B \nabla^2 \tilde{C}_A \\ - \tilde{C}_A \boldsymbol{u}_B \cdot \nabla \tilde{C}_B + D\tilde{C}_A \nabla^2 \tilde{C}_B. \end{aligned} \tag{2.62}$$

Manipulating this expression by using the product rule backwards for the nabla operator, assuming an incompressible velocity field (2.4), we find

$$\begin{aligned} m_A \delta(\boldsymbol{x} - \boldsymbol{x}_A)\tilde{C}_B - m_B \delta(\boldsymbol{x} - \boldsymbol{x}_B)\tilde{C}_A = \nabla \cdot \left(D\tilde{C}_A \nabla \tilde{C}_B - D\tilde{C}_B \nabla \tilde{C}_A - \tilde{C}_B \tilde{C}_A \boldsymbol{u}_B \right) \\ + \boldsymbol{u}_A \tilde{C}_B \nabla \tilde{C}_A + \boldsymbol{u}_B \tilde{C}_B \nabla \tilde{C}_A. \end{aligned} \tag{2.63}$$

For creeping flow, the velocity field from the Stokes equation (2.16) can be completely reversible, such that changing the sign of the external force also changes the sign of the velocity field. Hence, for creeping flow, the two velocity fields can satisfy

$$\boldsymbol{u}_A = -\boldsymbol{u}_B. \tag{2.64}$$

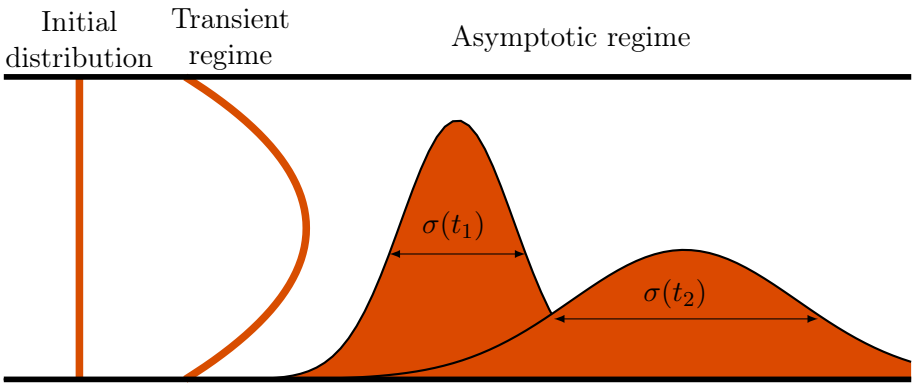

Figure 2.1: For a straight two-dimensional channel exhibiting Poiseuille flow, the evolution of a vertical line initial injection is illustrated. In the transient regime, the particles follow the parabolic flow profile. When the particles have vertically crossed the channel multiple times, $t \gg a^2/D_m$, the asymptotic regime where Taylor–Aris dispersion holds is reached. In this regime, the concentration profile is a Gaussian around the mean displacement, with a standard deviation σ. The effective diffusion coefficient measures the slope of the linear time increase in σ^2.

For cases where this equality is satisfied, the last two terms of equation (2.63) will cancel, and we are left with

$$m_A \delta(\boldsymbol{x} - \boldsymbol{x}_A)\tilde{C}_B - m_B \delta(\boldsymbol{x} - \boldsymbol{x}_B)\tilde{C}_A = \nabla \cdot \left(D\tilde{C}_A \nabla \tilde{C}_B - D\tilde{C}_B \nabla \tilde{C}_A - \tilde{C}_B \tilde{C}_A \boldsymbol{u}_B \right). \quad (2.65)$$

For materially closed systems, the right hand side vanishes upon volume integration, and on the left hand side the Dirac-delta functions make the integrals trivial. Performing the inverse Fourier transform, we find what we will refer to as the reciprocal relation:

$$\frac{1}{m_A} C_A(\boldsymbol{x}_B, t) = \frac{1}{m_B} C_B(\boldsymbol{x}_A, t). \quad (2.66)$$

Thus, the concentration measured at $\boldsymbol{x}_B$, resulting from a concentration injected at $\boldsymbol{x}_A$, will have the same value as a concentration measured at $\boldsymbol{x}_A$, resulting from a concentration injected at $\boldsymbol{x}_B$, if the velocity field is reversed between the two events. The relation is only valid for incompressible and creeping flow, where the non-linear term in the Navier-Stokes equations (2.23) can be ignored. Its connection to the well known Onsager symmetries can be seen by deriving the same relation (2.66) from a microscopic viewpoint, where the time reversibility at the microscopic scale and the fact that average spontaneous fluctuations obey linear macroscopic laws [63] is exploited, similar to Onsager's original derivation [65].

2.3.3 Taylor–Aris dispersion

For pure diffusion, the spatial variance of the concentration scales linearly with time, with a proportionality factor $2D_m$. With the addition of advection, the dispersive interplay between the diffusive and advective motion can be captured in an effective diffusion coefficient for the variance of the concentration parallel with the mean flow direction

$$\langle (x - \langle x \rangle)^2 \rangle = 2D_{\parallel} t. \quad (2.67)$$

For pure diffusion, the parallel diffusion coefficient is equal to the molecular one. G.I. Taylor derived the first description of an effective diffusion coefficient on his seminal paper *Dispersion of soluble matter in solvent flowing slowly through a tube* [19]. For adequately narrow and long tubes, the molecular diffusion of the solute will even out concentration differences across the tube while still exhibiting differences along it. Due to molecular diffusion, the tracer particles will collectively move in the flow direction with the average flow speed, with a spreading around this average resulting in an effective diffusion coefficient

$$D_{\parallel} = \frac{a^2 U^2}{48 D_m}, \tag{2.68}$$

where a is the radius of the pipe. At first glance, this result might seem surprising, as the effective diffusion coefficient is inversely proportional to the molecular diffusion coefficient. This can be understood with an analogy to driving on a road with many lanes with different driving speeds. If all the cars change lane often, they will arrive at close to the same time, but if they very rarely change lanes, some will arrive long before the others, resulting in a larger spread. The above equality holds when vertical concentration differences are slowly equilibrated compared to the horizontal advection $D_m/a \ll U$, meaning a large Peclet number.

Taylor's result was later generalized by Aris [20], who derived an effective spreading for unidirectional flow in an arbitrary axially invariant channel. Aris did so by identifying the Peclet number (2.56) and found that for such geometries, the effective diffusion is given by

$$D_{\parallel} = D_m \left(1 + \kappa \mathrm{Pe}^2\right). \tag{2.69}$$

The κ is a geometrical factor determined by the flow geometry and boundary conditions. For a circular pipe, it takes the value of $1/48$, in agreement with Taylor's result in the high Peclet limit, where the constant of 1 becomes negligible. For the flow in a straight two-dimensional channel, κ takes the value of $2/105$, when a is the channel half-width. An illustration of the evolution from the initial distribution to the transient regime for Poiseuille flow is displayed in figure 2.1 on the facing page. In the frame of reference following the mean flow, the cross-sectionally averaged solute concentration will, in the asymptotic regime, obey a one-dimensional diffusion equation, where the effective diffusion replaces the molecular diffusion coefficient.

2.3.4 Brenner's theory

Brenner further generalized Aris' result to arbitrary spatially periodic porous media [41]. His general theoretical framework gives a consistent way to calculate the effective diffusion coefficient for infinitely periodic repeating unit cells in an arbitrary number of dimension. The advantage of Brenner's theory is that one only needs to work inside a single unit cell, but, similar to Aris, comes with the disadvantage that the information in the transient regime is lost.

The geometry now consists of infinitely many connected periodic unit cells, labeled by the index n. We let $P(\boldsymbol{R}_n, \boldsymbol{r}, t|\boldsymbol{R}_{n'}, \boldsymbol{r}')$ represent the probability density for a Brownian

particle to be located at position $\boldsymbol{r}$ inside unit cell n at a time t, given that it was located at position $\boldsymbol{r}'$ inside unit cell n' at a time $t = 0$. The capital $\boldsymbol{R}_n$ denotes the global position of unit cell n, while the letter case $\boldsymbol{r}$ denote the local position within that unit cell. Without loss of generality, we can let the initial concentration be located at the zeroth unit cell for $t = 0$, such that $\boldsymbol{R}_{n'} = 0$, at the position $\boldsymbol{r}' = 0$, simplifying our notation to $P(\boldsymbol{R}_n, \boldsymbol{r}, t)$. The probability density is by definition normalized to one, and must converge asymptotically to zero at a sufficiently fast. The probability density must also satisfy both the continuity equation and the advection-diffusion equation. Assuming that the boundary is impenetrable to both the fluid and the flux of particles, it must satisfy the boundary condition

$$\hat{\boldsymbol{n}} \cdot \nabla P = 0 \quad \text{on} \quad \partial\Omega, \tag{2.70}$$

where $\hat{\boldsymbol{n}}$ is the boundary normal vector, and $\partial\Omega$ is the geometric boundary. Brenner continues by defining the local moments

$$\boldsymbol{\mu}_m(\boldsymbol{r}, t) \equiv \sum_n \boldsymbol{R}_n^m \; P(\boldsymbol{R}_n, \boldsymbol{r}, t), \tag{2.71}$$

acting as a coarse-grained positional moment, for a specific local position $\boldsymbol{r}$ within the unit cell at a time t. The m'th moment is constructed from m vectors without any operation between them, making the moments a scalar, vector, rank two tensor, and so on. Since the differential operators commute with the unit cell position vectors, the local moments must satisfy the advection-diffusion equation

$$\partial_t \boldsymbol{\mu}_m = -\nabla \cdot (\boldsymbol{u}\boldsymbol{\mu}_m) + D_m \nabla^2 \boldsymbol{\mu}_m + \delta_{m0}\delta(\boldsymbol{r})\delta(t), \tag{2.72}$$

where the last term describes the initial injection of a unit mass at $t = 0$. At the boundary between two neighbouring unit cells, n and n^*, the probability density can equally be described as $P(\boldsymbol{R}_n + \boldsymbol{r})$, or $P(\boldsymbol{R}_{n^*} + \boldsymbol{r}^*)$, as the two spatial coordinates represent same point. If we let $\boldsymbol{l}_j$ denote the spatial difference between the two neighbouring unit cells, we see that the probability density must satisfy

$$P(\boldsymbol{R}_{n^*}, \boldsymbol{r} + \boldsymbol{l}_j) = P(\boldsymbol{R}_n, \boldsymbol{r}). \tag{2.73}$$

Considering the continuity of $\boldsymbol{u}$ and the flux $\boldsymbol{J}$ over the cell boundary, we also find the same relation for the probability density's gradient:

$$\nabla P(\boldsymbol{R}_{n^*}, \boldsymbol{r} + \boldsymbol{l}_j) = \nabla P(\boldsymbol{R}_n, \boldsymbol{r}). \tag{2.74}$$

By performing a sum over n^* and n on the left and right hand side of equation (2.73) respectively, one can derive *jump conditions* for each of the local moments. The jumps, denoted by $[\![a]\!]$, give the change of the given quantity a across the opposite boundary of the unit cell. The first three jumps in the local moments can then be shown to be given by:

$$[\![\mu_0]\!] = 0, \qquad [\![\boldsymbol{\mu}_1]\!] = -[\![\boldsymbol{r}\mu_0]\!], \qquad \text{and} \qquad [\![\boldsymbol{\mu}_2]\!] = -\left[\!\!\left[\frac{\boldsymbol{\mu}_1\boldsymbol{\mu}_1}{\mu_0}\right]\!\!\right]. \tag{2.75}$$

Using equation (2.74) the jump conditions on the gradients are found to be:

$$[\![\nabla \mu_0]\!] = 0, \qquad [\![\nabla \boldsymbol{\mu}_1]\!] = -[\![\nabla \boldsymbol{r}\mu_0]\!], \qquad \text{and} \qquad [\![\nabla \boldsymbol{\mu}_2]\!] = -\left[\!\!\left[\nabla \frac{\boldsymbol{\mu}_1 \boldsymbol{\mu}_1}{\mu_0}\right]\!\!\right]. \tag{2.76}$$

This set of partial differential equations, jump conditions and boundary conditions can in principle be solved recursively to determine $\boldsymbol{\mu}_m$ uniquely [66], starting with $m = 0$. This approach would be equivalent to solving two advection-diffusion equations, and is therefore much more demanding than solving Brenner's final set of equations, which we will se in the following. The jump moments of a quantity $\boldsymbol{a}$ is related to the surface integral over the unit cell

$$\int_{\partial\tau} \mathrm{d}\boldsymbol{S} \cdot \boldsymbol{a} = \sum_{j=1}^{d} \int_{s_j} \mathrm{d}\boldsymbol{s} \cdot [\![\boldsymbol{a}]\!], \tag{2.77}$$

where d represents the number of spatial dimensions for which the jump conditions must be calculated, and $\partial\tau$ is the unit cell boundary.

Brenner goes on to define the total moments as a volume integral of the local moments over the fluid volume of a unit cell:

$$\boldsymbol{M}_m(t) = \int_\Omega \boldsymbol{\mu}_m(\boldsymbol{r}, t)\ \mathrm{d}^3\boldsymbol{r}. \tag{2.78}$$

From the definition of the local moments (2.71), we see that the total moments are coarse-grained positional moments for the concentration, which does not deal with the probability of being at a specific position within the unit cell, only the probability that each unite cell is occupied. Taking the time derivative of the total moments, and applying equation (2.72), we find that the total moments must satisfy the equation

$$\frac{\mathrm{d}\boldsymbol{M}_m}{\mathrm{d}t} = -\int_\Omega \mathrm{d}^3\boldsymbol{r}\ \boldsymbol{\nabla} \cdot (\boldsymbol{u}\boldsymbol{\mu}_m) + D_m \int_\Omega \mathrm{d}^3\boldsymbol{r}\ \boldsymbol{\nabla}^2 \boldsymbol{\mu}_m + \delta_{m0}\delta(t). \tag{2.79}$$

By applying Gauss's theorem, turning the volume integral into a surface integral, we can write the equation in terms of the jump moments using equation (2.77)

$$\frac{\mathrm{d}\boldsymbol{M}_m}{\mathrm{d}t} = -\sum_{j=1}^{d} \int_{s_j} \mathrm{d}\boldsymbol{s} \cdot \boldsymbol{u}\, [\![\boldsymbol{\mu_m}]\!] + D_m \sum_{j=1}^{d} \int_{s+j} \mathrm{d}\boldsymbol{s} \cdot [\![\nabla \boldsymbol{\mu}_m]\!] + \delta_{m0}\delta(t). \tag{2.80}$$

An essential consequence of this rewrite is that the second-order total moment can be calculated solely from the information of the jump conditions for the local moments. Applying the jump conditions above (2.75) and (2.76), we see that the total moment of second-order can be expressed as the jump conditions of zeroth and first-order local moments, independent of the second order.

To continue we must find the local moments, and use these to calculate the total moments. Brenner shows that in the long-time regime, meaning $D_m t/l^2 \gg 1$, the zeroth moment is given by $\mu_0 = 1/\Omega$, where we have ignored the decaying exponentials completely,

granting $M_0 = 1$. For $m = 1$, the jump conditions makes the second term of (2.80) disappear, and the first term can be rewritten to the form

$$\frac{\mathrm{d}\boldsymbol{M}_1}{\mathrm{d}t} = \frac{1}{\Omega}\int_\Omega \mathrm{d}^3 r\ \boldsymbol{u} = \langle \boldsymbol{u} \rangle, \tag{2.81}$$

where we have assumed an incompressible flow, and defined the notation of a unit cell average in terms of brackets. With this equation for $\boldsymbol{M}_1$ we perform an a priori guess which satisfies the above equation, with an additional term $\boldsymbol{B}$ containing the possible spatial dependence, which would disappear upon taking the time derivative,

$$\boldsymbol{\mu}_1 = \langle \boldsymbol{u} \rangle t + \boldsymbol{B}(\boldsymbol{r}). \tag{2.82}$$

Plugging our guess into equation (2.72), we find that the new unknown $\boldsymbol{B}$ is the solution of the equation

$$\langle \boldsymbol{u} \rangle = -\boldsymbol{u} \cdot \nabla \boldsymbol{B} + D_m \nabla^2 \boldsymbol{B}, \tag{2.83}$$

and has to satisfy the boundary condition

$$\hat{\boldsymbol{n}} \cdot \nabla \boldsymbol{B} = 0 \qquad \text{on} \qquad \partial\Omega. \tag{2.84}$$

Using equation (2.75), we find it is subject to the jump conditions $[\![\boldsymbol{B}]\!] = -[\![\boldsymbol{r}]\!]$ and $[\![\nabla \boldsymbol{B}]\!] = 0$. Performing a volume integral of the first order local moment (2.82) over the unit cell gives us the first order total moment

$$\boldsymbol{M}_1 = \langle \boldsymbol{u} \rangle t + \langle \boldsymbol{B} \rangle. \tag{2.85}$$

With our expression for μ_0 and $\boldsymbol{\mu}_1$, in addition to the jump condition of $\boldsymbol{\mu}_2$ being expressed in terms of these, we can plug everything into equation (2.80), to find

$$\frac{\mathrm{d}M_{2,ij}}{\mathrm{d}t} = 2\langle u_i \rangle \langle u_j \rangle t + \langle u_i \rangle \langle B_j \rangle + \langle B_i \rangle \langle u_j \rangle + 2D_m \left\langle \nabla_k B_i \nabla_k B_j \right\rangle, \tag{2.86}$$

As mention earlier, the total moments are closely related to the positional moments on a macroscopic scale. A macroscopic scale is here meant to mean a Darcy scale where the local position $\boldsymbol{r}$ is irrelevant, compared to the global position vectors. The mean displacement in the asymptotic time limit can then be written as

$$\langle R_i \rangle = \int_{\Omega_{\mathrm{tot}}} R_i\, P(R_i)\, \mathrm{d}V = \int_\Omega \sum_n R_{n,i} P(R_{n,i}, \boldsymbol{r}, t)\, \mathrm{d}^3 \boldsymbol{r} = \boldsymbol{M}_{1,i} \propto \langle u_i \rangle t, \tag{2.87}$$

where we have changed from an integral over the total fluid volume, to an integral over the unit cell volume, by including a sum over the unit cells. This result agrees with our intuition that the mean position of the solute should travel with the average fluid velocity. The mean square displacement can likewise be calculated from the second order moment

$$\langle (R_i - \langle R_i \rangle)\,(R_j - \langle R_j \rangle) \rangle = \int_{\Omega_{\mathrm{tot}}} R_i R_j\, P\, \mathrm{d}V - \langle R_i \rangle \langle R_j \rangle = M_{2_{ij}} - M_{1_i} M_{1_j}. \tag{2.88}$$

We have recognized the definition of the first and second total moment, similarly as above. From its definition (2.67), this quantity must be proportional to the dispersion tensor D_{ij}, which we can now define as

$$D_{ij} = \frac{1}{2} \lim_{t\to\infty} \frac{\mathrm{d}}{\mathrm{d}t} \left(M_{2_{ij}} - M_{1_i} M_{1_j} \right) = D_m \left\langle \nabla_k B_i \nabla_k B_j \right\rangle . \tag{2.89}$$

Here we have used our known expressions of the first (2.85) and second (2.86) order total moment to find the final form. The dispersion tensor can be calculated by solving (2.83), and plugging the solution in to the equation above. For a two-dimensional channel with horizontal flow in the $\hat{\boldsymbol{x}}$ direction, we are only interested in the dispersion tensor for $i = j = 0$, which in this case becomes a scalar field and can be written as the effective diffusion coefficient

$$D_{\parallel} = D_m \left\langle \nabla B_0 \cdot \nabla B_0 \right\rangle . \tag{2.90}$$

To get the final result on a form similar to that of Aris, we redefine the component of $\boldsymbol{B}$ parallel to the flow, to

$$B_0 = B - x. \tag{2.91}$$

The parallel diffusion coefficient in the flow direction is then found from calculating

$$D_{\parallel} = D_m \left\langle 1 - 2\nabla_x B + |\nabla B|^2 \right\rangle . \tag{2.92a}$$

With this redefinition (2.91), the scalar field B is the solution of the equation

$$D_m \nabla^2 B - \mathbf{u} \cdot \boldsymbol{\nabla} B = -\hat{\mathbf{x}} \cdot (\mathbf{u} - \langle \mathbf{u} \rangle) , \tag{2.92b}$$

which must satisfy the boundary condition on the geometry

$$\hat{\mathbf{n}} \cdot \boldsymbol{\nabla} B = -\hat{\mathbf{n}} \cdot \hat{\mathbf{x}}. \tag{2.92c}$$

Additionally, we may remove the gauge freedom in B by requiring $\langle B \rangle = 0$. The three equations above gives a closed set of equations and boundary conditions, to find the effective diffusion coefficient by only working within the unit cell. With the redefinition of B_0 performed above, we see that the standard Aris result is retrieved for axially invariant channels, where B becomes independent of x.

Chapter 3

Numerical Methods

This chapter briefly introduces the two main numerical methods used in this thesis, the lattice-Boltzmann method (LBM) and the finite element method (FEM). The two methods differ fundamentally from one another, with their own set of advantages and disadvantages. The LBM is a bottom-up approach, where one simulates rule-based particle collisions on a mesoscopic lattice, which gives rise to the correct hydrodynamics equations on the macroscopic scale. The FEM, on the other hand, is a more mathematically rigorous approach, where one tries to approximate the solution to a given partial differential equation using a set of basis functions. For our purpose, these methods will solve the Navier-Stokes equations (2.4, 2.19), the advection-diffusion equation (2.54), and Brenner's equations (2.92b, 2.92c). The non-linearity of the Navier-Stokes equations, complex boundary conditions and coupled equations can make analytical solutions difficult or impossible to find. Therefore, the numerical methods presented here serve as a toolbox for finding results that would otherwise be inaccessible. Another important aspect is that analytical results can be compared against numerical simulations, either to verify the calculation or to find the validity of perturbative or approximate analytical answers. Therefore, numerical and analytical results go hand in hand and supplement each other throughout the thesis. All of the code used in this thesis is accessible through a dedicated Git repository[1] and can be used for reproducibility and a better understanding of how to implement the numerical methods described in this section.

3.1 The lattice-Boltzmann method

In the 1980's a new paradigm for simulations of hydrodynamics began with the introduction of *lattice gas models* [60]. Previously, a top-down approach was used, where one starts with the macroscopic equations and works downward by discretizing them. In this new paradigm, a bottom-up approach was used, where one starts with a rule-based particle simulation algorithm on a lattice, and from the rules derive their corresponding macroscopic equations. The first example of such a model was the *lattice gas cellular automata* [60], which was a predecessor of the lattice Boltzmann models, which we will discuss here. The

[1] `https://github.com/ivarhaugerud/master`

notation and definitions will follow *The Lattice Boltzmann Method: Principles and Practice* by Krueger et al. [67], which I refer to for a more detailed introduction to the LBM.

3.1.1 Fundamentals

While the original lattice gas models used a fixed number of particles on each lattice site, the LBM uses occupation probabilities $f_i(\boldsymbol{x}, t)$; one for each of the discrete velocity directions i. This function is called the particle population number, and represents the density of particles with velocity $\boldsymbol{c}_i$ at a lattice point $\boldsymbol{x}$ at a time t. From the particle populations we can define the mass density

$$\rho(\boldsymbol{x}, t) = \sum_{i=1}^{N} f_i(\boldsymbol{x}, t), \tag{3.1}$$

where we are using natural units where the mass of each particle is set to 1. Here the number N denotes the number of velocity directions, matching the number of neighbouring sites. Using the discrete velocity vectors, one can define the momentum density

$$\rho \boldsymbol{u}\Big|_{(\boldsymbol{x},t)} = \sum_{i=1}^{N} \boldsymbol{c}_i f_i(\boldsymbol{x}, t) + \frac{1}{2}\Delta t\, \boldsymbol{F}, \tag{3.2}$$

where $\boldsymbol{F}$ is the body force acting on the fluid. Between each timestep an occupation $f_i(\boldsymbol{x}, t)$ moves with a velocity $\boldsymbol{c}_i$ to a neighbouring lattice site $\boldsymbol{x} + \boldsymbol{c}_i \Delta t$, where it will be acted upon by a collision operator Ω_i, which redistributes all the f_i's among the other velocity directions of that lattice site

$$f_i(\boldsymbol{x} + \boldsymbol{c}_i \Delta t, t + \Delta t) = f_i(\boldsymbol{x}, t) + \Omega_i(\boldsymbol{x}, t)\Delta t. \tag{3.3}$$

The collision operator gives the time dependence of the occupation number, and must satisfy conservation of both mass and momentum, as they are conserved in the macroscopic equations (2.3, 2.23). There are many possible operators which satisfy these conditions, but we will use the BGK (Bhatnagar, Gross and Krook) model, which takes the almost intuitive form of

$$\Omega_i(f) = -\frac{f_i - f_i^{eq}}{\tau}\Delta t. \tag{3.4}$$

This operator relaxes the particle population at a specific lattice point towards the local equilibrium value, with a characteristic time τ. At equilibrium the collisions operator vanish, and a steady state is reached. A collision operator on this form for lattice-Boltzmann simulations was first introduced by Qian [68], and further analyzed by Chen and Doolen [69]. This collision operator uses the local equilibrium particle occupation

$$f_i^{eq}(\boldsymbol{x}, t) = \omega_i \rho \left(1 + \frac{\boldsymbol{u} \cdot \boldsymbol{c}_i}{c_s^2} + \frac{(\boldsymbol{u} \cdot \boldsymbol{c}_i)^2}{2c_s^4} - \frac{\boldsymbol{u} \cdot \boldsymbol{u}}{c_s^2}\right), \tag{3.5}$$

where the number ω_i weights the different velocity directions of the velocity set, and must sum to one. The equilibrium distribution depends only on the density (3.1) and the

momentum (3.2) of the given lattice point, and has the important property of making the collision operator (3.4) conserve mass $\sum_i \Omega_i = 0$ and momentum $\sum_i \boldsymbol{c}_i \Omega_i = 0$. In the equilibrium occupation the speed of sound in the media was introduced

$$c_s^2 = \frac{1}{3}\frac{\Delta x^2}{\Delta t^2}. \tag{3.6}$$

It is common to use natural units, where $\Delta x = \Delta t = 1$, such that $c_s = 1/\sqrt{3}$.

Through Chapman–Enskog theory, one can relate the equilibrium occupations to the Navier-Stokes equations by performing a series expansion of the occupation probabilities f_i in terms of their equilibrium value f_i^{eq} in powers of what is known as the Knutsen number, a dimensionless number defined by the mean free path divided by the characteristic macroscopic length scale. The mean free path is $\Delta x = 1$, and the characteristic macroscopic length scale will depend on the number of lattice points included in the simulation. To retrieve a velocity field equivalently to that found with the Navier-Stokes equations, one needs enough lattice points to ensure a small Knutsen number, such that truncating the expansion at second order is satisfactory. For a more comprehensive discussion, see *Flow in Porous Media* [60] or *The Lattice Boltzmann Method* [67]. Following this procedure, one finds the kinematic viscosity of the fluid to be

$$\nu = c_s^2 \left(\tau - \frac{\Delta t}{2}\right). \tag{3.7}$$

A large viscosity is therefore associated with a quick convergence towards the local equilibrium.

Not all discretization methods will retrieve a solution of the Navier-Stokes equations on a macroscopic scale. For example, a square lattice with only horizontal and vertical connections will not suffice. In this thesis, we will use the D2Q9 lattice, meaning a two-dimensional lattice where each lattice point has nine neighbours, including itself. The velocity vectors are defined as

$$\boldsymbol{c}_0 = 0 \qquad \boldsymbol{c}_{1,3} = (\pm 1, 0) \qquad \boldsymbol{c}_{2,4} = (0, \pm 1) \qquad \boldsymbol{c}_{5,6,7,8} = (\pm 1, \pm 1). \tag{3.8}$$

An illustration of the lattice with the velocity vectors, is displayed in figure 3.1 on the next page. Each velocity direction is associated with a weight ω_i, which for the D2Q9 lattice takes the values

$$\omega_0 = \frac{4}{9} \qquad \omega_{1,2,3,4} = \frac{1}{9} \qquad \omega_{5,6,7,8,9} = \frac{1}{36}. \tag{3.9}$$

Other common velocity sets include D1Q3, D3Q15, D3Q19 and D3Q27 [67]. For numerical efficiency, it is common to simplify the expression for the equilibrium occupation numbers

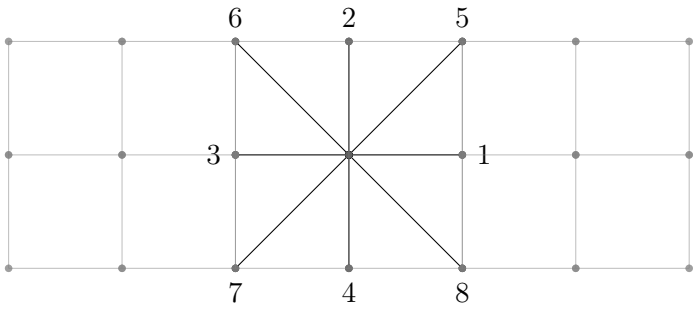

Figure 3.1: The unit cell for a D2Q9 square lattice is displayed. Each lattice point has 8 labeld neighbours to which the distribution is propagated after the collision step, in addition to propagating onto itself. In natural units the distance to first four lattice points is 1, and $\sqrt{2}$ to the angeld points.

(3.5), for the lattice you are working with. For the D2Q9 lattice these take the form

$$
\begin{aligned}
f_0^{eq} &= \frac{2\rho}{9}\left(2-3u^2\right) && (3.10)\\
f_1^{eq} &= \frac{\rho}{18}\left(2+6u_x+9u_x^2-3u^2\right) & f_5^{eq} &= \frac{\rho}{36}\left(1-3\left(u_x-u_y\right)-9u_xu_y+3u^2\right)\\
f_2^{eq} &= \frac{\rho}{18}\left(2+6u_y+9u_y^2-3u^2\right) & f_6^{eq} &= \frac{\rho}{36}\left(1-3\left(u_x-u_y\right)-9u_xu_y+3u^2\right)\\
f_3^{eq} &= \frac{\rho}{18}\left(2-6u_x+9u_x^2-3u^2\right) & f_7^{eq} &= \frac{\rho}{36}\left(1-3\left(u_x+u_y\right)+9u_xu_y+3u^2\right)\\
f_4^{eq} &= \frac{\rho}{18}\left(2-6u_y+9u_y^2-3u^2\right) & f_8^{eq} &= \frac{\rho}{36}\left(1+3\left(u_x-u_y\right)-9u_xu_y+3u^2\right),
\end{aligned}
$$

where the density and velocity field is calculated for the relevant lattice point, and $u^2 = \boldsymbol{u}\cdot\boldsymbol{u}$. Using the above expression reduces the number of floating point operations, due to the orthogonality of different components being precalculated.

3.1.2 Initialization and boundary conditions

To initialize the system at $t = 0$, a value must be set for f_i at each lattice point. We use the equilibrium distribution of occupations (3.10) with a density $\rho = 1$ and a velocity $\boldsymbol{u} = 0$. This gives us the initial mass distribution needed to start the algorithm.

The Navier-Stokes equations are solved with no-slip boundary condition (2.20). To achieve the no-slip boundary condition, one can employ what is known as the half-way bounce-back boundary condition. Half-way bounce back returns the occupation numbers that have entered the boundary to its previous lattice site, with the velocity direction reversed in a single time step. An illustration is displayed in figure 3.2 on the facing page, where the wall is located at an intermediate point between the fluid and solid node.

3.1.3 Updating scheme

The simulation is done by evolving the system with equation (3.3), which can be decomposed in two different steps performed in succession. First the collision operator must be

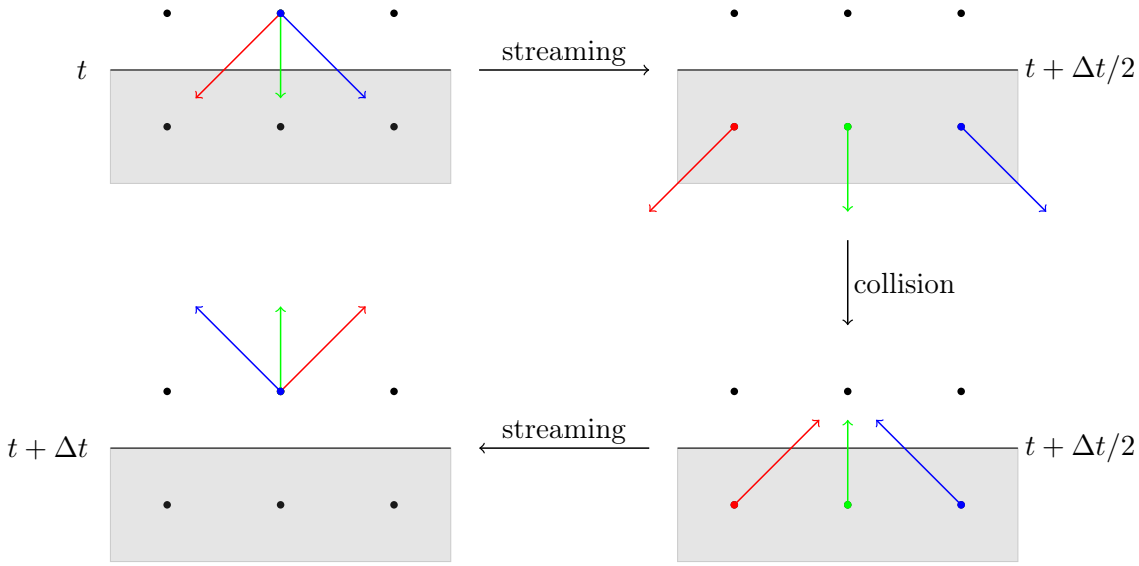

Figure 3.2: For the half-way bounce-back boundary condition, the wall is located half-way between the two lattice points. The occupations are initially streamed onto the solid node, where their directions are flipped and streamed back onto their original fluid node. This process is done during a single time step, contrary to the full-way bounce back where the particles stay one time step on the solid node before being streamed back.

calculated, called the collision step, then the resulting particle occupations are moved to their corresponding neighboring sites, called the streaming step. From equation (3.3) and (3.4), the distribution function after collision, $f_i^\star$, takes the form of

$$f_i^\star(\boldsymbol{x}, t) = f_i(\boldsymbol{x}, t) - \frac{\Delta t}{\tau}\left(f_i(\boldsymbol{x}, t) - f_i^{eq}(\boldsymbol{x}, t)\right). \tag{3.11}$$

To reduce the number of floating point operations, it is efficient to write the equation on the form

$$f_i^\star(\boldsymbol{x}, t) = \left(1 - \frac{\Delta t}{\tau}\right) f_i(\boldsymbol{x}, t) - \frac{\Delta t}{\tau} f_i^{eq}(\boldsymbol{x}, t), \tag{3.12}$$

where the numerical prefactors can be calculated outside the time evolution. Once the distribution after collision is calculated, one performs the streaming step, according to

$$f_i(\boldsymbol{x} + \boldsymbol{c}_i \Delta t, t + \Delta t) = f_i^\star(\boldsymbol{x}, t). \tag{3.13}$$

A visualization of the streaming step for the D2Q9 lattice is displayed in figure 3.3 on the next page. After initializing the system, the full LBM algorithm can be summarized in the following steps:

- From the occupation probabilities $f_i(\boldsymbol{x}, t)$, calculate the density ρ (3.1) and velocity $\boldsymbol{u}$ (3.2) at each lattice point.
- Write the macroscopic variables you are interested in to a file.

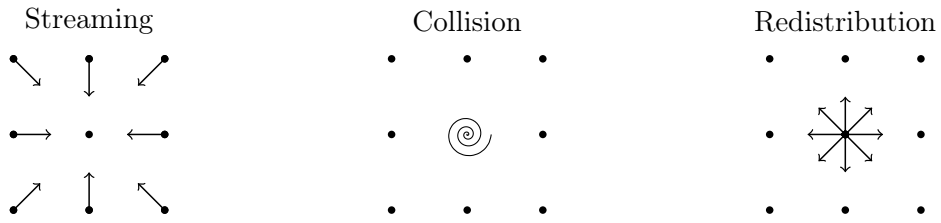

Figure 3.3: In the streaming step, one f_i from each neighbouring lattice site is streamed towards the same point, where they collide according to Ω_i and is redistributed between the 9 orientations. This occurs for each time step of the algorithm, where the collision and redistribution conserve both mass and momentum.

- Calculate the equilibrium distribution f_i^{eq} (3.5) .
- Perform the collision step (3.12).
- Propagate the distribution to the neighbouring nodes (3.13).
- Propagate the particle occupations at the boundary.
- Increase the timestep and go back to step one.

Implementing the above scheme gives a second-order solver in both space and time for the weakly compressible NSE [67]. When searching for steady-state flows, the relative L_2 norm is used to test if the flow field has converged, where the relative L_2 norm is defined as

$$L_2 \equiv \sqrt{\frac{\sum_s \left(\boldsymbol{u}(\boldsymbol{x}_s, t) - \boldsymbol{u}(\boldsymbol{x}_s, t - \Delta t)\right)^2}{\sum_s \boldsymbol{u}^2(\boldsymbol{x}_s, t)}}, \tag{3.14}$$

where we sum over all lattice sites s, and perform the dot product when squaring. If the L_2 norm is smaller than a threshold value, for us set to 10^{-9}, we say that the velocity field has converged to the steady state. Checking if the velocity field has converged can be added as the last step of the algorithm described above.

3.1.4 Simulating the advection-diffusion equation

The lattice Boltzmann method can also be used to simulate the advection-diffusion equation. Since the NSE can be viewed as an advection-diffusion equation for the fluid momentum density $\rho\boldsymbol{u}$, the LBM is easily adaptable to solving the advection-diffusion equation. The particle propagation can be written on the exact same form

$$g_i^\star(\boldsymbol{x}, t) = g_i(\boldsymbol{x}, t) - \frac{\Delta t}{\tau_g}\left(g_i(\boldsymbol{x}, t) - g_i^{eq}(\boldsymbol{x}, t)\right) + Q_i(\boldsymbol{x}, t), \tag{3.15}$$

now g is the particle or heat occupation and Q describes the sinks and drains of the solute. The time constant τ_g gives the molecular diffusion coefficient of the simulation

$$D_m = c_s^2\left(\tau_g - \frac{\Delta t}{2}\right), \tag{3.16}$$

which shows the close connection to the dynamic viscosity of the fluid (3.7). The equilibrium concentration takes the exact same form

$$g_i^{eq}(\boldsymbol{x},t) = \omega_i C\left(1 + \frac{\boldsymbol{u}\cdot\boldsymbol{c}_i}{c_s^2} + \frac{(\boldsymbol{u}\cdot\boldsymbol{c}_i)^2}{2c_s^4} - \frac{\boldsymbol{u}\cdot\boldsymbol{u}}{2c_s^2}\right). \tag{3.17}$$

To find the macroscopic concentration at a lattice point, one takes the sum over the g_i's, $\sum_i g_i = C$. The two algorithms are close to identical, only differing in the initialization, as it will depend on the initial condition for the concentration profile of interest. The bounce-back boundary condition is used for solute transport, displayed in figure 3.2 on page 29. For heat transport, where the wall has a fixed temperature value T, the anti-bounce back boundary condition is used, where the post-collision occupation at a boundary node $\boldsymbol{x}_b$ is given by

$$g_i(\boldsymbol{x}_b, t+\Delta t) = -g_i^*(\boldsymbol{x}_b, t) + 2\omega_i T. \tag{3.18}$$

The wall's temperature is now fixed to a constant and does not change when interacting with the diffusing temperature concentration.

When the concentration field does not influence the motion of the fluid, the concentration field is called *passive*. For passive dispersion, one can first solve the Navier-Stokes equations to find the velocity field and then perform the advection-diffusion simulation. For concentration-dependent flows, on the other hand, the Navier-Stokes and advection-diffusion time steps must be performed in succession throughout the whole simulation. The *passive* assumption is also made for the diffusion of temperature density, where the viscosity and density are assumed to be independent of the temperature.

3.2 The finite element method

The finite element method (FEM) is a computational method for solving partial differential equations, where the domain is discretized into a finite number of elements. By writing the equation in its variational form, the solution is found from minimizing some residue, using the calculus of variations, over the elements. The collection of equations from all the elements results in a set of linear algebraic equations that approximates the solution to the partial differential equation in question. The FEM produces an approximate solution by discretizing the space where we look for solutions, and therefore the solution itself. This is in contrast to finite difference methods, where the equations are approximated by discretizing the operators. Furthermore, it contrasts finite volume methods, where the volumes are discretized and the equations are written in terms of fluxes across the boundaries of the discretized cells. Although both of these are often used in computational fluid dynamics, they will not be used in this thesis. While the FEM is often derived in a mathematically rigorous way, with a strong emphasis on functional spaces, variational formulations and the approximation properties of piecewise polynomials, it will not be discussed in further detail here, but I refer to the textbook by Larson and Bengzon [70] or Süli and Mayers [71]. Instead, we will analytically go through the method for a simple case before discussing more complicated equations and how to implement them numerically.

3.2.1 Simple example

A simple example of the FEM is found from setting ourselves the realistic goal of solving the second order ordinary differential equation

$$\frac{\mathrm{d}^2u(\xi)}{\mathrm{d}\xi^2} - k^2(\xi)u(\xi) = f(\xi), \tag{3.19}$$

where the unknown function u is called the *trial function*. The Neumann boundary conditions at the edges of our one-dimensional system, defined on the interval $\xi \in [0, l]$, are

$$\frac{\mathrm{d}u}{\mathrm{d}\xi}\Big|_{\xi=0} = \alpha, \qquad \frac{\mathrm{d}u}{\mathrm{d}\xi}\Big|_{\xi=l} = \beta. \tag{3.20}$$

We write the equation on its variational form by multiplying both sides with a general function $v(\xi)$, known as the *test function*, and integrating over our domain

$$\int_0^l v\frac{\mathrm{d}^2u}{\mathrm{d}\xi^2}\mathrm{d}\xi - \int_0^l k^2vu\mathrm{d}\xi = \int_0^l vf\mathrm{d}\xi. \tag{3.21}$$

The double derivative can be removed through integration by parts, where the boundary terms are fixed from the Neumann boundary conditions (3.20)

$$\int_0^l \partial_\xi v\partial_\xi u\mathrm{d}\xi + \int_0^l k^2vu\mathrm{d}\xi = -\int_0^l vf\mathrm{d}\xi + v(l)\beta - v(0)\alpha. \tag{3.22}$$

As we see, the Neumann boundary conditions are naturally included in the equation itself. To continue, we let the trial function be written in terms of n basis functions ϕ_j with a constant unknown coefficient a_j,

$$u = \sum_{j=0}^{n} a_j\phi_j. \tag{3.23}$$

The functions ϕ_j make up a finite set of linearly independent functions, often referred to as the *Galerkin basis functions*. Writing the solution in terms of the Galerkin basis functions is the only approximation done in the FEM. Our test function v was an arbitrary function, and can therefore be chosen to be any of the basis functions, an aribtrary ϕ_i,

$$a_j\int_0^l \phi_i'\phi_j'\mathrm{d}\xi + a_j\int_0^l k^2\phi_i\phi_j\mathrm{d}\xi = -\int_0^l \phi_i f\mathrm{d}\xi + \phi_i(l)\beta - \phi_i(0)\alpha. \tag{3.24}$$

This equation can be written as a vector-matrix multiplication equation

$$A\boldsymbol{a} = \boldsymbol{b}, \tag{3.25}$$

where $\boldsymbol{b}$ is the known source vector, sometimes referred to as the *load vector*, $\boldsymbol{a}$ is the vector of unknown coefficients, and A is the *stiffness matrix*. To solve the equation, we choose, as an example, the hat functions displayed in figure 3.4, as the bases functions ϕ_i. There are many different possible basis functions, where the hat functions are the simplest

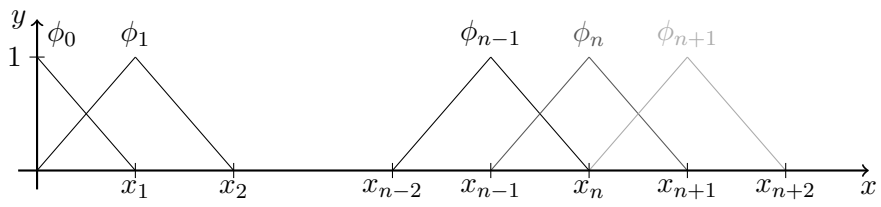

Figure 3.4: An illustration of the chosen basis functions ϕ_i, known as hat functions. The extremal value of ϕ_i is located at x_i with a value of 1, and is zero at all points beyond $x_{i\pm1}$. At the boundary of the parameter space only half of the basis function is used, and elsewhere all basis functions overlaps with neighbouring basis function $\phi_{i\pm1}$. With increasing number of hat functions used to approximate the solution, the error decreases.

case. One can increase the polynomial degree of the basis, which imparts increasing the number of coefficients per element. The elements, giving rise to the name of the method, are the combination of both the spatial interval for the basis functions and the type of basis function used. The hat functions chosen here are zero everywhere, except on the interval $[x_{i-1}, x_{i+1}]$, where they change linearly to a maximum value of 1 at the point x_i.

We see that $\phi_i(0) = \delta_{i,0}\phi_0$ and $\phi_i(l) = \delta_{i,n}\phi_n$, such that the Neumann boundary conditions act only on the first and last element of the source vector,

$$\left(\int_0^l \phi_i'\phi_j' \mathrm{d}\xi + \int_0^l k^2\phi_i\phi_j \mathrm{d}\xi\right) a_j = -\int_0^l \phi_i f \mathrm{d}\xi + \beta\phi_n\delta_{in} - \alpha\phi_0\delta_{i0}. \tag{3.26}$$

Due to the overlapping nature of the basis functions we can immediately see that A will be a tri-diagonal matrix. If we assume a constant step length $x_i - x_{i-1} = \Delta$, and a constant coefficient k, we find that the matrix A, for a (5×5) case is

$$A = \frac{\Delta}{6}\begin{bmatrix} 2 & 1 & 0 & 0 & 0 \\ 1 & 4 & 1 & 0 & 0 \\ 0 & 1 & 4 & 1 & 0 \\ 0 & 0 & 1 & 4 & 1 \\ 0 & 0 & 0 & 1 & 2 \end{bmatrix} + \frac{k^2}{\Delta}\begin{bmatrix} 1 & -1 & 0 & 0 & 0 \\ -1 & 2 & -1 & 0 & 0 \\ 0 & -1 & 2 & -1 & 0 \\ 0 & 0 & -1 & 2 & -1 \\ 0 & 0 & 0 & -1 & 1 \end{bmatrix}. \tag{3.27}$$

Here we have approximated all the integrals using the trapezoidal rule, with an error estimate of $\mathcal{O}(\Delta^3)$. The matrix representing the double derivative is identical to the one used in a finite difference method, when one discretizes the double derivative and writes it on a matrix form. The differential equation has now become an algebraic matrix-vector equation for the unknown coefficient of the vector $\boldsymbol{a}$. To find the coefficient, one has to invert the A-matrix, and the approximate solution can be represented in the original form through equation (3.23).

When solving a set of N coupled equations, which we will do later, the unknown vector will contain the n unknown coefficients for all N functions, making it Nn long. Likewise, the matrix will become an $Nn \times Nn$-matrix, where the tridiagonal elements give the terms from the stiffness matrix, and the non-tridiagonal elements will determine the coupling between the equations. To find the form of the equation, the same procedure as above can be followed.

3.2.2 More complicated equations

The FEM is more general than the example given. For partial differential equations, the procedure remains the same, as the variational formulation of the equation must be found by multiplying the equation with a test function and performing a volume integral over the domain, where double or higher-order derivatives are removed through integration by parts. The only difference is the number of dimensions for the basis functions, which must then match the number of dimensions of the trial function. Instead of hats, one works with Pyramids, with an arbitrary number of corners matching the mesh. An example of such a basis is displayed in figure 3.5, where we see that a single scalar value still defines the basis function for each element, but it spans a two-dimensional grid.

The equations we will solve in this thesis are all two- or three-dimensional, and slightly more complicated than the one presented above. The variational form of the dimensionless Navier-Stokes equations (2.3,2.23), is

$$\mathrm{Re}\int_\Omega v\dot{u}_i + \mathrm{Re}\int_\Omega v u_j \nabla_j u_i + \int_\Omega \nabla_j u_i \nabla_j v - \int_\Omega P\nabla_i v = \int_\Omega f_i v + \int_{\partial\Omega} v\hat{n}_j \nabla_j u_i. \quad (3.28)$$

Where the no-slip Dirichlet boundary condition (2.20) for u_i must be stated explicitly through the polynomial space where we look for solutions, and the arbitrary boundary condition for the pressure is chosen to be the no-flux boundary condition. The incompressibility of the fluid (2.4) has to be solved simultaneously, with the test function q

$$\int_\Omega q\nabla_i u_i = 0. \quad (3.29)$$

For Brenner's equation (2.92b, 2.92c) the Neumann boundary conditions (2.92c) are included naturally into the variational form

$$\mathrm{Pe}\int_\Omega v u_i \nabla_i B + \int_\Omega \nabla_i B \nabla_i v = \mathrm{Pe}\int_\Omega u'_x v + \int_{\partial\Omega} \hat{n}_i \hat{x}_i v, \quad (3.30)$$

where $\hat{x}_i$ is the basis vector in the x direction, and $\hat{n}_i$ is the normal unit vector of the boundary. For the above equations numerical implementation using the FEM is more complicated, and numerically expensive to run, and we will therefore use the numerical framework `FEniCS`.

3.2.3 FEniCS

FEniCS simplifies the numerical implementation of the FEM through a high-level Python package interface, which runs the more heavy computational tasks in C++. As input, one needs to define the mesh, the variational form of the equation, Dirichlet boundary conditions, and the problem's geometry. FEniCS takes this problem and rewrites it to a linear matrix equation, which is efficiently solved in the C++ back-end using optimized linear solver libraries. FEniCS also allows for simple parallelization through MPI, such that the code can be run in parallel on clusters. The equation to solve is implemented numerically by writing it on the form

$$a(u, v) = L(v), \quad (3.31)$$

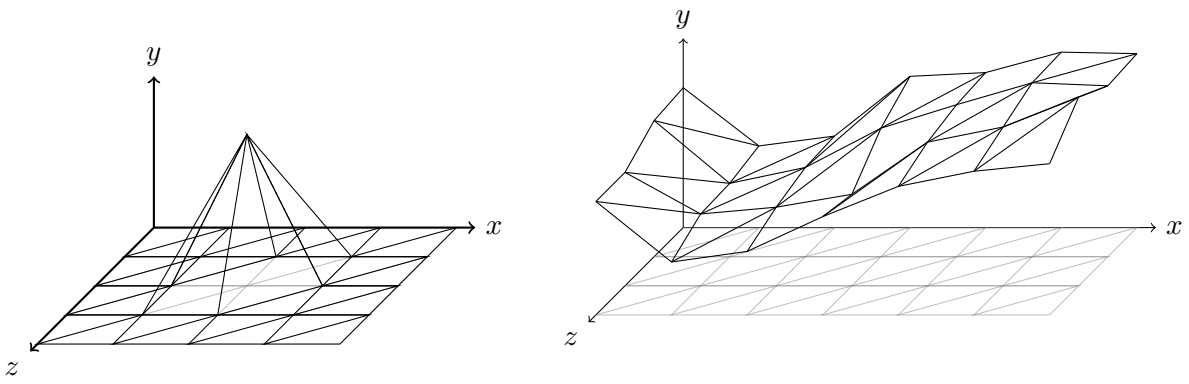

Figure 3.5: The basis function for the two-dimensional hat functions are displayed to the left, and to the right an example of a solution once the coefficients of the basis functions are found. The 1D-line of triangles has become six-sided pyramids with corners on a triangular lattice.

where the problem is to find u in a function space V, for all v in a function space $\hat{V}$. The form of a and L is seen from the equations, and are referred to as bi-linear and linear form, respectively. For a more in-depth description and tutorial for FEniCS, I refer you to the standard textbooks on the topic [72, 73].

3.2.4 Time dependent equations

For the time-dependent NS, we will solve the spatial equation for each time step using the FEM, but solve the temporal evolution using a finite difference method. The time derivative is then approximated using Newton's definition of the derivative

$$\partial_t u_i = \frac{u_i^k - u_i^{k-1}}{\Delta t}. \tag{3.32}$$

The superscript denotes the velocity field at two different time steps k and $k-1$, separated by a time Δt. To solve the problem, one must have an initial state for the $t = 0$ velocity field, which is then used to solve for the next time step using the FEM. To avoid non-linearity in the time evolution, we combine an implicit and an explicit method for the $u_j \nabla_j u_i$ term in the NS equations, which can be done while still achieving stability [74]. This is done by writing one of the velocity factors in an implicit way using Crank-Nicolson (CN) discretization, and the other factor in an explicit way using Adams-Bashforth (AB) discretization, defined as

$$u_i^{k,\mathrm{CN}} = \frac{1}{2}\left(u_i^k + u_i^{k-1}\right) \qquad u_i^{k,\mathrm{AB}} = \frac{1}{2}\left(3u_i^{k-1} - u_i^{k-2}\right). \tag{3.33}$$

The NS-equations then takes the form

$$\mathrm{Re}\left(\frac{u_i^k - u_i^{k-1}}{\Delta t} + u_j^{k,\mathrm{AB}} \nabla_j u_i^{k,\mathrm{CN}}\right) = \nabla^2 u_i^{k,\mathrm{CN}} - \nabla_i P^k. \tag{3.34}$$

This does not have to be taken care of for the $u_i \nabla_i B$ term in Brenner's equation, as the velocity field is known before solving for B. We will also work with time-dependent Brenner theory, summarized in section 4.2.1 on page 54, and derived in appendix A on page 101, which contains a time derivative on the same form as equation (3.32). When implementing this equation numerically, the same procedure as above will be followed, but since the equation (4.10) is linear in the unknown B, the combination of Crank-Nicolson and Adams-Bashforth does not have to be used.

3.2.5 Structure of program

Naturally, all known parameters must be defined, like the external force, geometry, and the spatial resolution of the mesh. With the `dolfin` package, the mesh is constructed, periodic boundaries are defined, and a boolean function to know if a mesh point is on the boundary or not must be written. Furthermore, `dolfin` is used to define the functional space for the trial function on the mesh, V, and the function space for the test function $\hat{V}$. For our investigation, n-th degree piecewise polynomials called Lagrange elements are used, where the hat functions used above would be a particular case for $n = 1$, in one dimension. When solving the NS equations, third degree polynomials have been used for the velocity and second degree has been used for the pressure. It is necessary to have a higher degree polynomial for the velocity to satisfy the Babuska-Brezzi condition, such that the linear system is non-singular and stability is achieved [75]. Similarly, the Brenner field is found with second-order polynomials. With the possible Neumann boundary conditions included, the variational equation is defined in terms of the trial and test function. Possible Dirichlet boundary conditions are not naturally included in the variational form and must therefore be stated explicitly. The FEniCS package contains a built-in solver for both linear and non-linear variational problems, where the Dirichlet boundary conditions and possible Jacobians are given as arguments, in addition to the variational equation and the unknown to solve for. The unknown is then found from calling the solver and saved to a file. For a more detailed description, I again refer you to the `Git`[2] repository of this thesis, where all code is included.

3.2.6 Comparison between the LBM and the FEM

The LBM differs fundamentally from the FEM and most other numerical methods. Instead of starting with the Navier–Stokes equations and discretizing them, one simulates particle collisions on the mesoscopic scale and find that the macroscopic averaged quantities satisfy the Navier–Stokes equations. No discretization is performed, and all boundary conditions must be implemented in particle-collision rules. With such a fundamentally different approach compared to other methods, such as finite difference, element or volume, comes both advantages and disadvantages.

An advantage of being based on the Boltzmann equation, instead of the equations of fluid mechanics, is that the method is fully explicit, with only local interactions, making it easy to parallelize. In addition, the boundary conditions are implemented by defining

[2] `https://github.com/ivarhaugerud/master`

the rules for boundary nodes, which makes complex geometries easy to implement. While this could also be said for the FEM, its implementation becomes very difficult without relying on established numerical frameworks. Thus, with the LBM it is simpler to write code at competitive speeds independently from scratch. Additionally, since each collision at each lattice point conserves both momentum and mass, they are excellently conserved throughout the simulation. A disadvantage with the LBM is that one cannot perform simulations at zero Reynolds number or infinite Peclet number, which can often act as a bench-marking limit. The LBM performs more FLOPS and consumes more memory per time step compared to the FEM [67]. Additionally, it is naturally time-dependent, making it less efficient for solving stationary flows [67], but it is easier to parallelize to compensate for this drawback.

An extensive part of our work is done on advection-diffusion in long periodic geometries, where the LBM for advection-diffusion would be expensive. If one were to use the LBM for this purpose, one would have to collide and stream particles at thousands of nodes in hundreds of unit cells for each time step, where most lattice points would be approximately zero. This problem is avoided by using RW simulations on the velocity field instead, where the periodicity allows us to only work inside a single unit cell.

An advantage of the FEM is that it can easily be extended to different equations than the Navier-Stokes equations. While it might be possible to solve Brenner's equations using the LBM, it is not trivial what collision rules must be used to retrieve the correct equation, especially the boundary conditions, and one has to perform a Chapman-Enskog analysis to verify the rules. Therefore, the process of implementing it is much more tiresome than it is for the FEM, where one only needs to find the equation on its variational form.

With this in mind, the FEM is always used when working with Brenner theory, and combined with RW simulations on the velocity field found with the finite element method. Hence, the LBM is only used when studying the reciprocal relation, but is then used to solve the Navier-Stokes equations and the advection-diffusion equation. In this part of the work, the periodicity of the unit cell is not of importance, and one is generally working in a smaller spatial domain, which makes the LBM method highly suitable.

3.3 Random walks to simulate the advection-diffusion equation

Random walk (RW) methods are intuitive and direct ways to simulate diffusive processes. Their main advantage is their simplicity; they are easy to implement, and therefore work well as a relatively simple and fully independent way to verify theoretical predictions based on a continuum description. In RW simulations, the diffusive movement is modelled through a stochastical term which changes the particle positions by a random number in each direction at each time step, similar to the Langevin-equation (2.30). To include the advection of a background velocity field, one has to include the velocity field in the equation of motion. This can be written mathematically by performing a short-time integration of

the Langevin equation with stokes drag (2.49), from t to $t + \mathrm{d}t$ (2.50), yielding

$$\boldsymbol{x}(t + \mathrm{d}t) = \boldsymbol{x}(t) + \boldsymbol{u}(\boldsymbol{x}, t)\mathrm{d}t + \mathrm{d}\boldsymbol{W}(t). \tag{3.35}$$

The vector $\boldsymbol{W}$, called a Wiener process, is an uncorrelated stochastical noise term in our equation. There are two main discretization methods when implementing this equation numerically, Itô and Stratonovich discretization. We will use the Itô discretization method, which is a fully explicit discretization method, where we evaluate the Wiener vector at the current time step when finding the next position

$$x_{i,n+1} = x_n + u_i(\boldsymbol{x}_{i,n}, t_n)\Delta t + \Delta W_i(t_n), \tag{3.36}$$

where i is a component of the position vector, and n is the time index, separated by a short-time interval Δt to neighbouring index values. The Stratonovich discretization, on the other hand, is an implicit discretization method, where the Wiener vector will be evaluated at an intermediate time step. The difference between the two discretization methods becomes relevant when the Wiener vector is spatially dependent, as the two discretization methods then produce different steady states. This is called the Itô-Stratonovich dilemma and is a general problem when dealing with discretization in stochastical calculus; see the review article by Manella and McClintock [76] for further discussion. As we will not deal with spatially dependent diffusion coefficients, the dilemma is of no inconvenience. The Wiener vector can be regarded as a short-time integral over a Langevin force, and its ensemble averages must therefore equal those defining a Langevin force (2.31)

$$\langle \Delta W_i(t_n) \rangle = 0, \qquad \langle \Delta W_i(t_n) \Delta W_j(t_m) \rangle = \sigma^2 \delta_{jk} \delta_{nm}. \tag{3.37}$$

Assuming the collisions are independent events, the Wiener process must be Gaussian, and is therefore defined by its first two moments [59]. For a Gaussian variable ξ, with zero mean $\langle \xi \rangle = 0$ and unity variance $\langle \xi^2 \rangle = 1$, we define the Wiener vector as

$$\Delta W_i(t_n) = \sqrt{2D_m \Delta t}\, \xi_i(t_n), \tag{3.38}$$

which achieves the correct diffusion coefficient when comparing with theory. The number $\xi_i(t_n)$ is drawn from a Gaussian distribution with the above properties at each time step for each particle and dimension.

For passive Brownian particles, one can first find the velocity field using the LBM or FEM and then perform the updating scheme for the random walkers by interpolating the velocity field over the lattice points. We use a bounce-back boundary condition for the random walkers, similar to what we defined for the LBM, where they move back to their previous position if they move out of the domain.

Chapter 4

Results and Discussion

With the theoretical background and numerical methods established, we continue by presenting the results of this thesis. The results from the three areas of investigation will be presented and discussed separately, with an overall conclusion in the next chapter.

4.1 Dispersion in channels with rough square boundary

Following the result from Aris [20], among others [25, 26], we look for an effective diffusion coefficient on the form

$$D_{\parallel} = D_m \left(\frac{\mathcal{D}_{\parallel}(b)}{D_m} + \kappa \mathrm{Pe}^2 g\left(\mathrm{Pe}, \mathrm{Re}, b\right) \right). \tag{4.1}$$

The geometric factor g measures the flow's effect on the asymptotic spreading as a function of the Peclet number, Reynolds number and roughness amplitude b. The constant κ is the geometric factor from the Taylor-Aris result, which for a two-dimensional straight channel takes the value of $2/105$, such that $g\left(\mathrm{Pe}, 0, 0\right) = 1$. We have also defined $\mathcal{D}_{\parallel}$ as the effective diffusion coefficient for pure diffusion at a roughness b, such that one retrieves the correct value in the limit of zero Pe. The effective dispersion has therefore been decomposed into one term, $\mathcal{D}_{\parallel}$, representing the effect of horizontal purely diffusive transport which is important at small Peclet numbers, and another term representing the effect of flow, where a scaling of order Pe^2 similar to Taylor-Aris, is expected.

An illustration of the two-dimensional rough channel is given in figure 4.1 on the next page, which is solely defined by the boundary square length b, with an average channel half-width of 1. To understand dispersion phenomena in rough channels, the velocity field is found by numerically solving the incompressible time-independent Navier–Stokes equations for various boundary amplitudes and Reynolds numbers. The average velocity is always normalised to 1, and increasing the Reynolds number, defined as $\mathrm{Re} \equiv U/\nu$, is therefore done by varying the kinematic viscosity ν. Different transport rates are investigated in a wide range of Peclet numbers, defined as $\mathrm{Pe} \equiv U/D_m$, where the diffusion coefficient D_m is varied. By varying the diffusivity of momentum and mass, the Reynolds and Peclet numbers are changed independently. The investigation is therefore for various Schmidt

numbers, defined as Sc ≡ Pe/Re. The range of parameters investigated should represent the values of the Schmidt number similar to that found in nature [37, 77]. The study is purely numerical, using the finite element method described in section 3.2 on page 31, and convergence is verified by ensuring the average velocity and effective diffusion coefficient changes by less than 1% by doubling the spatial resolution of the finite element mesh.

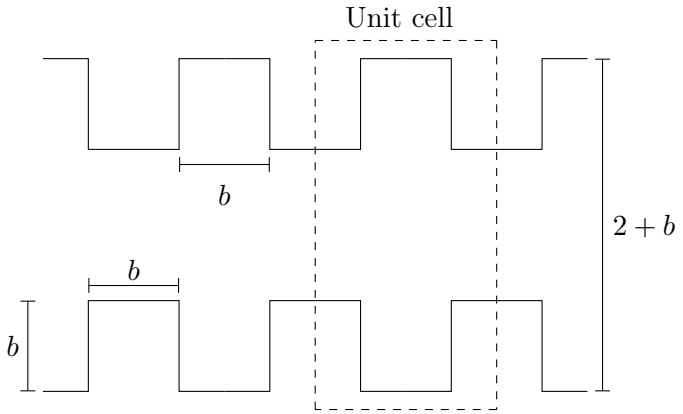

Figure 4.1: Illustration of the two-dimensional square rough channel, consisting of infinitely many repeated unit cells. The parameter b characterizes the roughness and solely defines the geometry. For $b = 0$ one finds Aris' channel, and for $b = 2.0$ the channel is completely closed.

4.1.1 Velocity field

In figure 4.2 the lower half of the velocity field is visualised for a set of roughnesses $b = 0.4$, 0.8 and 1.6, and Reynolds number of 0 and 31 in the left and right column, respectively. For $b = 0.4$, the recirculation zones (RZ) are close to filling the whole cavity area, independent of the Reynolds number. The flow profile in the centre of the channel takes the form of Poiseuille flow, with something similar to a lid-driven flow [78] for the cavity. With increasing roughness, the central streamlines move further into the cavities, reducing the relative size of the RZ compared to the cavity area. For a Reynolds number of 31, this is no longer the case, as the RZ fills to whole cavity area independent of the roughness. The increase in RZ area with Reynolds number is the largest at the largest roughness, where even additional RZ are observed in the form of Moffat eddies [79] in the corners of the cavity. A consequence of the discontinuous geometry is that recirculation zones appear even at small roughnesses, independently of the Reynolds number, filling the whole cavity.

4.1.2 Validation of Brenner solver

To validate our Brenner equation solver, the asymptotic effective diffusion coefficient from Brenner's equation is compared with the one found by performing random walk simulations and the well established Taylor-Aris result [20] for a flat channel. The effective diffusion coefficient found using the two different methods agree well and are displayed as a function of the roughness b without and with flow in figure 4.3 and 4.4 respectively. From the

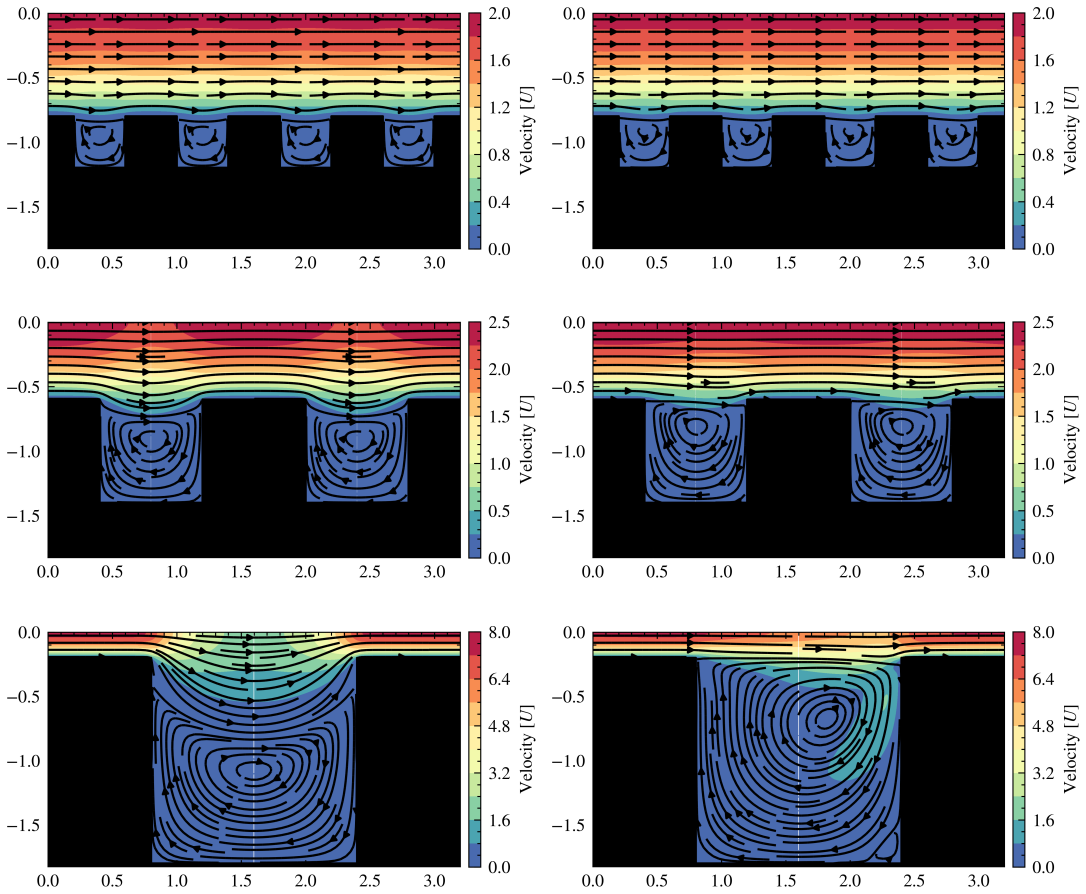

Figure 4.2: Visualization of the lower half of the velocity fields at different roughness and Reynolds number. For each sub-figure the spatial axis are scaled equally, and the average velocity is normalised to 1. The left and right columns have a Reynolds number 0 and 31 respectively. At the top row, with $b = 0.4$, the flow does not change notably with the change in Reynolds number, and the flow profile can be separated into a Poiseuille flow in the central channel, and something similar to a lid-driven flow [78] inside each cavity. At zero Reynolds number we see that increasing the roughness to 0.8, middle, and 1.6, bottom, makes the unit cell wider, such that the central streamlines go further inside the cavity, reducing the relative area of the RZ. This behaviour is not observed for higher Reynolds number, where the RZ almost fills the whole cavity for all roughnesses.

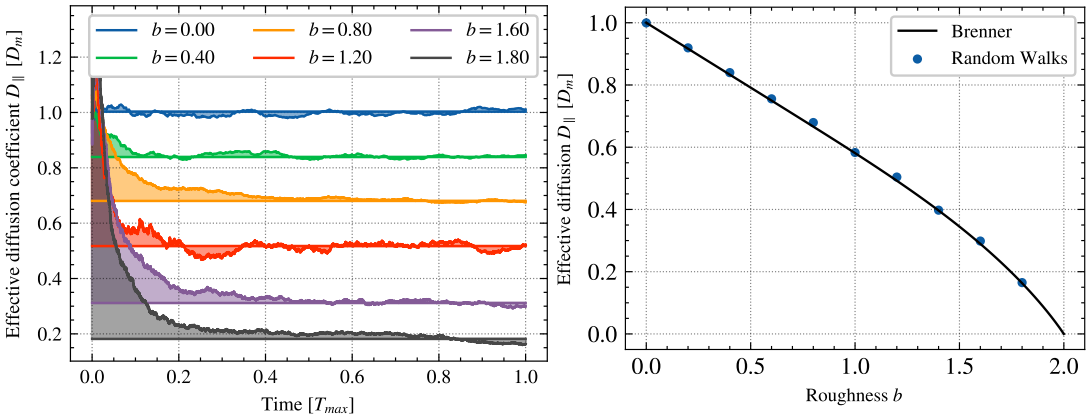

Figure 4.3: A comparison between the effective diffusion coefficient found by numerically solving Brenner's equation and RW simulation in the absence of advection is displayed. In the left figure, the average of the last third of the datapoints are used to measure the effective diffusion coefficient, resulting in the constant line displayed in the same figure. The values of the effective diffusion coefficient found using the two methods are in excellent agreement, and decreases linearly until around $b = 1$ with a slope of -0.42, and approaches zero when the channel is closed.

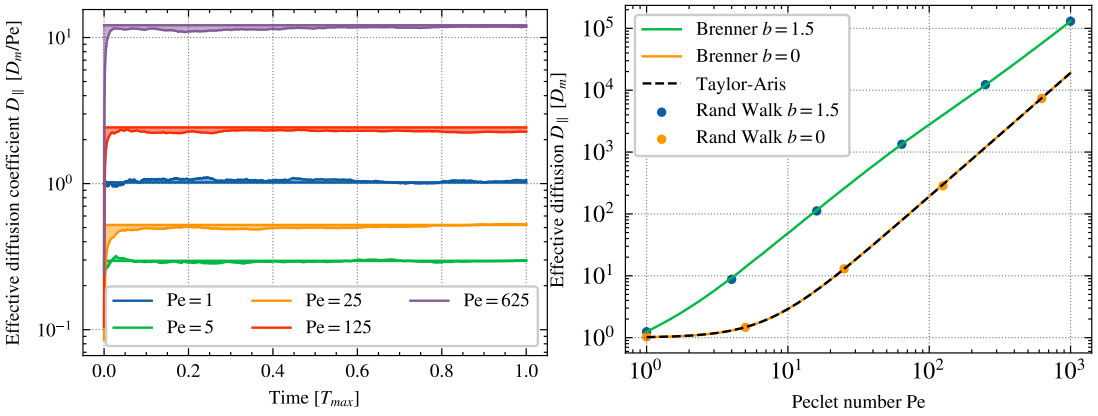

Figure 4.4: A comparison between the effective diffusion coefficient found by numerically solving Brenner's equation and RW simulation in the presence of advection is displayed. In the left figure, the constant line is the value found using Brenner's theory, and the average of the last third of the RW data points are used to measure the effective diffusion coefficient. The values of the effective diffusion coefficient found using the two methods are in excellent agreement and agree with the Taylor-Aris result (2.69) at $b = 0$. The agreement extends to the case with a varying boundary of $b = 1.5$.

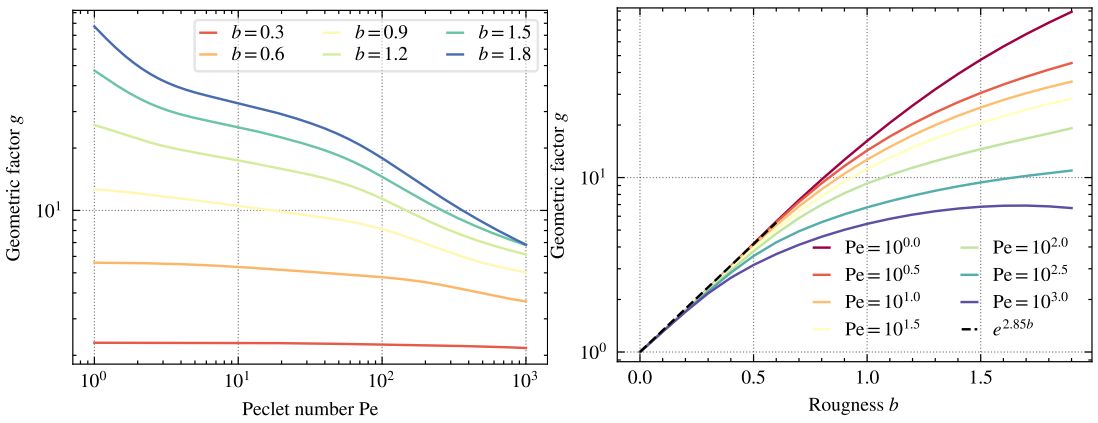

Figure 4.5: In the left figure, all of the curves are approximately linear with some oscillation around the straight line. Increasing the roughness size makes the spreading more efficient, while an increase in the Peclet number results in a decrease. The dependency on Peclet number is weak for small roughnesses, but increases with larger roughnesses. For the largest Peclet numbers, g moves closer to 1, meaning more similar to the Taylor-Aris result. To the right, we see that for small Peclet numbers, the geometric factor scales as $e^{2.85b}$ but begins to decrease with larger roughness. The slopes eventually decrease for all curves, with a larger decrease with larger Peclet numbers.

excellent agreement, we conclude that the Brenner equation solver is correct, and it will therefore be used for the following results, as it is much more efficient than performing RW simulations.

4.1.3 Effective dispersion for creeping flow

With a working solver of Brenner's equation, the effective diffusion coefficient at zero Reynolds number is calculated as a function of both the Peclet number and roughness, the resulting geometric factor (4.1) is displayed in figure 4.5. The effective dispersion is independent of the Peclet number at small roughnesses where a scaling of $e^{2.85b}$ is seen, and begins to decrease with the Peclet number at larger boundary amplitudes. The effective dispersion is monotonically increasing with the roughness except for at the largest Peclet number and roughness, where a slight decrease is found.

Even though the geometric factor is always larger than 1, the effective dispersion is not necessarily larger than the Taylor-Aris result (2.69). In figure 4.6 on the following page, the relative change in the effective dispersion from Poiseuille flow to our geometry is displayed. A slight decrease is observed when both transport methods are of equal importance, $\mathrm{Pe} = 1$, due to the horizontal diffusive spreading being limited by the varying boundary amplitude. This decrease is not monotonic and becomes positive at $b = 1.25$. The relative change is maximised for an intermediate value of $\mathrm{Pe} = 31$. Except for $\mathrm{Pe} = 10^3$, the relative change is the largest for the largest boundary amplitude.

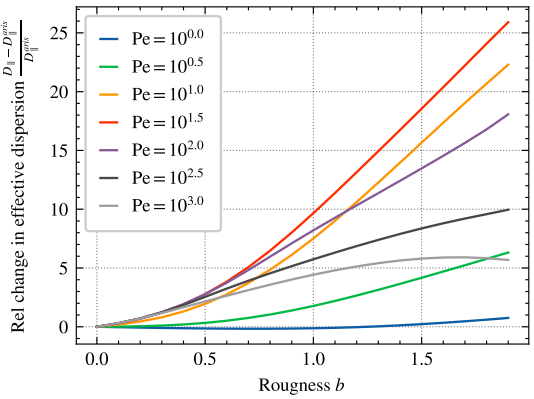

Figure 4.6: The relative change in the effective diffusion in our geometry, in comparison to the Taylor-Aris result, is positive for almost all curves except Pe = 1, which is negative for $b < 1.25$. Additionally, the relative change is maximized for an intermediate value of Pe = 31. The relative change is always at its maximum for the largest boundary amplitude, except for the Pe = 1000 curve.

4.1.4 Effective dispersion for inertial flow

In figure 4.7, the relative change in $D_{\parallel}$ when increasing the Reynolds number is displayed. For each sub-figure, the Peclet number is constant while varying the flow parameters of roughness and Reynolds number. For all Peclet numbers, the curves are independent of the Reynolds number until around $b = 0.5$. Assuming that RZ are the main mechanism determining the asymptotic dispersion, the result agrees with the relative RZ area being independent of the Reynolds number at these values of the boundary amplitude. Additionally, no relative change is seen for small values of the Reynolds number, as one would expect. The dependence on the Reynolds number becomes more complicated for larger roughness. Larger Reynolds numbers can result in the dispersion increasing or decreasing, depending on the Peclet number. When the advective and diffusive transport is similar, the additional RZ from an increase in Reynolds number always amplifies the dispersion and further increases for larger roughnesses. When advective transport dominates, the same change in flow results in a decrease in the effective diffusion coefficient. The maximum decrease for Pe = 100 is almost 50%, while the largest positive increase is observed to be around half that, at 25%.

4.1.5 Random walk analysis

By analysing the positions and trajectories found from random walk simulations, a physical explanation for the behaviour observed above can be found. We are especially interested in understanding how an increase in Reynolds number can increase or decrease the effective dispersion, depending on the Peclet number. Therefore, the simulations are performed for a small value of the Reynolds number, zero, and a large value, 31, which are the same values for which the streamlines in figure 4.2 are displayed. Three different orders of magnitudes of the Peclet number are also investigated, 1, 10 and 100, corresponding to the left column

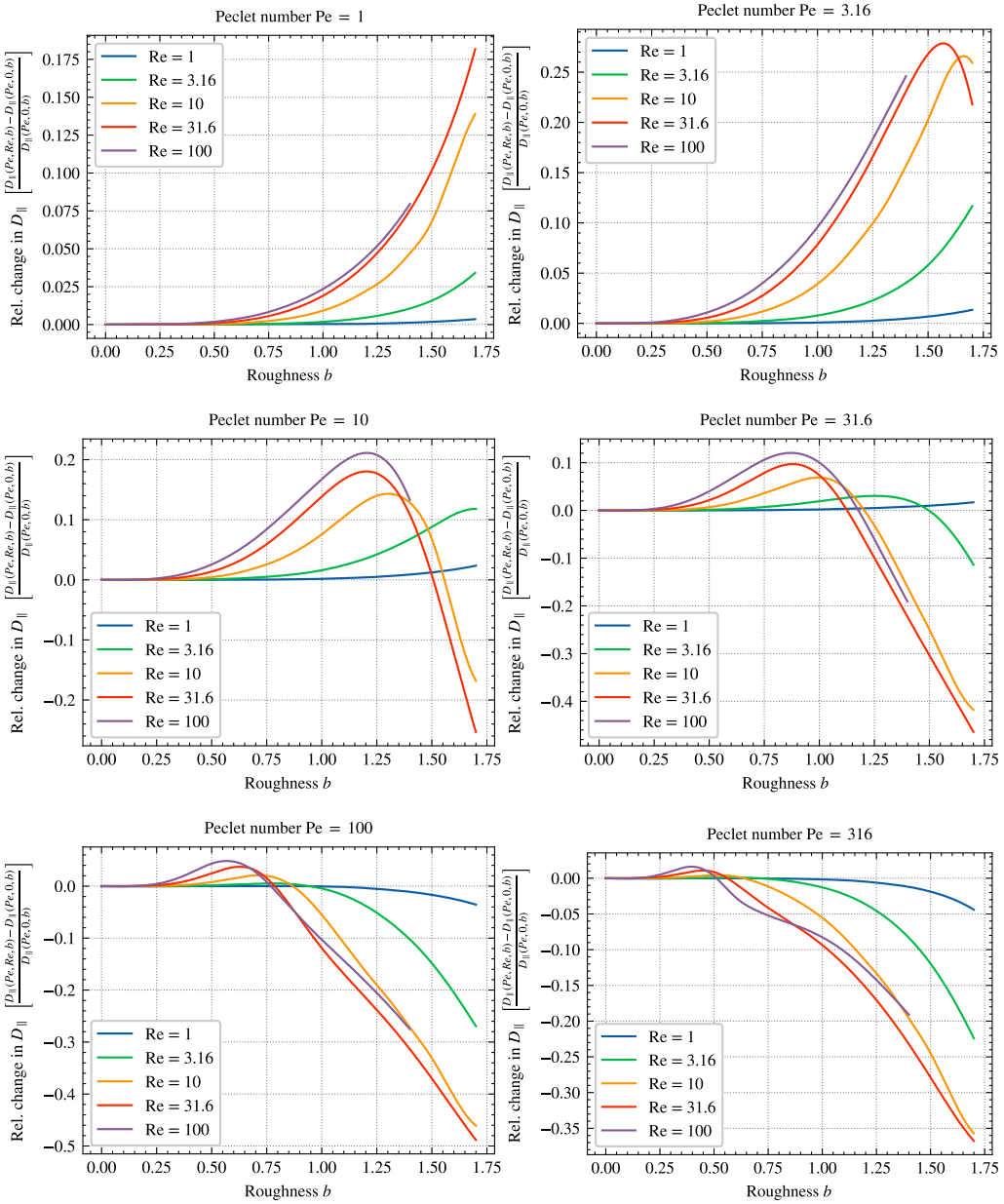

Figure 4.7: For small boundary amplitudes, $b < 0.5$, there is no noticeable relative change in the effective dispersion, independent of both the Peclet and Reynolds number. When the advective and diffusive transport rates are similar, the dispersion increases with the Reynolds number, and is further increased at larger roughnesses. When increasing the Peclet number, the relative change in $D_\parallel$ starts to decrease at the largest roughnesses. The negative values are found for smaller roughnesses when further increasing the Peclet number. For $\mathrm{Pe} = 10^2$ the relative change is almost strictly negative, with a maximum decrease of 50%, much larger than the maximum relative increase observed for $\mathrm{Pe} = 1$. When transport by flow dominates over diffusive transport, an increase of the Reynolds number reduces the effective dispersion.

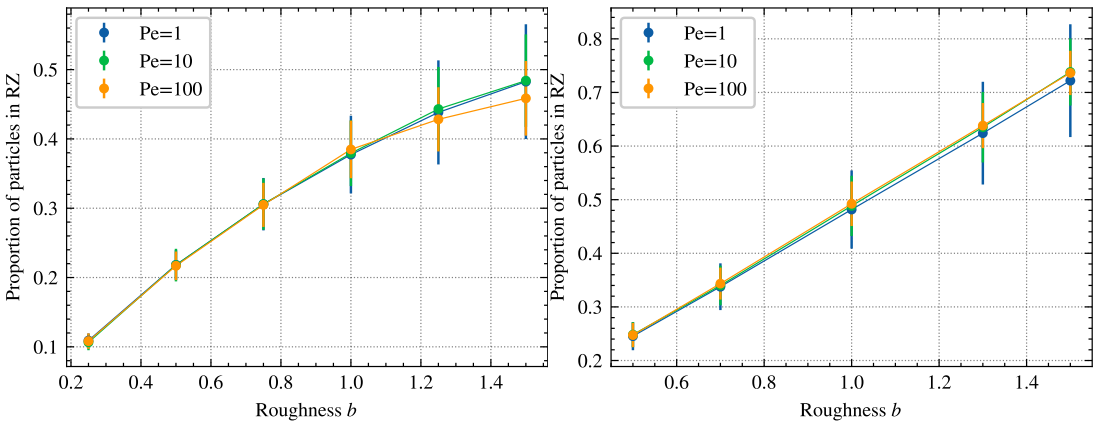

Figure 4.8: The average number of particles in RZ is found to flatten out with an increase in the roughness for Re = 0 (left), while increasing linearly for Re = 31 (right). This behaviour is consistent with the behaviour of the RZ area, inferred from figure 4.2 on page 41. For both cases the effect of changing the Peclet number is negligible compared to the fluctuations around the averaged values.

in figure 4.7 on the previous page.

By finding the shape of the RZ, the average number of particles in the RZ is measured and displayed in figure 4.8. The proportion of particles always increases for creeping flow, although the slope decreases for the largest boundaries. For a Reynolds number of 31, on the other hand, the linear increase matches the fact that the RZ fills the whole cavity area, which is $b/2$ of the total unit cell area. Additionally, the proportion reaches a value of 0.72, compared to 0.50 reached for creeping flow. For both figures, the results are approximately independent of the Peclet number. The error bars give the standard deviation around the average occupation number.

By calculating a histogram for the occupation time in the RZ and the central channel (CC), one finds an exponential decay on the form $\exp\{-t/\tau\}$. This is displayed for the RZ occupation times for Re = 0 and Re = 31 at Pe = 10 in figure 4.9 on the next page, where the characteristic occupation time is measured from the slope of the straight line. For the set of Peclet numbers, Reynolds number and roughness investigated above, we want to find the behaviour of the characteristic occupation time τ both within and outside of the RZ. The characteristic occupation time in the RZ and CC is displayed respectively in figure 4.10 and 4.11. Starting with the RZ occupation times, we see that increasing the Peclet number or roughness results in an increase of τ. Since the transport mechanism to enter and leave RZ is diffusion, it makes sense that increasing the Peclet number results in transitions from one region to the other being less frequent. The scaling, on the other hand, seems to be proportional to the Peclet number with an exponent slightly smaller than one. The characteristic occupation time in the channel, on the other hand, tends to decrease with the roughness but increase with the Peclet number. This effect is more apparent at Pe = 100, where τ goes from 12 to 4 for the roughness values investigated here.

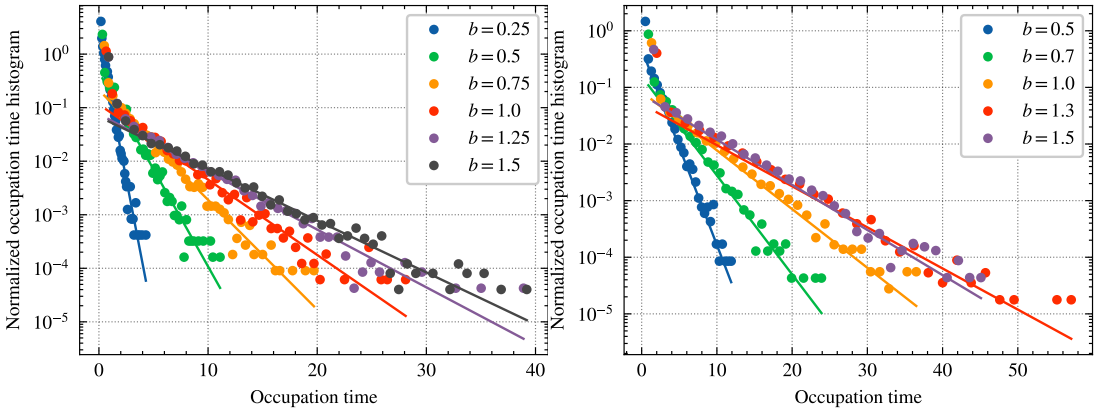

Figure 4.9: The histogram of occupation times in the RZ follows an exponential decay, where the characteristic time is given by the best fit slope, displayed as the straight line. Both figures have a Peclet number of 10, with creeping flow to the left, and a Reynolds number of 31 in the right.

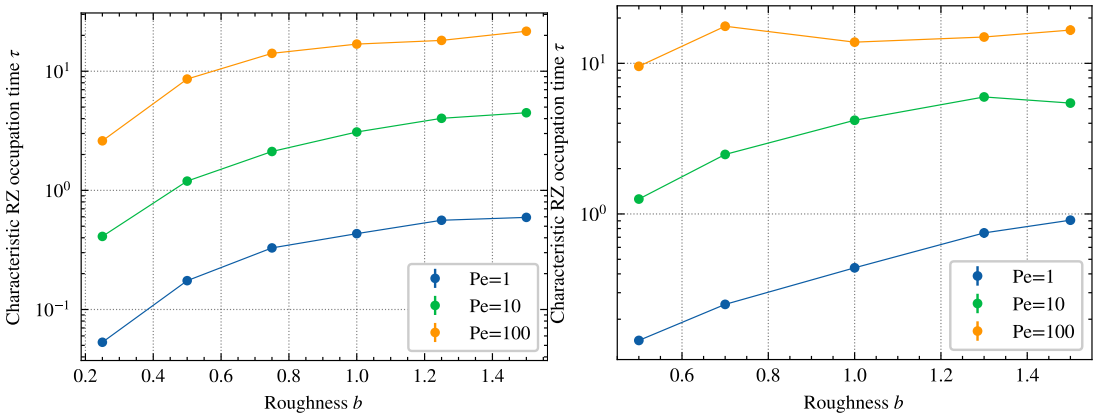

Figure 4.10: The probability of staying in a RZ follows an exponential decay, where the characteristic occupation time is seen to increase with both the Peclet number and the roughness, for both creeping flow (left) and inertial flow with Re = 31 (right), meaning the RZ are more difficult to escape.

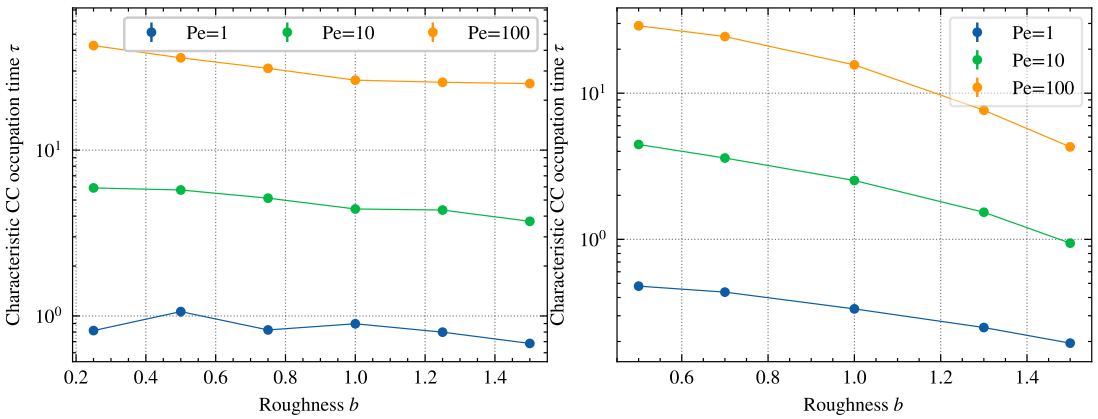

Figure 4.11: The probability of staying in the central channel (CC) follows an exponential decay, where the characteristic occupation time is seen to increase with the Peclet number and decrease with the roughness, for both creeping flow and inertial flow with Re = 31 (right). Although the behaviour is similar, the occupation times are more sensitive to changes in the roughness for inertial flows.

4.1.6 Discussion

Different contributions to the effective dispersion

The geometric factor g measures the deviation in asymptotic spreading relative to a straight channel, and therefore captures the effect of flow with a varying boundary amplitude on the dispersion. Phenomenologically, a varying boundary amplitude has four main consequences on the effective dispersion. The first consequence is larger velocity differences, hence more shear, inside the unit cell. Particles following streamlines close to the wall move much slower than those at the centre. Thus, the particles having stayed closer to the wall will have travelled much shorter than the latter, increasing the effective dispersion. In the limit of no shear in a straight channel, the effective dispersion is equal to the molecular one, independent of the Peclet number. Additionally, compression of streamlines at the pore throats makes vertical diffusive transport between streamlines more efficient. This, in turn, results in less efficient dispersion, as particles will deviate less from the mean velocity, as they are *sampling* the different velocities over the unit cell more efficiently. The effects are already explained in the established Taylor-Aris result (2.69), where an increase in shear increases the dispersion. In contrast, an increase in the diffusion coefficient, or decrease in the channel height, increases the vertical switching of streamlines through diffusive transport, thus reducing the effective dispersion. Depending on the magnitude of the two effects, the boundary can either increase or decrease the effective dispersion. The third consequence of a varying boundary on the effective dispersion is a reduction in horizontal diffusive transport. Previous work on the topic finds that small and smoothly varying boundaries reduce the effective dispersion quadratically with the boundary amplitude and linearly for discontinuous geometries, in the absence of advection[40]. This effect is only relevant when the transport rates are of a similar order, meaning a Peclet number of

order unity. The fourth and last consequence of a varying boundary is the appearance of recirculation zones. Particles in recirculation zones have no net advective transport along the channel. RZ, therefore, act as large zero-velocity regions, similar to the no-slip boundary layer of the fluid. Recirculation zones increase the effective dispersion drastically, as they can be hard to escape, contrary to the boundary layers of the fluid. In addition to appearing for larger boundary amplitudes, recirculation zones appear with fluid inertia at larger Reynolds number. The four contributing terms to the effective diffusion coefficient can be summarised in the following way: to maximise the dispersion, the average auto-correlation time for the advected horizontal velocity should be maximised, with a broad distribution in advection speed between particles. The effective dispersion will depend on all of the four competing effects, and each of them will contribute differently at different Peclet numbers, geometric roughness and Reynolds number.

Dispersion in creeping flow

The four different effects have been studied earlier for smoothly varying boundary amplitudes [25, 26]. For such geometries, accumulation of streamlines occurs at the pore throat, while the boundary amplitude is not large enough for recirculation zones to appear. If the additional shear is not enough to compensate, the effective dispersion can decrease relative to a straight channel [25]. The decrease in the geometric factor at small boundary amplitudes does not occur for the discontinuous boundaries studied here, as recirculation zones are present at all boundary amplitudes. Another consequence of the rough boundary is that the contraction of streamlines at the pore throat is small for low boundary amplitudes. From inspecting the streamlines in figure 4.2 on page 41, the flow is seen to be separated into a Poiseuille flow in the central channel and a lid-driven flow in the cavity. With increasing boundary amplitude and width of the unit cell, the two regions become more connected as the central streamlines go further into each cavity. Adding the negative contribution from the slight contraction of streamlines at the pore throats, and the positive contribution from recirculation zones and additional fluid shear, the effective dispersion increases monotonically with the roughness in this region of the parameter space. However, the full change decrease for $\mathrm{Pe} = 1$ due to the horizontal diffusion being limited by the varying boundary. This effect is more prominent for discontinuous boundaries due to $\mathcal{D}_{\parallel}$ being linear in the boundary amplitude [40]. Therefore, the competing effects for creeping flow are the negative contribution from the less efficient horizontal diffusion and the positive contributions from RZ and shear. Naturally, the latter becomes more important at larger Peclet numbers, and the change compared to Poiseuille flow is positive. The relative change in $D_{\parallel}$ becoming positive at $b = 1.25$ for $\mathrm{Pe} = 1$ is due to increased fluid shear and larger RZ. In figure 4.6 on page 44, the relative change is not maximised by maximising the Peclet number. It is maximised for an intermediate value of $\mathrm{Pe} = 31$, giving a factor of 27 more effective dispersion than Taylor-Aris dispersion with the same Peclet number. This is understood from figure 4.4 on page 42, where the scaling is similar for large Pe, and the constant offset is reached around $\mathrm{Pe} = 31$. The same fact was observed in sinusoidal channels with Stokes flow by Bolster et al. [25], without an explanation.

We observe that increasing the Peclet number reduces the geometric factor for creeping

flow, as seen in figure 4.5. The effect occurs at all roughnesses, but is magnified at larger values. This result can seem surprising, as the Peclet number magnifies the shear and importance of the flow field, which is highly dependent on the geometry. An explanation for this behaviour can be that the negative contribution from the accumulation of streamlines in the pore throats contributes more when the vertical diffusive transport rate is small compared to the advective transport rate. Additionally, both values of τ for creeping flow does not scale linearly with Pe, but with Pe^{α} with some exponent α slightly smaller than one, as seen in figure 4.10 and 4.11. For creeping flow, it seems as if data collapse can be made if one multiplies by $\mathrm{Pe}^{0.9}$, or some similar exponent, although three different values of the Peclet number are insufficient to state this definitively. While the geometric factor g decreases with the Peclet number, we must remember that the effective dispersion still increases as a factor of Pe^2 that has been factorised out.

Occupation times

By mapping all particle positions to the same unit cell, the non-equilibrium steady state will be a uniform distribution. This explains the first-order total moment in Brenner theory being Ut (2.85). Therefore, the relative occupations of the RZ in figure 4.10 on page 47 is a measure of the relative RZ area, which can be inferred from figure 4.2 on page 41. For small roughnesses with creeping flow, RZ fills the entire cavity, such that a linear increase of the relative RZ area with b is expected. When b increases further, the dipping of the streamlines into the cavity will reduce the slope with b. For $\mathrm{Re} = 31$, the RZ fills the cavity area for all roughnesses, such that a linear increase should persist for all b. This is consistent with the occupation numbers measured. There is an uncertainty in the average number of particles, quantified by the error bars, which gives one standard deviation away from the mean. There is an uncertainty of the separation between the CC and the RZ, resulting in further uncertainty in the occupation number.

With creeping flow, we find that the occupation times in the central channel decrease with b, while the occupation times in the RZ increase with b. A lower channel height makes it more likely for a particle to be close to the separation line between the two regions, reducing the occupation time in the central channel. Additionally, it is more difficult to escape RZ because the total RZ area increases. This effect might be slightly reduced since the contact length between the two regions also does increase with the roughness.

When increasing the Reynolds number, the occupation time in the RZ are almost unchanged. The characteristic occupation time in the central channel, on the other hand, decreases much more with increasing boundary roughness than at creeping flow. This large decrease with b can be understood from looking at figure 4.2 on page 41 for $b = 1.6$. For a particle located at the centre of the channel, the diffusive distance to reach a RZ is much shorter for inertial flow due to the streamlines not moving into each cavity. To enter a recirculation zone at creeping flow with a large Peclet number, the particle must be located along the wall at the end of the pore throat to be advected along with the boundary layer between the two regions. This makes it less likely to enter than for inertial flow. This explanation also agrees with the slope being more negative at larger roughnesses and Peclet numbers.

Effective dispersion with inertial flow

Bolster et al. [25] argues that increasing recirculation area increases the effective dispersion. In our geometry, increasing the Reynolds number keeps the velocity difference the same and increases the recirculation area. According to Bolster et al. [25], this would necessarily increase the effective dispersion. The same is also said by Bouquain et al. [26], who argue for a direct relation between the recirculation area and the effective dispersion coefficient; if the recirculation area increases, so must the effective dispersion. These statements contradict the relative change in the effective dispersion with Reynolds number, displayed in figure 4.7 on page 45, where an increase in the Reynolds number can both result in an increase or a decrease, depending on the Peclet number. Here, the relative decrease is the most interesting aspect of the figure, as it has not been observed previously and contradicts explanations from the literature [25, 26].

We aim to give an explanation of this decrease with Reynolds number, by investigating the change in characteristic occupation times for $\mathrm{Pe} = 100$ and $b = 1.5$, through RW analysis displayed in figure 4.8, 4.10 and 4.11. For this combination of parameters, increasing the Reynolds number does not change the characteristic occupation time of RZ, which is around 11 for both cases. At the same time, it increases the likelihood of entering a RZ significantly, as the characteristic time spent in the channel decreases from around 12 to 4. Increasing the Reynolds number makes it easier to enter and equally difficult to leave the RZ, such that on average, three-quarters of the particles are inside RZ and stay there three times longer than in the central channel. Furthermore, the mean position of the solute is dominated by particles stuck in RZ with zero horizontal velocity. The variance in position will increase slowly due to the majority of particles having zero effective horizontal velocity. Furthermore, the particles in the central channel quickly return to the recirculation zone. The decrease is due to the characteristic occupation time of the channel decreasing and most particles having zero net horizontal velocity. Following the summarised statement on maximising the effective dispersion, the above arguments can be formulated as follows: the autocorrelation time is the same for particles in RZ but decreases for particles in the CC. Additionally, the variance in velocity differences between particles is decreased due to 3/4 of the particles experiencing the same zero velocity in RZ at any given time. The two effects combined is ultimately believed to be the reason for the measured decrease. When visually inspecting the motion of the random walkers, their behaviour agrees with the explanation provided here. This explanation prompts the question of why one finds a relative increase in the effective spreading for low values of the Peclet number, as the RZ occupation is approximately the same as for $\mathrm{Pe} = 100$.

Although RZ contributes positively to the effective dispersion at low Peclet numbers, the contribution is much smaller than at larger Peclet numbers, simply due to the flow being a less prominent transport method. This is apparent in figure 4.6 on page 44, where the change in effective dispersion compared to the Taylor-Aris result is negative due to the varying boundary reducing horizontal diffusive transport, until RZ and additional fluid shear contribute enough to make the change in effective dispersion positive. Since diffusion is an equally important transport method, the reduced occupation time in the central channel does not limit the horizontal transport of the particles as much as it did for

Pe = 100. Instead, the contributions competing with the inefficiency of horizontal diffusive transport is enhanced, resulting in an increase.

Relation to other work

A recent publication by Yoon et al. [30] focused on dispersion under the combined effect of self-similar rough surfaces and fluid inertia. Their investigation was in the transient regime and focused on first passage times and transition times of their finite channels. Their investigation found that the increase of roughness and Reynolds number can increase or decrease the transport, depending on the Peclet number. When advective transport was dominating, Pe = 10^5, their channel is flushed efficiently due to RZ not being entered by the RW. The RZ are not entered at this Peclet number due to the region separating the RZ and the CC acting as a slip boundary moving at a large velocity. In our geometry, the roughness is larger, and the Peclet number is smaller than in their investigation. Therefore, their maximal RZ occupation is less than 25%, much less than what is observed here. Furthermore, RZ will be entered in the asymptotic regime, their findings are therefore only valid in the transient regime. The dynamics behind the transport efficiency increasing or decreasing depending on the Peclet number found here is different from the one in their investigation.

For creeping flow with small boundary amplitudes, or a Reynolds number of 31 with any boundary amplitude, the central streamlines do not move into the cavities, and therefore has a profile similar to that of Poiseuille flow in the central channel. In this regime, RZ are believed to be the primary mechanism affecting the dispersion. Therefore, much of the dynamics might be captured by modelling the RZ as absorbing boundaries with a characteristic waiting time. The exact shape of the RZ is not of importance, only their accessibility and characteristic occupation time. Levesque et al. [80] found an analytic expression for the effective dispersion in a two-dimensional channel with absorbing boundary. Their closed analytic form expressed the effective dispersion in terms of adsorption and desorption rates, similar to what we measured in figure 4.10 and 4.11. It is not trivial to map the characteristic occupation times measured for this model to the quantities used in their expression, but it could act as an interesting starting point for an analytic investigation.

Outlook

The geometry studied here is a prototype for a more general investigation into dispersion with a rough geometric profile, and more research on similar geometries is necessary to further understand its effect on dispersion. One starting point is turning the square roughness into rectangles, defined by two different length scales, as more parameters to vary might give a better understanding of the competing contribution to the effective dispersion. Dispersion with a sawtooth or triangle boundary, with the top and bottom boundary either in or out of phase, might exhibit some new and some similar properties as the square geometry, and should be explored, to give a broader understanding of rough surfaces. A geometry exhibiting both a smoothly varying and a discontinuous boundary, similar to what has been done for pure diffusion [40], could be used to investigate dispersion in dif-

ferent geometries transitioning from smooth to rough. Another aspect could be a unit cell that is not symmetric along the vertical axis, such that the effective dispersion would depend on the flow direction at non-zero Reynolds numbers. The perfect periodicity studied here is a simplification of naturally occurring rough surfaces, which are often statistically self-affine [81–83]. The effect on dispersion of a self-affine channel would give greater insight into dispersion phenomena in nature.

The Reynolds number studied here was relatively small compared to fully developed turbulence, typical for many real-world systems with rough boundaries. When increasing the Reynolds number further, the time derivative in the NS equations cannot be ignored, and the flow is no longer steady and laminar. The time-dependent Brenner theory, derived in appendix A on page 101, would allow the same method used here to be extended to higher Reynolds numbers. Even though Taylor dispersion at larger Reynolds number has been studied [84, 85], and was even investigated by Taylor himself [86], it is to our knowledge lacking in rough channels, and the geometry studied here can be further investigated. How the decrease in effective dispersion with Reynolds number behaves for larger values of both the Peclet and Reynolds number is hitherto unknown.

The geometry can be made self-similar by superimposing a smaller boundary of the same shape. A square with length $b/3$ can be placed at the bottom of the cavity and removed at the pore throats. This process can be repeated indefinitely, with the squares of the next fractal generation having lengths of $b/9$. Each new fractal generation will leave the total unit cell area unchanged but add additional discontinuities and RZ. This geometry was slightly investigated, but required larger numerical resolution to achieve convergence, especially with flow, a mesh with varying resolution would be needed. Hopefully, this investigation would result in the effective dispersion coefficient converging to a fixed value with increasing fractal generation to give insight into channels with roughness at all length scales.

Investigations in two-dimensional channels can seem artificial, but do provide insight into systems where the geometric variation in one direction is sufficiently larger than in the third direction. This could be applied to rock fracture and slickenline patterns [30, 87] and microfluidic devices [35, 47, 88], to mention some possibilities. Still, extension to three-dimensional geometries can provide additional effects, like vortices and crossing streamlines, which are known to impact the dispersion properties significantly [89, 90]. Therefore, the investigations performed here should be extended to the third dimension to give a broader understanding of dispersion phenomena in these geometries.

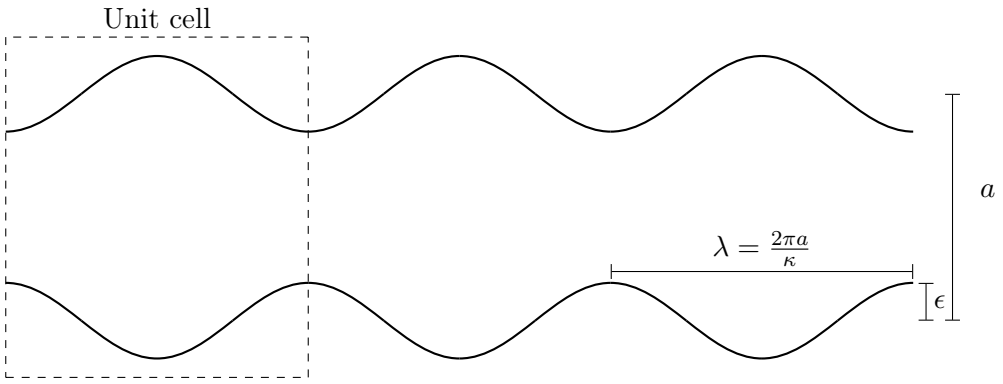

Figure 4.12: An illustration of the channel geometry with height a, boundary amplitude ϵ and wavelength λ in the untransformed coordinates.

4.2 Dispersion with an oscillating force in channels with sinusoidal boundary

Having investigated the effects of a discontinuous boundary roughness, we continue by letting the boundary vary smoothly along the flow direction and impose a time-dependent oscillating force to drive the flow. Here we present the perturbation method used, the generalisation of Brenner's theory to time-dependent flows, and its verification and application to our geometry.

4.2.1 Perturbation theory and time-dependent Brenner equations

To analytically investigate the interactions between an oscillating external body force on the fluid, and the resulting hydrodynamic dispersion in a channel with a smoothly varying boundary amplitude, we perform a coordinate transformation from the physical coordinates into dimensionless and rescaled coordinates. In the physical coordinates, the horizontal position is given by x, and the vertical position by y, with the boundary located at $y = a\left(1 \pm \epsilon \sin\left(2\pi x/\lambda\right)\right)$. An illustration of the channel in the physical coordinates is displayed in figure 4.12. The coordinates are rescaled to the vertical and horizontal coordinates, ξ and η, defined as

$$\xi \equiv \frac{y/a}{1 + \epsilon \sin\left(\frac{2\pi}{\lambda} x\right)} \qquad \text{and} \qquad \eta \equiv x/a. \tag{4.2}$$

In the transformed coordinates the boundary is located at $\xi = \pm 1$, and all lengths are measured in units of the channel height a. Additionally, the dimensionless wavenumber is defined as $\kappa \equiv 2\pi a/\lambda$. To be able to find analytic expressions, the geometry is perturbed in the boundary amplitude ϵ,

$$\frac{1}{1 + \epsilon \sin\left(\kappa\eta\right)} = \sum_{n=0}^{\infty} \left(-\epsilon \sin\left(\kappa\eta\right)\right)^n \approx 1 - \epsilon \sin\left(\kappa\eta\right) + \epsilon^2 \sin^2\left(\kappa\eta\right). \tag{4.3}$$

Due to the unit cell being invariant in the transition $-\epsilon \to \epsilon$, only even powers of ϵ will contribute to the spatial averages. We therefore need to perform the perturbation to second-order, with the advantage that our estimated error for spatially averaged quantities are of the order ϵ^4. All operators, boundary conditions, integrals and unknowns will be expanded in ϵ, identically to how the velocity field is written here:

$$\boldsymbol{u} = \boldsymbol{u}^{(0)} + \epsilon \boldsymbol{u}^{(1)} + \epsilon^2 \boldsymbol{u}^{(2)} + \mathcal{O}(\epsilon^3). \tag{4.4}$$

With this rewrite, one has to solve the equation for each matching order of ϵ, turning the difficult unperturbed problem into infinitely many easier problems, that increase in complexity with each power in epsilon. For more reading on perturbation theory I refer you to the book by Bender and Orszag [91].

The incompressible Navier–Stokes equations are solved in their complex form, such that the full solution of the equation is found by adding its complex conjugate,

$$\frac{1}{\nu}\partial_t \mathbf{u} - \triangle \mathbf{u} = -\boldsymbol{\nabla} P + \frac{1}{2}\hat{\mathbf{x}} F_0 e^{i\omega t}, \qquad \nabla \cdot \boldsymbol{u} = 0, \tag{4.5}$$

with the no-slip boundary conditions (2.20), where we have defined $\triangle \equiv \boldsymbol{\nabla}^2$. The body force F_0 is a redefinition of the physical force f_0 per unit volume, to be per density ϱ and kinematic viscosity $F_0 \equiv f/(\nu\varrho)$, the same scaling is performed on the physical pressure p, such that $P \equiv p/(\varrho\nu)$. In this approximation, we are assuming low Reynolds number flow and therefore neglecting the non-linear term. Since we are including the time derivative we still allow for large frequencies compared to the diffusion of momentum, producing non-reversible flows. The zeroth-order NS equations, meaning a flat channel, is

$$\frac{1}{\nu}\partial_t \mathbf{u}^{(0)} - \triangle^{(0)} \mathbf{u}^{(0)} = \frac{1}{2}\hat{\mathbf{x}} F_0 e^{i\omega t}, \qquad \nabla^{(0)} \cdot \boldsymbol{u}^{(0)} = 0. \tag{4.6}$$

Using the zeroth order incompressability, we find a gauge freedom in the pressure, that has been used to set it to zero. The first-order NSE is slightly more complicated

$$\frac{1}{\nu}\partial_t \mathbf{u}^{(1)} - \triangle^{(0)} \mathbf{u}^{(1)} + \boldsymbol{\nabla}^{(0)} P^{(1)} = \triangle^{(1)} \mathbf{u}^{(0)}, \qquad \nabla^{(1)} \cdot \boldsymbol{u}^{(0)} + \nabla^{(0)} \cdot \boldsymbol{u}^{(1)} = 0, \tag{4.7}$$

as the first-order pressure is now non-zero. The second, and final, equation to solve is

$$\frac{1}{\nu}\partial_t \mathbf{u}^{(2)} - \triangle^{(0)} \mathbf{u}^{(2)} + \boldsymbol{\nabla}^{(0)} P^{(2)} = \triangle^{(2)} \mathbf{u}^{(0)} + \triangle^{(1)} \mathbf{u}^{(1)} - \boldsymbol{\nabla}^{(1)} P^{(1)}, \tag{4.8}$$

where the incompressability is given by

$$\nabla^{(2)} \cdot \boldsymbol{u}^{(0)} + \nabla^{(1)} \cdot \boldsymbol{u}^{(1)} + \nabla^{(0)} \cdot \boldsymbol{u}^{(2)} = 0. \tag{4.9}$$

Since the form of the Navier–Stokes equations used here is linear, we can superimpose solutions with different frequencies to obtain a solution for an arbitrary forcing signal which can be decomposed into a sum of frequencies. A result of this work is therefore an analytic approximate velocity for low Reynolds number flow in a two dimensional channel with sinusoidal boundary, for an arbitrary sum of body force frequencies.

Brenner theory, presented and discussed in section 2.3.4 on page 19, is only valid for stationary flow, and was therefore generalised for the purpose of this investigation. This procedure provides a new theoretical framework for calculating the dispersion tensor in arbitrary periodic environments for time-dependent incompressible flow in any dimension. The full derivation is shown in appendix A on page 101, but will be summarised here.

The only change, in comparison with the previously known Brenner equation (2.92b), is a time derivative acting on the Brenner field,

$$\partial_t B + \mathbf{u}\cdot\boldsymbol{\nabla} B - D_m \triangle B = u_x', \quad \text{with} \quad \hat{\mathbf{n}}\cdot\boldsymbol{\nabla} B_x = \hat{n}_x, \tag{4.10}$$

where u_x' is the velocity field relative to the average unit cell velocity $u_x' = u_x - \langle u_x \rangle$. Since the Brenner field is time-dependent the dispersion matrix must be redefined by including a time-average for the limit to be well defined

$$\overline{D}_{ij} = \lim_{t\to\infty} \frac{1}{\tau} \int_t^{t+\tau} D_{ij}(t')\mathrm{d}t', \tag{4.11}$$

where the bar denotes the time-averaged quantity and τ is some characteristic time, for example the period of the flow. The effective dispersion tensor can be calculated from the Brenner field

$$\overline{D}_{ij} = \lim_{t\to\infty} D_m \left\langle \left[\delta_{ij} - \nabla_j \overline{B}_i - \nabla_i \overline{B}_j + \overline{\nabla_k B_i \nabla_k B_j}\right]\right\rangle. \tag{4.12}$$

The non-linearity in B when calculating the dispersion tensor means that we cannot superimpose different solutions of D_{ij} to find the effective diffusion for a specter of frequencies, and are therefore only calculating the effective dispersion for single frequency flow.

To calculate the dispersion tensor, we must first find the Brenner field, by solving the time-dependent Brenner equation (4.10). In our perturbation parameter, we find the zeroth order equation

$$\partial_t B^{(0)} + \mathbf{u}^{(0)}\cdot\boldsymbol{\nabla}^{(0)} B^{(0)} - D_m \triangle^{(0)} B^{(0)} = u_x'^{(0)} \quad \text{with} \quad \partial_\xi B^{(0)} = 0 \quad \text{on} \quad \partial\Omega. \tag{4.13}$$

The equation is complicated further at the first-order:

$$\begin{aligned}\partial_t B^{(1)} + \mathbf{u}^{(0)}\cdot\boldsymbol{\nabla}^{(0)} B^{(1)} - D_m \triangle^{(0)} B^{(1)} \\ = D_m \triangle^{(1)} B^{(0)} + u_x'^{(1)} - \mathbf{u}^{(1)}\cdot\boldsymbol{\nabla}^{(0)} B^{(0)} - \mathbf{u}^{(0)}\cdot\boldsymbol{\nabla}^{(1)} B^{(0)}.\end{aligned} \tag{4.14}$$

Here, the boundary condition takes the form $\partial_\xi B^{(1)}(\xi = \pm 1) = \mp\kappa\cos\kappa\eta$. Continuing to the second and final order, we have

$$\begin{aligned}&\partial_t B^{(2)} - D_m \triangle^{(0)} B^{(2)} + \mathbf{u}^{(0)}\cdot\boldsymbol{\nabla}^{(0)} B^{(2)} = D_m \triangle^{(1)} B^{(1)} + D_m \triangle^{(2)} B^{(0)} + u_x'^{(2)} \\ &+ \left(\mathbf{u}^{(1)}\cdot\boldsymbol{\nabla}^{(1)} + \mathbf{u}^{(0)}\cdot\boldsymbol{\nabla}^{(2)} + \mathbf{u}^{(2)}\cdot\boldsymbol{\nabla}^{(0)}\right) B^{(0)} + \left(\mathbf{u}^{(1)}\cdot\boldsymbol{\nabla}^{(0)} + \mathbf{u}^{(1)}\cdot\boldsymbol{\nabla}^{(0)}\right) B^{(1)},\end{aligned} \tag{4.15}$$

with the boundary condition $\partial_\xi B^{(2)} = 0$. From studying the above equations, we notice that overtones of the ground frequency will appear due to the $\boldsymbol{u}\cdot\boldsymbol{\nabla} B$ term. The addition

of a varying boundary therefore results in the effective diffusion coefficient consisting of infinitely many multiples of the ground frequency.

To arrive at the effective diffusion coefficient, one has to take the spatial average of the Brenner field over the unit cell. When taking the spatial averages, the Jacobian $a^2(1 + \epsilon \sin \kappa\eta)\mathrm{d}\eta\mathrm{d}\xi$, must be included in the integration. While this leaves the total area of the unit cell unchanged, it can effect the spatial average at second-order. At zero order in ϵ, the spatial average of a quantity f is given by

$$\langle f \rangle^{(0)} = \frac{1}{2} \int_{-1}^{1} \mathrm{d}\xi f^{(0)}, \tag{4.16}$$

where we have used that all zeroth order contributions are independent of η. The first-order average becomes

$$\langle f \rangle^{(1)} = \frac{\kappa}{4\pi} \int_0^{2\pi/\kappa} \mathrm{d}\eta \int_{-1}^{1} \mathrm{d}\xi \left[f^{(1)} + \sin \kappa\eta f^{(0)} \right] = \frac{\kappa}{4\pi} \int_0^{2\pi/\kappa} \mathrm{d}\eta \int_{-1}^{1} \mathrm{d}\xi f^{(1)}, \tag{4.17}$$

where we again have used that no zeroth order contributions will be independent of η. Going to second order adds an additional term

$$\langle f \rangle^{(2)} = \frac{\kappa}{4\pi} \int_0^{2\pi/\kappa} \mathrm{d}\eta \int_{-1}^{1} \mathrm{d}\xi \left[f^{(2)} + f^{(1)} \sin \kappa\eta \right]. \tag{4.18}$$

The geometry begins to affect the integral at second order, where first order contributions that are proportional to sin can contribute to spatial averages. Lastly the unit normal vector, evaluated at the boundary, is given by

$$\hat{\mathbf{n}}(\xi = \pm 1) = \mp \frac{\hat{\mathbf{y}} + \epsilon\kappa \cos \kappa\eta \hat{\mathbf{x}}}{\sqrt{1 + (\epsilon\kappa \cos \kappa\eta)^2}} \approx \mp \hat{\mathbf{y}} \mp \hat{\mathbf{x}} \epsilon\kappa \cos \kappa\eta \mp \hat{\mathbf{y}} \frac{\epsilon^2}{2} \kappa^2 \cos^2 \kappa\eta + \mathcal{O}(\epsilon^3). \tag{4.19}$$

The x-component of the unit normal vector for the boundary is of interest, as it is needed to specify the boundary conditions in Brenner's equations.

4.2.2 Velocity fields and pressure

The velocity fields and pressure is found analytically by solving the zeroth, first and second perturbative order of the Navier–Stokes equations. The equations are written in complex and dimensionless form, as in equation (4.5); thus one must add the solution's complex conjugate to find the physical description of the fluid. The zeroth order velocity field takes the form

$$u_x^{(0)} = \frac{F_0}{2\gamma^2} \left(1 - \frac{\cosh \gamma\xi}{\cosh \gamma} \right) e^{i\omega t}. \tag{4.20}$$

For ease of notation, we have defined the Womersley number (2.24), multiplied by a complex phase $\sqrt{i}$, as

$$\gamma \equiv \sqrt{i}\mathrm{Wo} = \sqrt{\frac{i\omega a^2}{\nu}}, \tag{4.21}$$

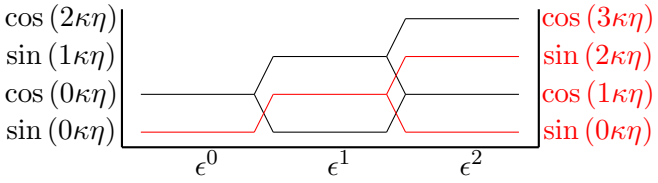

Figure 4.13: The horizontal wavelength is found to bifurcate to one higher and one lower value for each increase in the power of ϵ. Additionally, it changes from cos to sin and the other way around. The horizontal velocity field follows the black line, corresponding to the left vertical axis, while the pressure and vertical velocity field follow the red line with the right vertical axis.

The physical interpretation of γ, is the length that momentum diffuses over a period of flow, in units of the channel height. For most fluids and frequencies the Womersley number is small, such that one can perform a Taylor expansion in γ, resulting in

$$u_x^{(0)} \approx \frac{F_0}{4}\left(1-\xi^2\right)e^{i\omega t} - \frac{F_0\gamma^2}{48}\left(5-6\xi^2+\xi^4\right)e^{i\omega t}. \tag{4.22}$$

Here, the first term is identical to that of Poiseuille flow multiplied by a $\cos(\omega t)$, and the second term represents a latency in the fluid's response of the external force due to the diffusion of momentum not being instantaneous, reducing the velocity compared to regular Poiseuille flow. With our gauge freedom in P we choose for simplicity

$$P^{(0)} \equiv 0. \tag{4.23}$$

By going to second-order, the velocity field depends on the wavelength of the boundary κ and the horizontal coordinate η. The pressure is now non-zero and given by

$$P^{(1)} = \frac{1}{2}P_1\cosh(\kappa\xi)\,e^{i\omega t}\cos(\kappa\eta), \qquad P_1 \equiv \frac{\frac{\gamma F_0\tanh\gamma}{\kappa\cosh\kappa}}{1-\frac{\kappa'\tanh\kappa}{\kappa\tanh\kappa'}}. \tag{4.24}$$

Where we have defined a new quantity $\kappa' \equiv \sqrt{\kappa^2+\gamma^2}$. The horizontal component of the velocity is further expressed as

$$u_x^{(1)} = \left[\frac{P_1\kappa\cosh\kappa}{2\gamma^2}\left(\frac{\cosh\kappa\xi}{\cosh\kappa}-\frac{\cosh\kappa'\xi}{\cosh\kappa'}\right)+\frac{F_0\tanh\gamma}{2\gamma}\left(\frac{\cosh\kappa'\xi}{\cosh\kappa'}-\frac{\xi\sinh\gamma\xi}{\sinh\gamma}\right)\right]e^{i\omega t}\sin(\kappa\eta),$$

where we see that it is in phase with the boundary, while the vertical component is out of phase with the boundary

$$u_y^{(1)} = \frac{P_1\kappa\sinh\kappa}{4\gamma^2}\left[\frac{\sinh\kappa'\xi}{\sinh\kappa'}-\frac{\sinh\kappa\xi}{\sinh\kappa}\right]e^{i\omega t}\cos(\kappa\eta). \tag{4.25}$$

Going to second-order, we find a bifurcation of the spatial frequency, and a change from cosines to sines, and from sines to cosines, compared to the first-order result. The bifurcations holds for both the velocity field and the pressure, and is illustrated in figure 4.13 on

the facing page. This is for example seen in the second-order horizontal velocity

$$u_x^{(2)} = \frac{P_1 \sinh\kappa}{4\gamma^2}\left(\kappa'^2\xi\frac{\sinh\kappa'\xi}{\sinh\kappa'} - \kappa^2\xi\frac{\sinh\kappa\xi}{\sinh\kappa} - \gamma^2\frac{\cosh\kappa''\xi}{\cosh\kappa''}\right)e^{i\omega t}\cos(2\kappa\eta) \tag{4.26}$$
$$+\left[\frac{F_0}{8}\left(\xi^2\frac{\cosh\gamma\xi}{\cosh\gamma} - \frac{\cosh\kappa''\xi}{\cosh\kappa''}\right) - \frac{P_2\cosh 2\kappa}{2}\left(\frac{\cosh 2\kappa\xi}{\cosh 2\kappa} - \frac{\cosh\kappa''\xi}{\cosh\kappa''}\right)\right]e^{i\omega t}\cos(2\kappa\eta)$$
$$+\left[\frac{P_1\sinh\kappa}{4\gamma^2}\left(\kappa^2\xi\frac{\sinh\kappa\xi}{\sinh\kappa} - \kappa'^2\xi\frac{\sinh\kappa'\xi}{\sinh\kappa'} + \gamma^2\frac{\cosh\gamma\xi}{\cosh\gamma}\right) + \frac{F_0\cosh\gamma\xi}{8\cosh\gamma}\left(1-\xi^2\right)\right]e^{i\omega t},$$

where we have defined the new variable $\kappa'' = \sqrt{4\kappa^2+\gamma^2}$, in addition to

$$P_2 = \frac{\kappa}{\tanh\kappa'}\frac{P_1\kappa''\left[\kappa\cosh\kappa\tanh\kappa' - \kappa'\sinh\kappa\right] + \gamma^2\tanh\kappa''\tanh\kappa'\left[F_0 + 2P_1\sinh\kappa\right]}{2\gamma^2\left(2\kappa\tanh\kappa''\cosh 2\kappa - \kappa''\sinh 2\kappa\right)}, \tag{4.27}$$

which is also contained in the second-order pressure:

$$P^{(2)} = \frac{1}{4}\left(P_1\kappa\xi\sinh\kappa\xi + \frac{P_2\gamma^2}{\kappa}\cosh(2\kappa\xi)\right)e^{i\omega t}\sin(2\kappa\eta). \tag{4.28}$$

Finally, the vertical second-order velocity is

$$u_y^{(2)} = \left[\frac{P_1\kappa\sinh\kappa}{4\gamma^2\tanh\kappa'}\left(\kappa'\xi\frac{\cosh\kappa'\xi}{\cosh\kappa'} - \kappa'\frac{\sinh\kappa''\xi}{\sinh\kappa''} - \kappa\frac{\tanh\kappa'}{\tanh\kappa}\left(\xi\frac{\cosh\kappa\xi}{\cosh\kappa} - \frac{\sinh\kappa''\xi}{\sinh\kappa''}\right)\right)\right.$$
$$\left. - \frac{P_2\sinh 2\kappa}{2}\left(\frac{\sinh 2\kappa\xi}{\sinh 2\kappa} - \frac{\sinh\kappa''\xi}{\sinh\kappa''}\right)\right]e^{i\omega t}\sin(2\kappa\eta). \tag{4.29}$$

The expressions above describe the velocity field and pressure of the fluid, where terms of order ϵ^3 and higher are ignored. Due to the linearity of this form of the Navier–Stokes equations, any superposition with different frequencies and forces is also a solution.

4.2.3 Comparison with numerical solutions

To verify the analytical solution of the Navier–Stokes equations, they are solved numerically to compare the averaged kinetic energy

$$E_{\text{kinetic}} = \overline{\langle \boldsymbol{u}^2\rangle}, \tag{4.30}$$

where a factor of the density and a half is omitted. The average kinetic energy gives a single scalar quantity which can be compared to the one predicted by numerically solving the Navier–Stokes equations. When solving the equations numerically, we do not perform any perturbation assumptions and therefore expect a disagreement between the two methods with increasing boundary amplitude. Additionally, the $\boldsymbol{u}\cdot\boldsymbol{\nabla}\boldsymbol{u}$ term is neglected in the numerical solver, such that the disagreement must be due to the perturbative approach and the numerical resolution. An agreement for $\epsilon = 0$, where the velocity field is already

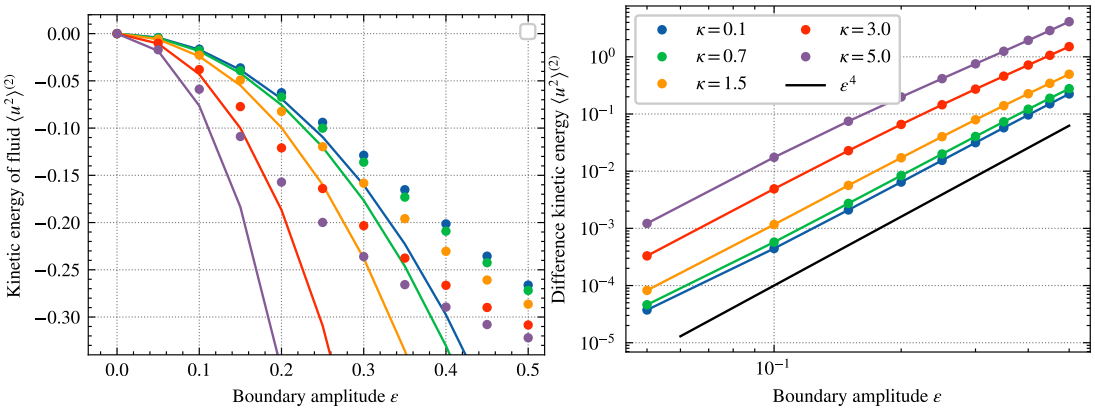

Figure 4.14: To the left, the second-order kinetic energy found numerically (dots) and analytically (lines) is seen to agree with each other, with the deviation increasing with ϵ. For short wavelengths, the deviation occurs for much smaller values of the boundary amplitude. To the right, the absolute value of the difference is displayed, where the continuous black line is the expected error of ϵ^4. Though the difference is larger than the expected error, the error increases with ϵ^4, and we conclude that the analytic velocity field is correct. The constant offset is likely due to the accuracy of the numerical solver and numerical integration of the analytic result and will depend on the parameters used. The parameters used in this plot are $\omega = 2\pi/5$, $F_0 = 3$, $\nu = 1.2$.

known, is expected. The kinetic energy found numerically and analytically is displayed in figure 4.14. For long wavelengths, the kinetic energy agrees well for boundary amplitudes up to around $\epsilon = 0.25$. For larger wavenumbers, a clear disagreement is seen already at a value of $\epsilon = 0.15$. Therefore, a more suitable expansion might be in small gradients, given by $\epsilon\kappa$. Notably, the deviation between the two follows the expected error of ϵ^4, where the constant offset is likely due to numerical inaccuracies in the numerical solver, integration of the analytic result and most importantly, the value of the chosen parameters. Furthermore, the analytic results have been verified by putting the solutions back in the original equation and using a symbolic calculation package, `sympy` to check if the left- and right-hand sides agree. With this in mind, we conclude that the perturbed velocity field is correct.

A visualisation of the perturbed velocity field in the physical coordinates is displayed in figure 4.15 on the next page for four different points in time. The velocity is maximised in the pore throats and minimised in the valleys, agreeing with our intuition. Still, a Poiseuille flow type behaviour is observed when the flow is fully developed, but slightly more complex behaviour is seen when the average velocity is close to zero. Small recirculation zones appear along the valley boundary, which then increases in size and moves towards the channel's centre, while the velocity field above and below is oriented in opposite directions. The recirculation zone eventually disappears, and the flow becomes fully developed. For a different set of parameters, with a larger viscosity, the recirculation zones do not appear, and the flow profile is close to a Poiseuille flow multiplied by a single $\cos \omega t$.

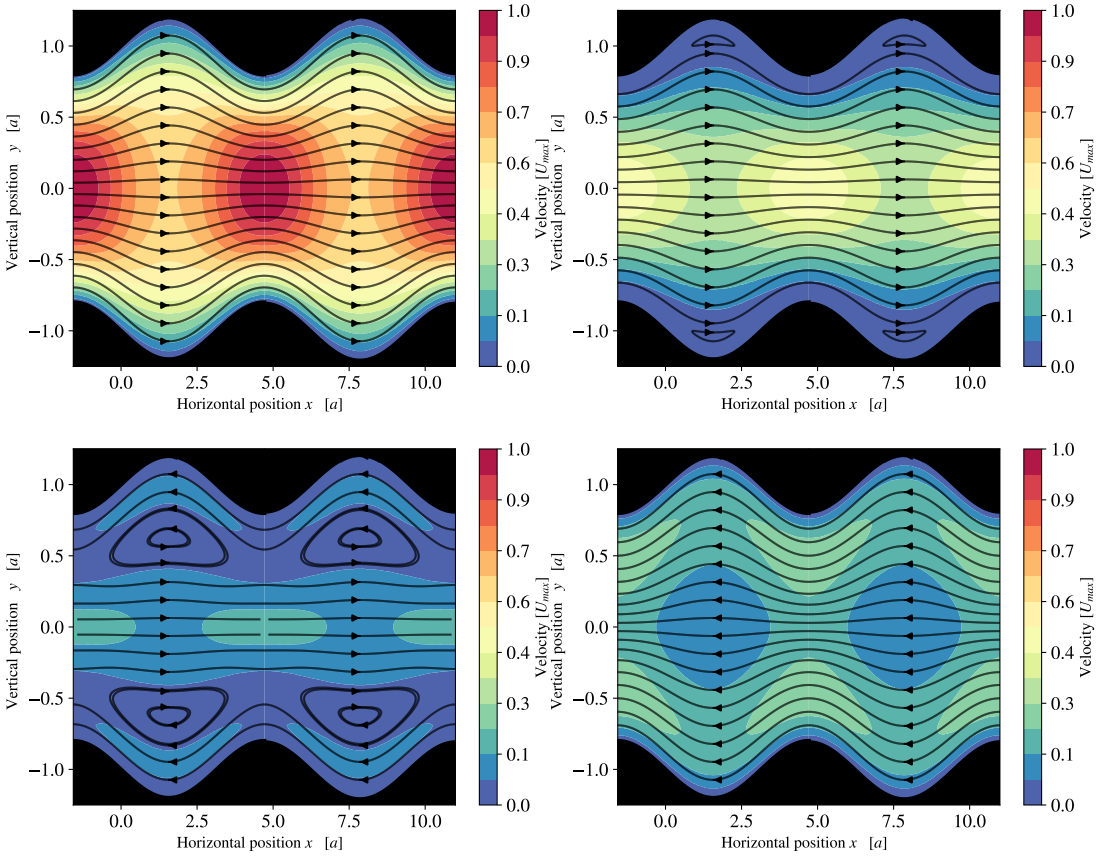

Figure 4.15: Visualization of the flow field, to second-order in the boundary amplitude, with $F_0 = 10$, $\omega = 2\pi/3$, $\kappa = 1$, $\nu = 5$, and $\epsilon = 0.2$. With the value of γ used here, the streamlines become slightly non-reversible, and interesting behaviour, different from regular Poiseuille flow, occurs when the unit cell average velocity is close to zero. The streamlines are transformed from the rescaled coordinates back into the physical coordinates through equation (4.2).

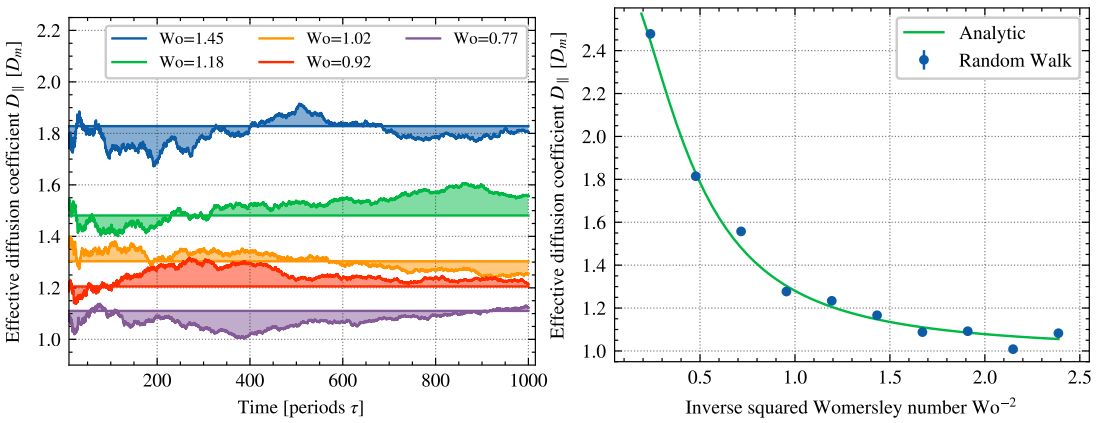

Figure 4.16: From numerical RW simulations with different Womersley numbers the effective dispersion coefficient is found, and compared with the analytical expression. The time evolution of the effective diffusion coefficient is seen to quickly approach the theoretical (straight) lines in the left figure, where the shaded area gives the deviation. Using the last half of the data-points the average and standard deviation is calculated and compared with the analytical result. The two methods agree, and we conclude that the analytical result is correct. The RW simulations were performed with $\omega = 2\pi/3$, $D = 0.25$, $F_0 = 10$, while varying ν.

4.2.4 Zeroth-order effective diffusion coefficient

The velocity fields found above can further be used as the source terms for time-dependent Brenner's theory (4.10). For a flat channel we find the Brenner field

$$B^{(0)} = \frac{\Lambda \tanh\gamma}{2\rho^2\gamma^3} e^{i\omega t} + \frac{\Lambda \tanh\gamma}{2\gamma\left(\rho^2-\gamma^2\right)}\left[\frac{\cosh\rho\xi}{\rho\sinh\rho} - \frac{\cosh\gamma\xi}{\gamma\sinh\gamma}\right] e^{i\omega t}. \tag{4.31}$$

For ease of notation, we have defined the diffusive Womersley number, with a phase factor $\sqrt{i}$ as

$$\rho \equiv \sqrt{i}\mathrm{Wo}_D = \sqrt{\frac{i\omega a^2}{D_m}}, \tag{4.32}$$

with the physically interpretation as the molecular diffusion length over a period, in units of the channel height. Additionally, a relation between the forcing and diffusivity is defined as $\Lambda \equiv a^3 F_0/D_m$, which can be interpreted as an effective Peclet number with a permeability K, such that $\Lambda = \mathrm{Pe}/K$. The value of K will depend on the Womersley number, boundary amplitude and wavenumber, and can be calculated from $\langle \boldsymbol{u}^2 \rangle$. From the Brenner field, we calculate the effective diffusion coefficient parallel with the flow, as a special case of equation (4.12),

$$\frac{D_\parallel^{(0)}}{D_m} = \left\langle 1 - 2\nabla_x^{(0)} B^{(0)} + \left(\nabla^{(0)} B^{(0)}\right)^2 \right\rangle = 1 + \left\langle \left(\partial_\xi B^{(0)}\right)^2 \right\rangle. \tag{4.33}$$

Calculating the derivative of the Brenner field, and solving the integral, gives the time-averaged contribution to the effective dispersion

$$\frac{D_{\parallel}}{D_m} = 1 + \frac{\Lambda^2 \tanh\gamma \tanh\gamma^*}{4\gamma\gamma^* \left(\gamma^4 - \rho^4\right)} \left(\frac{1}{\gamma^2} \left[\frac{\gamma}{\tanh\gamma} - \frac{\gamma^*}{\tanh\gamma^*} \right] - \frac{1}{\rho^2} \left[\frac{\rho}{\tanh\rho} - \frac{\rho^*}{\tanh\rho^*} \right] \right). \quad (4.34)$$

One can also calculate the oscillations around the time-averaged value, with a frequency doubling compared to the frequency of the body force

$$\begin{aligned} \frac{D_{\parallel}^{amp}(t)}{D_m} = \frac{\Lambda^2 \tanh^2\gamma}{4\gamma^2 \left(\gamma^2 - \rho^2\right)^2} e^{2i\omega t} \Bigg(& \frac{1}{\rho \tanh\rho} - \frac{1}{\sinh^2\rho} + \frac{1}{\gamma \tanh\gamma} - \frac{1}{\sinh^2\gamma} \\ & + \frac{4}{\gamma^2 - \rho^2} \left(\frac{\rho}{\tanh\rho} - \frac{\gamma}{\tanh\gamma} \right) \Bigg). \end{aligned} \quad (4.35)$$

Performing a Taylor expansion in both γ and ρ, meaning the frequency is small in comparison to the diffusion of both momentum and mass, we find that the full effective diffusion coefficient can approximately be written as

$$\frac{D_{\parallel}}{D_m} = 1 + \frac{2\Lambda^2}{105} \frac{\cos^2(\omega t)}{9} + \mathcal{O}\left(\gamma^2, \rho^2\right). \quad (4.36)$$

For this flow K takes a value of $1/3$, such that the result is identical to the Taylor-Aris result of $2/105$. For small Womersley numbers, the diffusion of momentum is instantaneous compared to the channel height and flow frequency, making the time derivative in the NS equations unimportant. Thus, the flow is approximately equal to that of Poiseuille flow with a factor oscillating in time, as we can see from its Taylor expansion in γ from equation (4.22). In the limit of small ρ, the frequency is much smaller than the molecular diffusion coefficient in units of the channel height, such that the particles have time to diffuse the channel height multiple times over a single period. This results in the solute reaching an asymptotic effective spreading in a time interval where the velocity field is almost stationary. Thus, an effective diffusion coefficient equal to that of the Taylor-Aris result is realized for each time frame, with a body force of $F_0 \cos(\omega t)$. The total effective spreading is therefore Taylor dispersion for each scaling of the force. Writing this result in the physical units, we find

$$\frac{D_{\parallel}}{D_m} = 1 + \frac{2}{105} \frac{a^6 f_0^2 \cos^2(\omega t)}{9\varrho^2 \nu^2 D_m^2} + \mathcal{O}\left(\frac{\omega a^2}{\nu}, \frac{\omega a^2}{D_m} \right), \quad (4.37)$$

which is completely symmetric in D_m and ν, meaning the diffusion of momentum is equally important as the diffusion of mass for the effective dispersion. For the case of large ρ and γ, where the frequency ωa^2 is much larger than both D_m and ν, we find the frequency scaling

$$\frac{D_{\parallel}}{D_m} - 1 \propto \frac{1}{\sqrt{\nu}\omega^{7/2}} \frac{1 - \sqrt{\frac{D_m}{\nu}}}{1 - \frac{D_m^2}{\nu^2}} \propto \omega^{-7/2}. \quad (4.38)$$

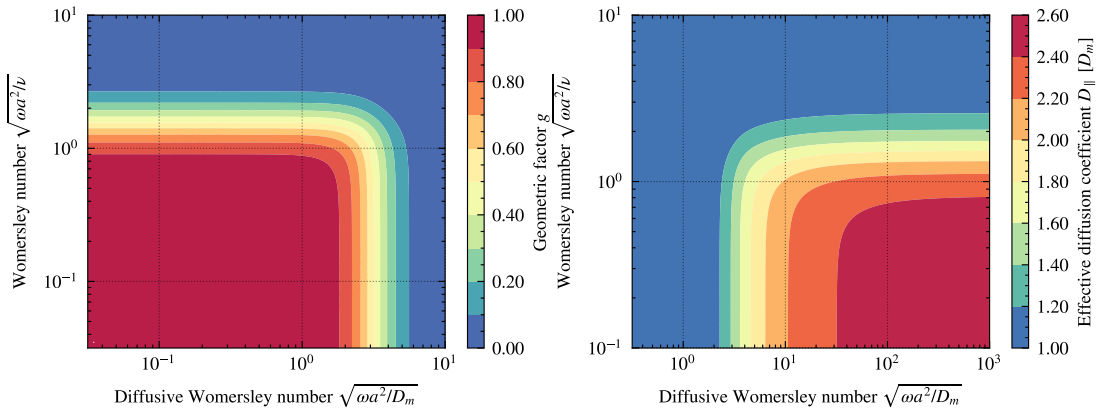

Figure 4.17: When varying the two different timescales, the maximal effective dispersion is found for large values of the diffusive Womersley number, even though the geometric factor is close to zero. The complete opposite behaviour is due to the Peclet number increasing with decreasing ρ, such that the inefficient geometric characteristics is compensated for by the horizontal transport being primarily advective, with inefficient diffusive vertical transport. The parameters used are $F_0 = 3$, and $\omega = 1$, while varying both ν and D.

For large frequencies, the effective spreading quickly approaches the molecular diffusion coefficient. This is due to two different effects. One, particles diffusing slowly compared to the frequency cannot change streamlines during a single period. Thus each particle will experience the average speed of their streamline over a period, which always is zero. Therefore, the spreading should be equal to the value without flow, consistent with the expression. The second effect is that in the limit of large Womersley numbers, the diffusion of momentum does not have time to respond to the change in external force, such that the flow never fully develops. This results in a small average velocity with little shear, and dispersion is therefore just due to molecular diffusion.

To verify the analytic expression for the effective diffusion coefficient, it is compared with the one found using random walk simulations. The comparison is displayed in figure 4.16 on page 62, where we see an excellent agreement when varying the Womersley number. From this data, we conclude that the zeroth-order result for the effective diffusion coefficient is correct. Our result is also in agreement with previous work [43]. The generalised Brenner theory is therefore verified for flat boundaries.

The effect on the dispersion from varying the two different time scales, γ and ρ, is displayed in figure 4.17. To the left, the dimensionless geometric factor g, which measures the change in effective dispersion compared to the Taylor-Aris result, defined as

$$\frac{D_\parallel}{D_m} = 1 + \frac{2\mathrm{Pe}^2}{105}\frac{g}{2}, \tag{4.39}$$

is displayed. The factor of $1/2$ makes a value of $g = 1$ retrieve the Taylor-Aris result for the mean value of the effective dispersion. To compare with the Taylor-Aris result, we

define the Peclet number for oscillating flows as

$$\mathrm{Pe} \equiv \frac{a\sqrt{\overline{\langle \boldsymbol{u}^2 \rangle}}}{D_m}. \tag{4.40}$$

To reach the saturation value of $g = 1$, the time scales for diffusion of momentum and mass relative to the channel height must be larger than the frequency. The threshold value for the transition from 0 to 1 occurs at a smaller value for ρ than for γ, meaning the diffusion of momentum is more important than the diffusion of mass to reach a non-zero effective dispersion. Additionally, if the Womersley number is smaller than 1, it no longer affects the value of g or the transition interval from 0 to 1 when varying ρ. The dispersion is quickly saturated, and increasing either of the time scales will no longer affect the dispersion.

The effective dispersion is plotted to the right in the same figure while varying the same parameters. The almost mirror-symmetric behaviour in the two figures is due to varying the diffusive Womersley number also affecting the Peclet number, which was factorised out from g. For large values of ρ, the geometric factor is close to zero, but still results in the maximal effective dispersion due to the Peclet number compensating. Therefore, the solute particles are very rarely able to diffuse between streamlines over a single period, decreasing the effective dispersion. However, if they are able to do so, the advective transport rate is significantly more effective, causing a larger spread in the horizontal position between the particles. A large value of the Womersley number always results in the effective dispersion being equal to the molecular one due to the flow being negligible.

With the zeroth-order solution verified and analysed, we continue our investigation with the addition of a varying boundary.

4.2.5 Contributing terms to higher-order effective dispersion

The solutions of the higher-order Brenner equations will be used to find the effective dispersion, using equation (4.12). Although the higher-order Brenner fields become increasingly complicated, they are slightly simplified when calculating the effective diffusion coefficient, as many terms vanish upon taking the spatial average over the unit cell. To simplify the final expression, we perform the spatial average over η before knowing the exact form of the Brenner field, such that we need only calculate the terms that end up contributing to our final result. To do so, we write the n'th order solution of the Brenner field as

$$B^{(n)} = B_+^{(n)}(\xi, t)\sin(\kappa\eta) + B_-^{(n)}(\xi, t)\cos(\kappa\eta) + B_0^{(n)}(\xi, t). \tag{4.41}$$

The overtones we have observed for the ground wavelength in η will occur at higher orders in ϵ, but these will not contribute due to vanishing upon taking the spatial average for ϵ^2. The term linear in B from equation (4.33), is given to second-order by

$$\nabla_x B = \nabla_x^{(0)} B^{(0)} + \epsilon\left(\nabla_x^{(0)} B^{(1)} + \nabla_x^{(1)} B^{(0)}\right) + \epsilon^2\left(\nabla_x^{(2)} B^{(0)} + \nabla_x^{(1)} B^{(1)} + \nabla_x^{(0)} B^{(2)}\right). \tag{4.42}$$

Employing the decomposition scheme from above (4.41), and taking the horizontal unit cell average, the end contribution simplifies greatly

$$-\langle 2\nabla_x B\rangle = \epsilon^2\kappa\langle(1+\xi\partial_\xi)\,B_-^{(1)}\rangle_\perp, \tag{4.43}$$

where $\perp$ represents the vertical average. The term proportional to the Brenner field squared in equation (4.41) becomes more complicated

$$\begin{aligned}(\nabla B)^2 = \left(\nabla^{(0)}B^{(0)}\right)^2 &+\epsilon^2\left(\nabla^{(0)}B^{(1)}+\nabla^{(1)}B^{(0)}\right)^2\\ &+2\epsilon^2\left(\nabla^{(2)}B^{(0)}+\nabla^{(1)}B^{(1)}+\nabla^{(0)}B^{(2)}\right)\cdot\left(\nabla^{(0)}B^{(0)}\right).\end{aligned} \tag{4.44}$$

Following the decomposition from earlier (4.41), and calculating the spatial average in η, we find

$$\begin{aligned}\left\langle(\nabla B)^2\right\rangle = \left\langle\left(\nabla^{(0)}B^{(0)}\right)^2\right\rangle + \epsilon^2\Bigg\langle &\frac{1}{2}\left(1+\kappa^2\xi^2\right)\left(\partial_\xi B^{(0)}\right)^2 - \partial_\xi B^{(0)}\left[\partial_\xi+\kappa^2\xi\right]B_+^{(1)}\\ &+2\partial_\xi B^{(0)}\partial_\xi B_0^{(2)}+\frac{1}{2}\left[\left(\partial_\xi B_+^{(1)}\right)^2+\kappa^2 B_+^{(1)^2}+\left(\partial_\xi B_-^{(1)}\right)^2+\kappa^2 B_-^{(1)^2}\right]\Bigg\rangle_\perp.\end{aligned} \tag{4.45}$$

Combining the two contributions, we find that the effective diffusion coefficient is calculated from taking the vertical average of

$$\begin{aligned}D_\parallel = D_\parallel^{(0)} + D_m\epsilon^2\Bigg\langle &\kappa\left(1+\xi\partial_\xi\right)B_-^{(1)}+\frac{1}{2}\left[\left(\partial_\xi B_+^{(1)}\right)^2+\kappa^2 B_+^{(1)^2}+\left(\partial_\xi B_-^{(1)}\right)^2+\kappa^2 B_-^{(1)^2}\right]\\ &+\partial_\xi B^{(0)}\left[2\partial_\xi B_0^{(2)}-\partial_\xi B_+^{(1)}-\kappa\xi^2 B_+^{(1)}\right]+\frac{1}{2}\left(1+\kappa^2\xi^2\right)\left(\partial_\xi B^{(0)}\right)^2\Bigg\rangle_\perp.\end{aligned} \tag{4.46}$$

The important detail to notice from this expression is that it is only the η-independent part of the second-order Brenner field which contributes to the effective dispersion. Thus, the second-order calculation of the Brenner field is greatly simplified.

4.2.6 First-order Brenner field

With the known velocity field, and the zeroth order Brenner field, the first-order Brenner field is found by solving equation (4.13). The known right hand side can be decomposed into the different horizontal phases, with different frequencies

$$\begin{aligned}\mathrm{RHS} = &\cos\kappa\eta\left(\kappa\xi u_x^{(0)}\partial_\xi B^{*(0)}+\kappa\xi u_x^{*(0)}B^{(0)}-\frac{u_y^{(1)}}{D_m}\partial_\xi B^{*(0)}-\frac{u_y^{*(1)}}{D_m}\partial_\xi B^{*(0)}\right)\\ &+\sin\kappa\eta\left(\kappa^2\xi\partial_\xi B^{(0)}-2\partial_\xi^2 B^{(0)}+\frac{u_x^{(1)}}{D_m}\right)e^{i\omega t}+\text{c.c}\\ &+\cos\kappa\eta\left(\kappa\xi u_x^{(0)}\partial_\xi B^{(0)}-\frac{u_y^{(1)}}{D_m}\partial_\xi B^{(0)}\right)e^{2i\omega t}+\text{c.c.}\end{aligned} \tag{4.47}$$

To arrive at this form, we have factorised the η and t dependence out of the velocity and Brenner fields, such that they are only dependent on ξ. The horizontal phases of $\cos(\kappa\eta)$ have even temporal frequency, while the horizontal phases of $\sin(\kappa\eta)$ have an odd temporal frequency. When investigating the left-hand side of equation (4.13), we see a new term, $\boldsymbol{u}\cdot\nabla B$, compared to the zeroth-order equation. This additional term adds an *interaction* between the first-order solutions of different frequencies. This is made clear by writing our solution on the form

$$B^{(1)} = \sum_{n=-\infty}^{\infty} e^{i\omega n t}\left(S_n(\xi)\sin\kappa\eta + C_n(\xi)\cos\kappa\eta\right). \tag{4.48}$$

Plugging this into the left hand side of equation (4.13), we end up with

$$\text{LHS} = \cos\kappa\eta\left(\rho_n^2 C_n - \partial_\xi^2 C_n + \frac{\kappa u_x^{(0)}}{D_m}S_{n-1} + \frac{\kappa u_x^{*(0)}}{D_m}S_{n+1}\right)e^{i\omega n t} \tag{4.49}$$

$$+\sin\kappa\eta\left(\rho_n^2 S_n - \partial_\xi^2 S_n - \frac{\kappa u_x^{(0)}}{D_m}C_{n-1} - \frac{\kappa u_x^{*(0)}}{D_m}C_{n+1}\right)e^{i\omega n t}, \tag{4.50}$$

where we have defined $\rho_n^2 = n\rho^2 + \kappa^2$. We see that the solution proportional to $\cos(\kappa\eta)$, with a frequency n, will depend on the solution proportional to $\sin(\kappa\eta)$ with frequency $n\pm1$. Likewise the soution proportional to S_n will interact with $C_{n\pm1}$. The full solution consists of two completely independent infintely large sets. One has even temporal frequencies proportional to $\cos(\kappa\eta)$, and odd temporal frequencies proportional to $\sin(\kappa\eta)$. The other solution will be the opposite; even temporal frequencies proportional to $\sin(\kappa\eta)$, and odd temporal frequencies proportional to $\cos(\kappa\eta)$. The solution has gone from one of a single frequency, to infinitely many frequencies, where we have to solve two independent infinite sets of ordinary differential equations. Additionally, the solution must satisfy the boundary condition

$$\hat{\mathbf{n}}_\pm^{(0)}\cdot\boldsymbol{\nabla}^{(0)}B^{(1)} = \partial_\xi B^{(1)} = \mp\kappa\cos\kappa\eta \qquad \text{on} \quad \partial\Omega. \tag{4.51}$$

Which in our decomposition can be written as

$$\partial_\xi C_0\big|_{\xi=\pm1} = \mp\kappa, \tag{4.52}$$

while all other terms must have a zero derivative at the boundary. By investigating the source terms (4.47), we see that they only contribute to one of the independent solutions, as the horizontal phase of $\cos(\kappa\eta)$ in the source term have even temporal frequency, while the horizontal phases of $\sin(\kappa\eta)$ have an odd temporal frequency. In addition, the boundary condition (4.52) will only influence the same set of solutions. Without any source terms or boundary conditions, we must conclude that the connected solutions of S_0, $C_{\pm1}$, $S_{\pm2}$ and so on, must all be identically equal to zero. We therefore only have to solve one infinite set of ordinary differential equations, C_0, $S_{\pm1}$, $C_{\pm2}$, …, instead of two. An illustration of this coupling is displayed in figure 4.18 on the following page. While this is a simplification, as we now require only half the number of solutions, we still need infinitely many.

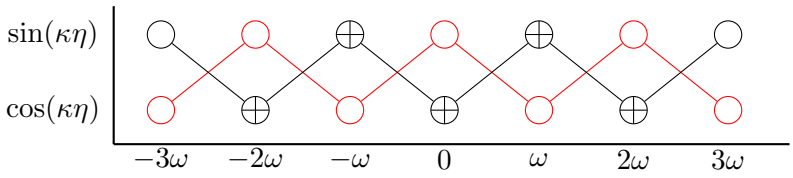

Figure 4.18: An illustration of the coupling between different terms in the analytic first-order Brenner field is displayed, where the horizontal axis gives the different frequencies, while the vertical axis gives the spatial phase, representing S_n and C_n. The black and red terms are completely independent of one another. The source terms and boundary conditions act on the terms with crosses and therefore only contribute to the black terms. Without any source terms or boundary conditions, we conclude that the red terms are zero. The black terms without crosses will still be non-zero due to their coupling.

4.2.7 Second-order Brenner field

We have the same left-hand side for the second-order Brenner field as for the first-order, but with a more complicated source term (4.15). Luckily, it is only the η independent part of $B^{(2)}$ that contributes to the effective dispersion coefficient, as seen in equation (4.46). Thus, we will guess on a solution independent of η, on the form

$$B^{(2)} = \sum_{n=-\infty}^{\infty} e^{i\omega n t} \beta_n(\xi). \tag{4.53}$$

This also simplifies the source term Q, as it is only the η independent terms that will contribute to the right hand side. This rewrite allows the equation (4.15) to be written as

$$\frac{\mathrm{d}^2 \beta_n}{\mathrm{d}\xi^2} = n\rho^2 \, \beta_n - Q_n, \tag{4.54}$$

which is a great simplification compared to what we had for $B^{(1)}$, as coupling between frequencies of the unknown solutions no longer appears, such that each n can be solved separately. The loss of coupling at second-order is due to the coupling term being proportional to the horizontal derivative ∂_η. This will create a coupling between the $\cos(\kappa\eta)$ and $\sin(\kappa\eta)$ terms, never affecting the η-independent parts. Performing a calculation on the source term, we find that many terms cancel, yielding

$$\begin{aligned} Q = &\frac{1}{2}\kappa^2 \xi \partial_\xi B^{(0)} + \frac{1}{2}\left(3 + \kappa^2\xi^2\right)\partial_\xi^2 B^{(0)} - \frac{1}{2}\kappa^2 \xi \partial_\xi B_+^{(1)} - \partial_\xi^2 B_+^{(1)} \\ &+ \frac{1}{2D_m}\left(u_x^{(0)} \kappa \xi \partial_\xi B_-^{(1)} + u_x^{(1)} \kappa B_-^{(1)} - u_y^{(1)} \partial_\xi B_-\right) + \frac{1}{D_m}\left(u_{x,0}^{(2)} - \langle u_{x,0}^{(2)} \rangle - \langle u_x^{(1)} \rangle^{(1)}\right), \end{aligned} \tag{4.55}$$

where the decomposition was applied (4.41). The boundary condition for the second-order is given by

$$\partial_\xi \beta_n = 0 \qquad \forall \; n. \tag{4.56}$$

While the second-order Brenner field is simpler to solve than its first-order counterpart, it relies on the analytical expressions of the first-order solution. Hence, the difficulty of finding an analytical expression is to solve the first-order equations, not the second-order.

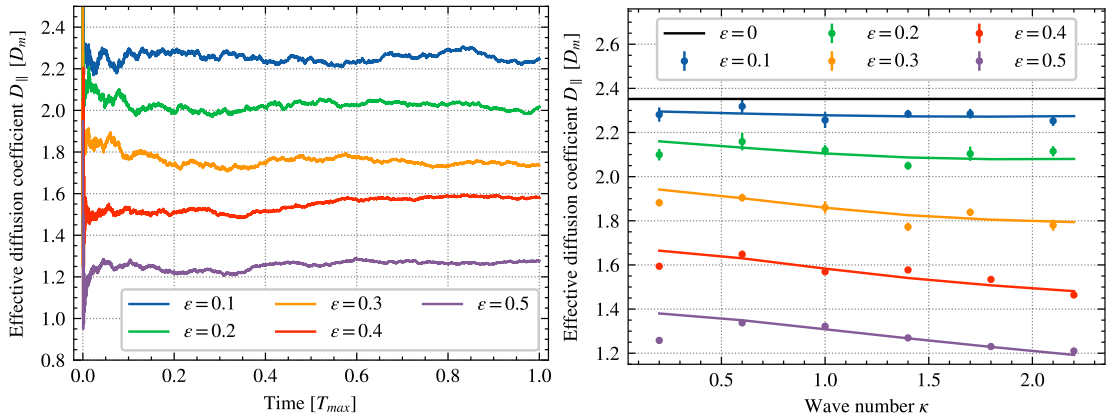

Figure 4.19: The effective diffusion coefficient is calculated from the average of the variance found from RW simulations (left), resulting in the dots in the right figure. This is compared with the predicted dispersion from solving the time-dependent Brenner equation (lines), and is seen to be in good agreement. A systematic disagreement is seen for $\kappa = 0.2$, which is believed to be due to the size of the unit cell increasing such that a longer simulation time is necessary to reach convergence. When varying ϵ and κ, the other parameters are fixed to $\omega = 2\pi/3$, $\nu = 1.2$, $D = 0.1$ and $F_0 = 10$, in the left figure κ is held constant at 1.4.

4.2.8 Numerical solutions of Brenner's equations

To find the effective diffusion coefficient beyond the regime where perturbative solutions are admissible, the time-dependent Brenner equation is solved numerically with the finite element method. This is done to validate the perturbative approach and extend our analysis to the regime where our perturbative approach is no longer valid. To validate the implementation of the FEM and the time-dependent Brenner equation with a varying boundary, we compare the numerical solution of this equation with RW simulations. The two methods are seen to agree for different combinations of boundary amplitude and wavenumber shown in figure 4.19. A systematic disagreement is seen for the shortest wavenumber, which is believed to be due to the size of the unit cell requiring a longer simulation time to reach convergence in the RW simulation.

With the Brenner solver verified, we extend our investigation to other parameters. In figure 4.20 on the following page, the effective diffusion coefficient is displayed as a function of the geometry parameters. With increasing wavenumber and boundary amplitude, the effective dispersion is found to decrease. The decrease is not only due to the Peclet number decreasing with larger geometrical variations, as its value relative to the Taylor-Aris result for the same Peclet number is also reduced. For the same velocity field, a more interesting behaviour is seen by increasing the molecular diffusion, resulting in $|\rho| = 1.45$ and $\mathcal{O}(\mathrm{Pe}) = 1$, displayed in figure 4.21 on the next page, where a local maximum is observed when varying the wavenumber. The maximum is both in the measured dispersion and relative to the Taylor-Aris result. The combination of frequency and wavenumber that interact to maximise the dispersion will be referred to as resonance. For the combination of parameters considered in the figure, the effective dispersion is maximised at around $\kappa = 1.0$.

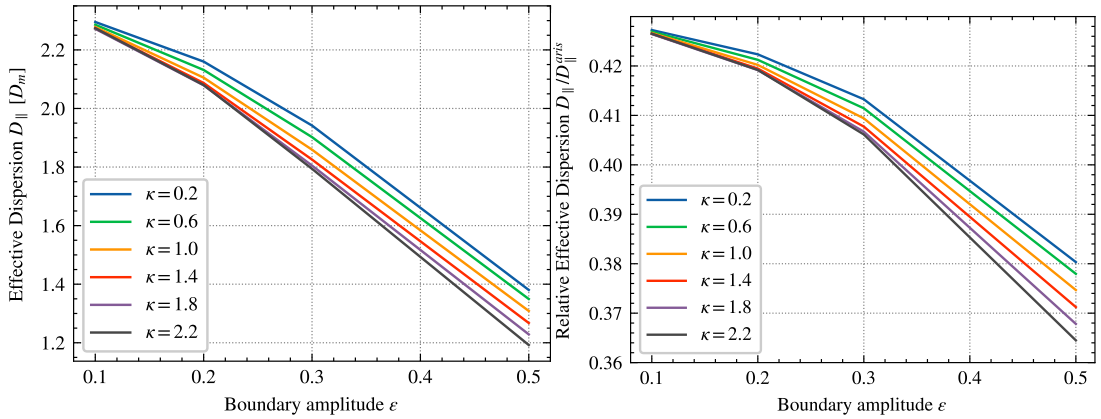

Figure 4.20: The absolute and relative effective dispersion is found to decrease when varying both the boundary amplitude and wavenumber for $|\rho| = 4.6$ and $\mathcal{O}(\mathrm{Pe}) = 10$. The dispersion is less than half as efficient as in the Taylor-Aris result with the same Peclet number. When varying ϵ and κ, the other parameters are fixed to $\omega = 2\pi/3$, $\nu = 1.2$, and $F_0 = 10$, with $D = 0.1$.

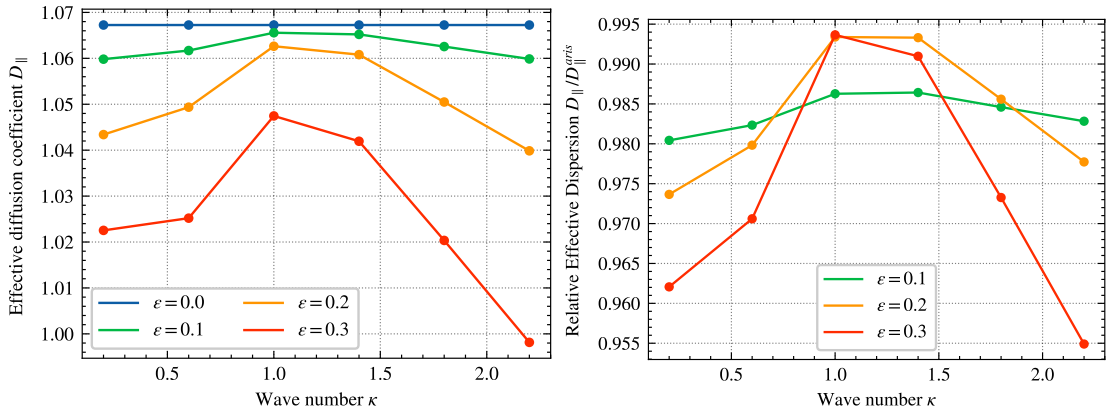

Figure 4.21: With the diffusive Womersley number, $|\rho| = 1.45$, similar to the wavenumber of the geometry, a resonance behaviour is observed. Both the shape of the resonance peak and its position seems to be independent of the boundary amplitude. While a local maximum is reached, the effective dispersion is lower than the zeroth order dispersion and slightly smaller than the Taylor-Aris result. When varying ϵ and κ, the other parameters are fixed to $\omega = 2\pi/3$, $\nu = 1.2$, $D = 1.0$ and $F_0 = 10$.

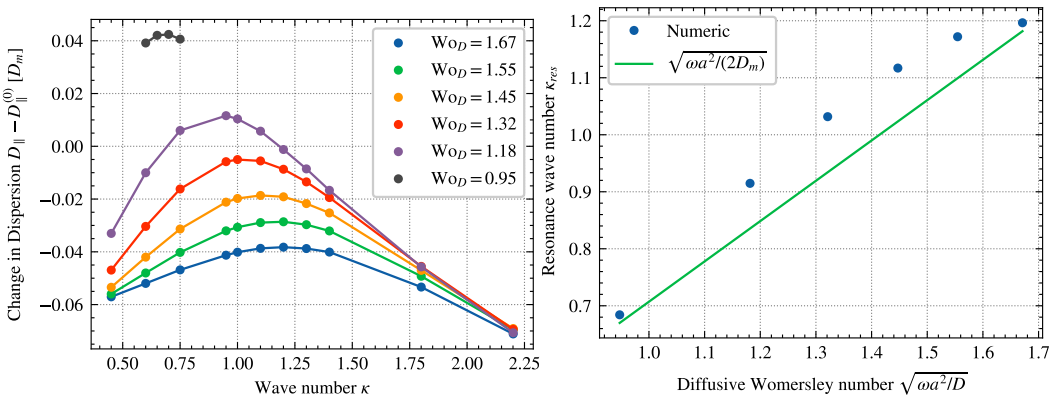

Figure 4.22: The resonance wavenumber is found to increase with the diffusive Womersley number, producing a larger effective dispersion than its flat boundary counterpart for small values of ρ. The position found from the numerical data points (left) is tested versus the real value of ρ in the right figure. While the two curves are not exactly matching, their behaviour is similar, with a maximum relative difference of approximately 10%. The analytically predicted resonance wavelength seems to give an approximately correct value, but it is unknown if this relationship continues to hold at even larger and smaller wavenumbers, and for other external forces and viscosities. While ω and κ are varied, the other parameters are fixed to $\epsilon = 0.3$, $D = 1.0$, $\nu = 1.2$, $F_0 = 10$.

The resonance wavelength changes for different values of the diffusive Womersley number, as displayed in figure 4.22. With longer diffusive transport over a period, the resonance wavelength increases and can even result in a larger effective dispersion compared to a flat boundary. The resonance wavenumber scales approximately as the real part of ρ, as displayed to the right of the same figure. The range of parameters scanned in this figure is relatively narrow, as the numerical investigation is expensive to run. From figure 4.22 and 4.23, we can conclude that the position of the resonance wavelength depends both on the frequency ω, and the molecular diffusivity D_m.

For figure 4.20 and 4.21, the velocity field was the same, while the molecular diffusivity is varied. To find the velocity field, the inertial term was neglected from the Navier–Stokes equations in the numerical solver. This assumption is verified in figure 4.23 on the next page, where the effective dispersion for this flow field, with the addition of the inertial term, is found to have minimal effect on the dispersion. The relative change by including the non-linear term is found to vary less than one per cent for a Reynolds number around one. Importantly, the resonance behaviour is not an artefact of ignoring the non-linear term in the Navier–Stokes equations. Although the velocity field in figure 4.22 is different, it is calculated at similar values of the Reynolds number, and the assumption should therefore hold. In addition to increasing with larger Reynolds numbers, the difference is expected to increase with steeper boundary gradients.

By varying the external force, the Reynolds and Peclet number is increased for a fixed value of both γ and ρ. Due to inertia no longer being negligible, the non-linear term in the NSE is included. The effective dispersion is found to be somewhat larger than the Taylor-Aris result for large Peclet numbers, displayed in figure 4.24 on the following

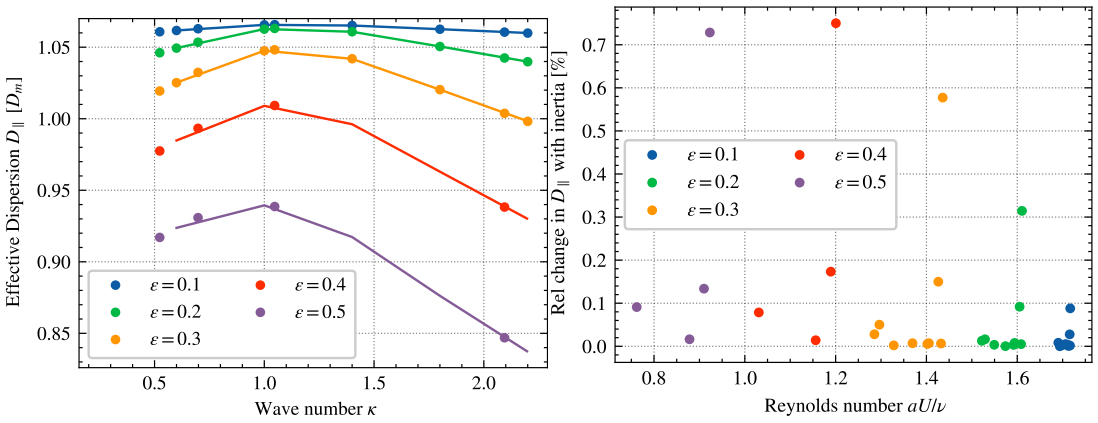

Figure 4.23: The validity of ignoring the non-linear term in the Navier–Stokes equations is verified by the small change in the effective dispersion with the term included (lines), compared to when it is ignored (dots). The difference in the left figure is used to calculate the relative change displayed in the right figure. For a Reynolds number of up to 1.7, the approximation appears valid for the geometries investigated here. When varying ϵ and κ, the other parameters are fixed to $\omega = 2\pi/3$, $\nu = 1.2$, $D = 1.0$ and $F_0 = 10$.

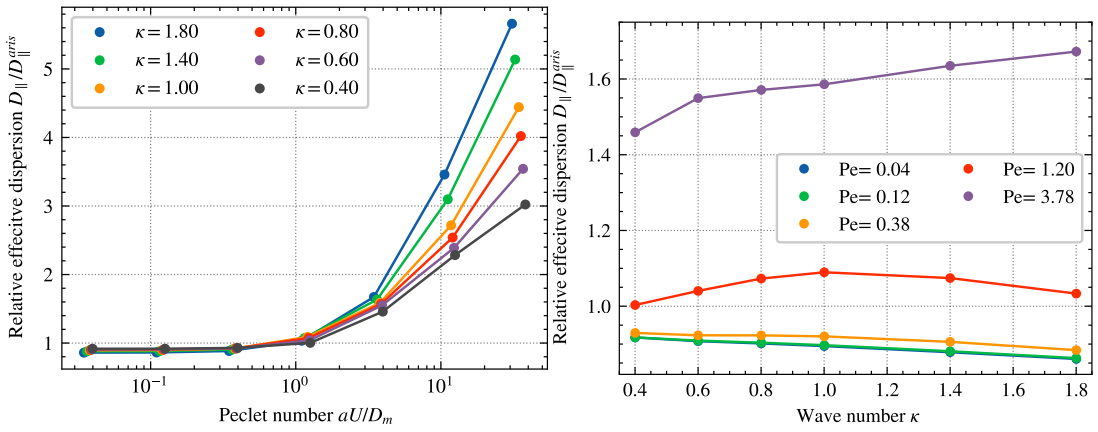

Figure 4.24: The effective dispersion is found to be larger than the Taylor-Aris result for large Peclet and Reynolds numbers. The wavenumber transitions from decreasing to increasing the effective dispersion, with larger Peclet numbers. For an intermediate value of the Peclet number close to one, the resonance behaviour is observed. While varying F_0 and κ, the other parameters are fixed to $\omega = 2\pi/3$, $\nu = 2.25$, $D = 1.0$ and $\epsilon = 0.4$. The Peclet number given in the right legend is the mean value for all wavenumbers.

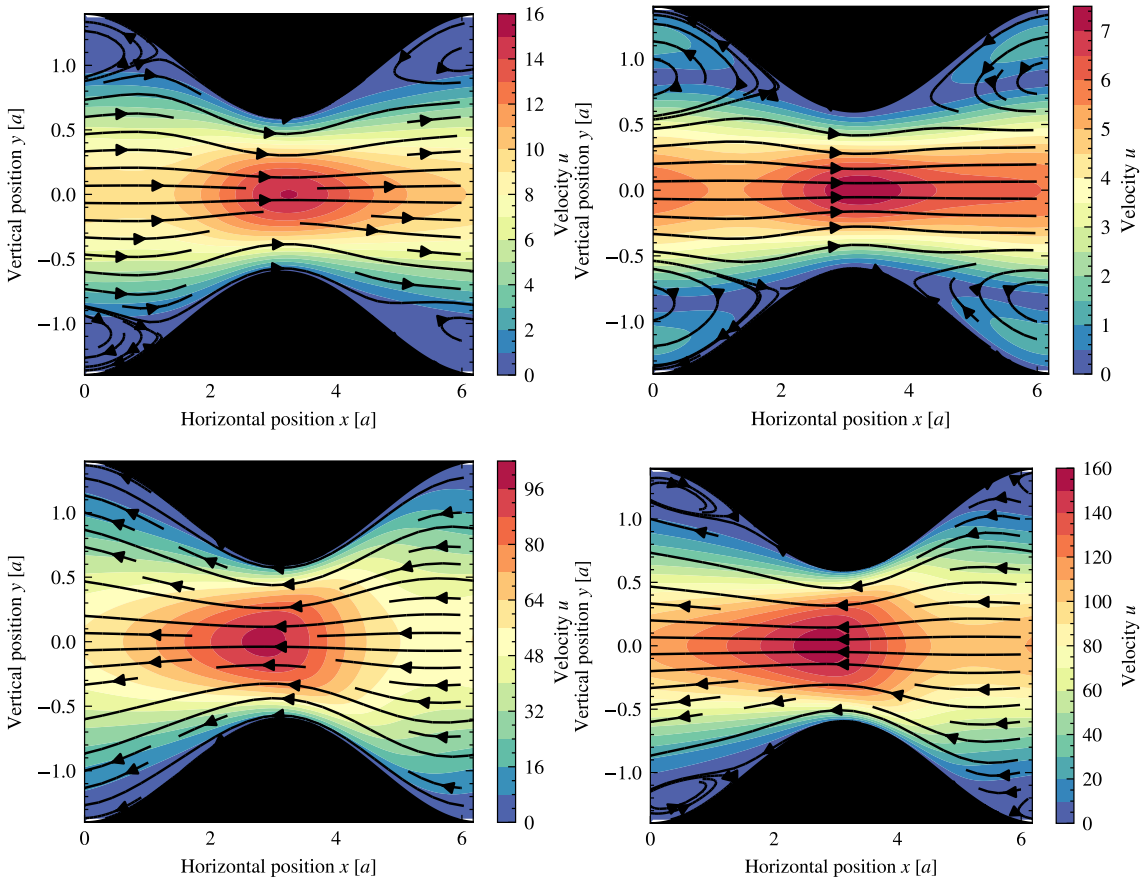

Figure 4.25: Recirculation zones are seen to appear in the velocity field for a Reynolds number of 25, with $\kappa = 1$ and $\epsilon = 0.4$, when including the non-linear term in the Navier–Stokes equations. Recirculation zones appear when the flow is developing, and persists until it reversed. The velocity field is found for $\omega = 2\pi/3$ and $\nu = 2.25$, note the different scales of the axis.

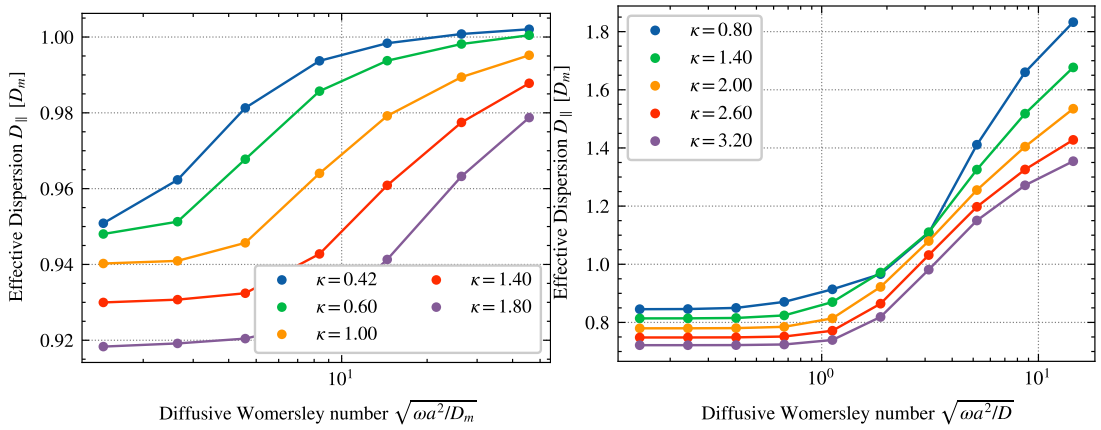

Figure 4.26: The effective dispersion appears to reach a saturation value for large diffusive Womersley numbers, where the Peclet number is around 10 (left), but does not reach the same saturation value when the Peclet number is around 100 (right). The behaviour with respect to the wavenumber is the same in both figures. The wavenumber and molecular diffusion coefficient is varied, while keeping the other parameters fixed: $\omega = 2\pi/3$, with $F_0 = 1$ and $\nu = 2.25$ in the left figure, and $F_0 = 10$ and $\nu = 1.2$ in the right figure, to create a larger Peclet number.

page. In the transition from small to large Peclet numbers, the effective dispersion changes from decreasing to increasing with the wavenumber. At the intermediate point of a Peclet number around one, the resonance behaviour is observed and displayed to the right in the same figure. When varying the Peclet number, the Reynolds number is implicitly changed and is for this dataset half the value of the Peclet number. The corresponding velocity field is displayed in figure 4.25 on the previous page, where recirculation zones appear. The recirculation zones appear while the flow is developing and persists until the velocity is reversed.

The molecular diffusion coefficient can be reduced to increase the Peclet number at a fixed value of the Reynolds number, increasing the diffusive Womersley number. How this affects the dispersion is displayed in figure 4.26, where, to the left in the figure, a saturation value appears in the limit of a large diffusive Womersley number. In this limit, the Peclet number is of order 10, but due to the diffusing particles slowly changing streamlines, their net advection over a period is close to the average velocity of zero. In this limit, the effective dispersion seems to approach a value slightly larger than the molecular value, likely due to the slight differences in advection between particles. To the right in the same figure, the Peclet number is of order 100, and the saturation point is never reached. The saturation value might still exist, just that it has moved to larger values of the diffusive Womersley number. The change in dispersion between the two graphs is around a factor of two, though the Peclet numbers differ by over a factor of 10. The diffusive Womersley number reduces the effectiveness of the Peclet number by limiting the advected distance per period.

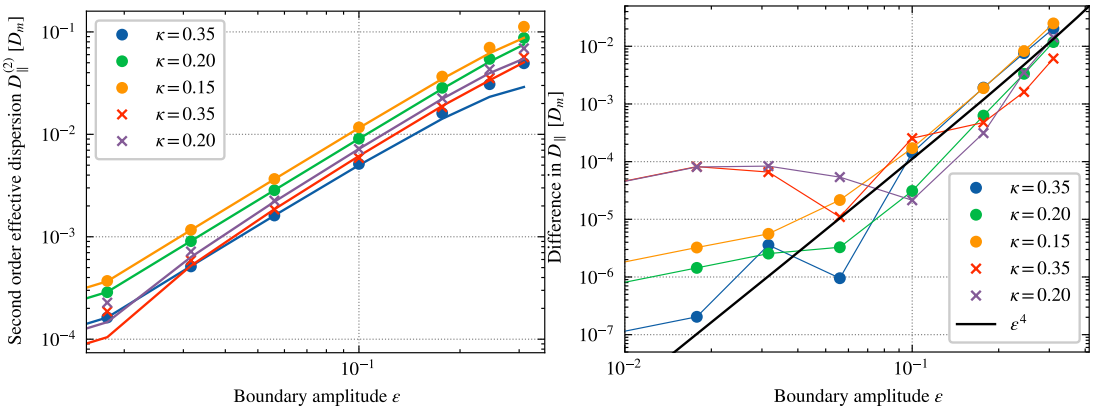

Figure 4.27: The numerical solution of the analytic equations are in good agreement with the full numerical solution. The difference follows the expected order of magnitude of ϵ^4. To compare the effect of the boundary, the zeroth order contribution to the effective dispersion has been subtracted from the expressions. The non-linear term is neglected from the Navier–Stokes equations, and the parameters are set to $\omega = 2\pi/6$, $\gamma = 0.45$, and $F_0 = 50$, with the circles for $\rho = 0.20$ and crosses for $\rho = 0.51$.

4.2.9 Semi-analytic solutions for the effective diffusion coefficient

Solving the set of equations for the first (4.50) and second (4.54) order Brenner field analytically proved to be a challenge. In the analytical analysis of the first and second-order equations for the Brenner field, the three-dimensional partial differential equations become ordinary differential equations, making them much easier to solve numerically. Using the procedure given as a simple example of the finite-element method in section 3.2.1 on page 32, the first and second-order Brenner fields are solved numerically. While not yielding an analytical result, the numerical solver is less numerically expensive than solving the complete partial differential equation, at the cost of being a perturbed solution. The Brenner field is calculated using a frequency spectrum from -16ω to 16ω, beyond which the solution is truncated due to the amplitude being vanishingly small.

The solution for the effective diffusion coefficient, using the non-perturbed numerical method and semi-analytical method, are compared against each other in figure 4.27, with the difference displayed to the right. The semi-analytic solution agrees well with the direct numerical solution of Brenner's equation and follows the expected error of ϵ^4. A deviation is seen for small ϵ due to the spatial and temporal accuracy of the complete numerical solver and performing numerical integrals.

With the semi-analytical approach verified, it is used to effectively scan the parameter space to understand the resonance wavelength. The resonance behaviour previously observed has occurred for Reynolds number of order 1. To be certain that the semi-analytic approach produces the correct result, the parameter space is scanned for a large value of the kinematic viscosity, producing a small Reynolds number. In this regime, the assumption of ignoring the non-linear term in the Navier–Stokes equations are valid. The resonance wavelength is measured for various frequencies, diffusion coefficients and external forces.

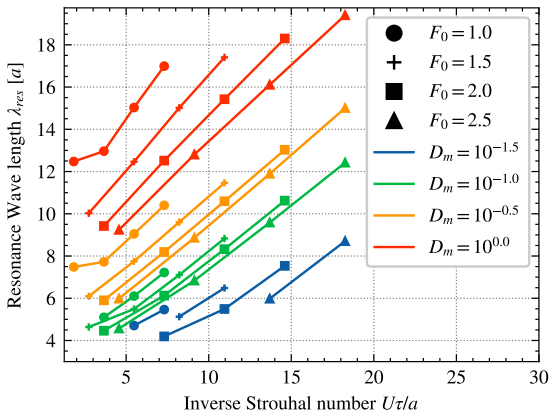

Figure 4.28: The resonance wavelength shows a linear relationship with the inverse Strouhal number for a variety of external forces and diffusion coefficients. A larger value of the diffusion coefficient is found to increase the resonance wavelength. The second-order effective diffusion coefficient is used to calculate the value of κ resulting in the maximal dispersion, when varying D_m, F_0, ω and κ, with $\nu = 1000$.

The resonance wavelength is displayed in figure 4.28, where a linear relationship is observed with relation to the inverse Strouhal number. Since the average velocity U depends on both the boundary amplitude and wavenumber, the zeroth-order average velocity is used to approximate the average velocity, despite slightly overestimating the value. The average advected distance over a period is generally larger than the resonance wavelength. Increasing the molecular diffusion coefficient results in a positive shift of the resonance wavelength.

4.2.10 Discussion

Verification of time-dependent Brenner theory

From the comparison with RW simulations displayed in figure 4.16 and 4.19, the generalisation of Brenner's theory to time-dependent flow is believed to be correct, both with a flat and varying boundary amplitude. The generalised theory, derived in appendix A, represents a new method for calculating the dispersion tensor in periodic environments, in any dimension, of incompressible time-dependent flow. As the original Brenner theory [41, 42] has proven to be a solid basis for calculating the dispersion tensor [25, 66, 92], the generalisation of the theory will extend its applicability to more systems. Possible areas of applicability are the effective dispersion in multi-phase or turbulent flow, which are generally time-dependent.

Velocity field

In figure 4.15 on page 61 the velocity field is displayed for four points in time at a specific combination of parameters. When the flow is fully developed, it takes a form similar to that of Poiseuille flow, with an increased velocity in the pore throats and a decrease in the

valleys. When the average velocity is close to zero, more interesting behaviour is observed. A small recirculation zone appears in the deepest valleys close to the boundary, which then slowly drifts upwards to the centre of the channel before it disappears once the flow is fully developed. Whereas the velocity profile has some interesting aspects at this point in time, the slight velocity differences in the unit cell are unlikely to significantly impact the effective dispersion. For smaller values of the Womersley number, the velocity profile is Poiseuille-like at all points in time, and no interesting behaviour is seen.

The analytic velocity field neglects the non-linear term in the Navier–Stokes equations. Based on figure 4.23 on page 72, the assumption appears to hold for at least Reynolds numbers of order one. This assumption will decrease in validity for larger values of the Reynolds number and steeper boundary gradients. Further studies on this system should systematically investigate its effect at larger values of the Reynolds number.

For some applications, e.g. transport of solutes in blood flow, there is an overall preferred direction due to a constant body force, in addition to the oscillating one investigated here. When the flow has a preferred direction, the effect of an oscillating flow and a varying boundary might be completely different, as the channel is no longer vertically symmetric. A natural question for further investigations is whether, and to which extent, the resonance behaviour persists under such conditions. Additionally, a constant body force would result in additional fluid share, likely resulting in a larger effective diffusion coefficient [43]. The generalised Brenner theory developed here would act as an excellent theoretical framework for this investigation.

Zeroth order diffusion coefficient

Analytic expressions for the effective dispersion at flat boundaries with an oscillating flow are already well established in the literature [43]. In this work, this geometry was investigated to verify the generalised Brenner theory for flat boundaries and produce the zeroth-order Brenner field necessary to continue to higher orders. While this system has been studied previously, some interesting behaviour should be discussed.

There are two relevant time scales for diffusion in our system, the Womersley number and the diffusive Womersley number. These parameters appear naturally in our equations and contain a complex scaling of $\sqrt{i}$, quantifying a phase difference. For the Womersley number, the phase difference is between the external force F_0 and the fluid response in terms of velocity. The parameter γ only appears with even powers, therefore contributing a phase difference of 90°. For large values of γ, therefore, the fluid reaches its maximum velocity at the point when the external force becomes zero. For small values, on the other hand, the fluid has no phase difference with the force and responds immediately to the external changes. The equation containing the diffusive Womersley number (4.10) does not depend on the body force acting on the fluid directly, only indirectly through the velocity field $\boldsymbol{u}$. Thus, ρ measures the phase difference between the fluid oscillations and the resulting solute dispersion. In the limit of large values of ρ, the effective dispersion has a phase difference of 90° compared to the fluid velocity. Hence, if the particles are not able to diffuse between streamlines over a single period, their maximal displacement will be 90° after the maxima of the velocity field is reached. When the particles are able

to cross the channel height multiple times in a single period, the phase difference with the flow is zero, meaning the maximal displacement is reached when the average velocity is at its maximum. This is consistent with equation (4.36), where the dispersion follows the oscillating force in the limit of small values of both ρ and γ. Therefore, the frequency doubling of the dispersion is due to the variance increasing the most when the magnitude of the velocity field is large, independent of direction, resulting in two maxima for each period. The diffusive Womersley number proves to be an essential characteristic of the dispersion behaviour, in agreement with experimental measurements on the same system [49]. It characterises the saturation value of the geometric factor g, gives the transition interval from zero to non-zero effective dispersion, and governs the phase difference between the flow and the dispersion.

In figure 4.17 on page 64, the geometric factor and the effective diffusion coefficient is displayed as a function of both the time scales, γ and ρ. A surprising feature of this figure is the opposite dependency of ρ for g and $D_{\parallel}$. The diffusion length over a period is short compared to the channel height for large values of ρ, such that the particles are advected along a single oscillating streamline each period. For the flow investigated here, the average velocity for any streamline over a period is zero, such that the advected distances for the particles are zero. Therefore, one would expect the effective diffusion coefficient to be equal to the molecular diffusion coefficient. This would be correct if the Peclet number is held constant when varying ρ. In the figure, advective transport dominates when the diffusive Womersley number is large. This results in the small diffusive distance over a period resulting in a larger horizontal displacement. There are two competing effects when varying the molecular diffusion coefficient, one increasing $D_{\parallel}$ and one decreasing it. When comparing the numerical values of the effective dispersion in figure 4.17 on page 64, they are drastically smaller than for Poiseuille flow. For example is the smallest value of D_m used in this figure 10^{-6}, which would typically give an effective diffusion coefficient on the order of 10^{10} without the oscillating force. Therefore, the two competing effects are in a very close fight, as their product ends up being so close to 1. This behaviour extends to varying boundaries, as seen in figure 4.26 on page 74, where decreasing the diffusion coefficient results in a saturation value for the effective dispersion for a Peclet number of 10, but not for a Peclet number of 100. There are two competing effects when decreasing the diffusivity, an increase in Peclet number and an increase in the diffusive Womersley number. A dimensionless number to maximise the dispersion might therefore be the Peclet number over the diffusive Womersley number, as the Peclet number should be maximised while minimising the Womersley number

$$\delta = \frac{U}{\sqrt{\omega D_m}}. \tag{4.57}$$

This dimensionless number gives the advection speed relative to the characteristic diffusion speed over a period. The dimensionless number might better capture the Peclet number's role for oscillating flows.

Effective diffusion coefficient with varying boundary

In figure 4.20 the effective dispersion is found to decrease with increasing boundary amplitude and wavenumber. A similar decrease is found in the same geometry with stationary flow, but only for Peclet numbers larger than 10 at large boundary amplitudes and long wavelengths [25]. Their behaviour is explained by the fact that for large Peclet numbers, the varying boundary makes vertical diffusive transport across streamlines more efficient, and in the long wavelength regime the additional shear is not enough to compensate. By reducing the wavelength in this geometry, the amount of shear increases, and eventually, the change in effective dispersion becomes positive. The decrease measured here occurs for a Peclet number of order 10, and decreases both for short and long wavelengths, contrary to what is previously observed [25]. By displaying the change in effective dispersion relative to the Taylor-Aris result, we can verify that the decrease is not just due to the average velocity of the fluid decreasing with more prominent boundaries, but is a consequence of interactions between the solute and the flow in the presence of a varying boundary. The data suggests that the effective dispersion for oscillating flows with varying boundaries is more dependent on the contraction of streamlines at the pore throats than the additional fluid shear. The amplitude around the average might increase with shear, as different particles move with greater speeds relative to each other. This increase in variance is reduced when the velocity field is reversing, therefore contributing less to the period average dispersion. Additionally, more particles pass through the pore throat each period at larger values of κ, allowing them to reduce their spread in velocity more efficiently. The tentative explanation explains the observed data, but should be investigated further. One might expect the tentative explanation to be invalid in the limit of large values of the diffusive Womersley number and large Peclet numbers due to the difficulty of switching streamlines suppressing the effective dispersion in this regime. In light of the data displayed in figure 4.26 on page 74, where larger values of κ result in smaller values of the effective dispersion, it appears that the tentative explanation holds in this regime as well.

Outside of the resonance phenomena, increasing the wavenumber always decreases the dispersion, except in the large Peclet and Reynolds regime, displayed in figure 4.24 on page 72. In the limit of small Peclet numbers, a large value of κ reduces the effective dispersion as it limits horizontal diffusive transport. In the other limit, a shorter wavelength increases the effective dispersion by a factor of five compared to the Taylor-Aris result. The explanation behind the significant increase is seen in figure 4.25 on page 73, where recirculation zones are found. Recirculation zones act as large regions with no effective transport in either direction, creating a considerable difference in the horizontal velocity between particles stuck in the recirculation zones and those travelling along the high-speed streamlines. This results in a significant increase in the effective dispersion for stationary flow [25, 26], but it is not obvious whether this extends to oscillating flows. For oscillating flows, the net advection of a particle moving along a streamline is zero over an entire period, which is the same net advection it would experience in a recirculation zone. Still, based on the significant increase in dispersion found in figure 4.24, it appears as if recirculation zones add a large positive contribution to the effective dispersion, even for oscillating flows. In fact, the relative increase is similar to what is found for stationary flows in the same

geometry [26]. With increasing wavenumber, the area of the recirculation zones increases and explains the behaviour observed in figure 4.24.

Resonance

The resonance observed in figure 4.21, 4.22, 4.23, 4.24, and 4.28, has significant consequences on the effective dispersion, and can even result in a larger effective dispersion than for a flat boundary, as seen in figure 4.22. Importantly, the resonance behaviour occurs both for the effective dispersion and its value relative to the Taylor-Aris result. The decrease in the dispersion found for values of the wavenumber larger than the resonance value is not due to a decrease in the Peclet number, but due to interactions between the solute and the flow. Additionally, there are no RZ appearing in either the full numerical or perturbative analytical solution of the velocity field, and there is not a local maximum in terms of shear. This hints at a new mechanism for increasing the effective dispersion, limited to oscillating flows and varying boundaries, which has to the best of our knowledge, not before been observed.

From the above figures, we can conclude that the value of the resonance wavelength decreases with ω and increases with D_m. Therefore, one might expect that the diffusive Womersley number determines the value of the resonance wavelength, which seems plausible based on figure 4.22. The result found in figure 4.28, where an increase in the average velocity results in an increase in the resonance wavenumber, shows that the underlying dynamics are more complicated than first imagined. Still, an explanation for this new method of maximising the dispersion will be made.

A significant difference in the average horizontal velocity between particles over a period should be achieved to maximise the effective dispersion for an oscillating flow. To achieve this, not all particles should pass through the pore throat each period, as this makes the distribution of horizontal advected distance over a period narrower. The same occurs if no particles are able to pass through the pore throats over a period. Therefore, the ideal scenario is that around half of the particles pass through the pore throat each period, while the rest do not pass through. This way, the distribution of advected distance over a period is broad. Therefore, there exists an optimal wavelength of the boundary satisfying the above criteria, where making it longer results in fewer particles passing through the pore throat, and making it shorter results in too many particles passing through the pore throat. For even shorter wavelengths, particles can pass through multiple pore throats over a single period. This argument implies that a longer advected distance over a period will result in a linear increase in the resonance wavelength, consistent with the data in figure 4.28 on page 76. Additionally, the explanation implies that a larger value of the diffusion coefficient must increase the resonance wavelength to limit the number of particles reaching the pore throat, which is again consistent with the figure. Furthermore, it implies that the resonance will only appear when the two transport methods are of a similar order. A small Peclet number will result in the oscillations being unimportant for the transport, and a large Peclet number will make all or none of the particles pass through the pore throat. This tentative explanation of the observed resonance phenomena does explain all the observed effects. Further investigation should be made to falsify or verify the proposed explanation.

A simplified model for the resonance behaviour is a discrete one-dimensional random-walk-like system, where a proportion α of all particles perform a jump to the right each even time step, and a proportion α take a step to the left every odd time step. Performing a jump is in this model equivalent to passing through the pore throat, and two time-steps are equivalent to one period. Calculating the effective dispersion for this updating rule produces an effective diffusion coefficient of $\alpha^2(1-\alpha)^2/2$, capturing that if all particles move in unison, the variance is zero. A local maximum in the effective dispersion is found for the intermediate value $\alpha = 1/2$, corresponding to half of the particles passing through the right pore throat, and half passing through the left, each period. In this model, an optimal choice for the probability of moving to the next *unit cell* is able to produce a local maximum in the effective dispersion, similar to the behaviour argued for in our more complicated system. Our explanation might be verified by performing random walk simulations and counting how many particles pass through the pore throat each period.

From figure 4.28 on page 76, we can conclude that the resonance phenomenon can occur for creeping flow, where the flow is entirely reversible. In addition, it can occur for Schmidt numbers of order 10^3 to 10^4, which are typical values found in nature [30]. It is therefore realisable for a variety of real-world systems. One could speculate as to whether the resonance behaviour is exploited in naturally occurring systems where optimising the dispersion is of importance. If this is the case, it would be an interesting discovery. With the intricate dependence of the resonance wavelength on the diffusion coefficient, frequency and average velocity, it is difficult to make definitive statements about the typical values needed to achieve resonance. However, the resonance wavelength should be of the same order as the inverse Strouhal number, with a Peclet number close to one. From the two, one finds that the resonance wavelength should approximately be $\lambda = D_m\tau/a$, with $U = D_m/a$.

Outlook

The system investigated has a large parameter space, with many dimensionless numbers, which can be reduced to only three independent ones. To limit the parameter space, further investigation should focus on values typical to real-world systems. For example is the Schmidt number commonly around 10^3, meaning that the diffusive Womersley number is usually 31 times larger than the Womersley number. Additionally, one dimensionless variable should be varied while keeping all others fixed to understand the role of different dimensionless numbers better.

Although a tentative explanation of the novel resonance behaviour is provided, many aspects are still unknown. Further research should investigate if the resonance behaviour persists to larger values of the Reynolds numbers. An essential next step is to systematically investigate under what conditions the resonance behaviour produces more efficient dispersion than for a flat boundary, as it might be exploitable for industrial applications, such as microfluidic mixing.

Even though the time-dependent dispersion tensor contains integer overtones of the ground frequency, their amplitudes are close to zero. The interaction coefficient between solutions of $\kappa u_x^{(0)}/D_m$ is seemingly too small for the set of parameters investigated in this study. An extended study for larger boundary amplitudes and shorter wavelengths with

large Peclet numbers would give an interesting insight into the behaviour of the overtones. In theory, an arbitrary smooth periodic function can be written as a discrete Fourier Series, and different behaviour of the dispersion might be achievable.

This thesis limited itself to the asymptotic regime where the initial conditions no longer relevant. Numerical random walk simulations show a behaviour similar to that of chaotic mixing in the transient regime at large Peclet numbers. New insight into the mixing dynamics might be aided by the analytic velocity field derived.

Analytically, the equations proved challenging to solve. Further Taylor approximations, or perhaps boundary layer theory [91], might make the first-order Brenner field solvable, which in turn should make the effective diffusion coefficient possible to find analytically. This can result in a better understanding of the role of different physical parameters, as numerical investigations are expensive to run, with many free parameters. The oscillation amplitude of the dispersion tensor was not investigated in this thesis, as we focused on the period average value. A varying boundary might have interesting effects on the dispersion amplitude, and the generalised Brenner theory will serve as a solid foundation in this investigation.

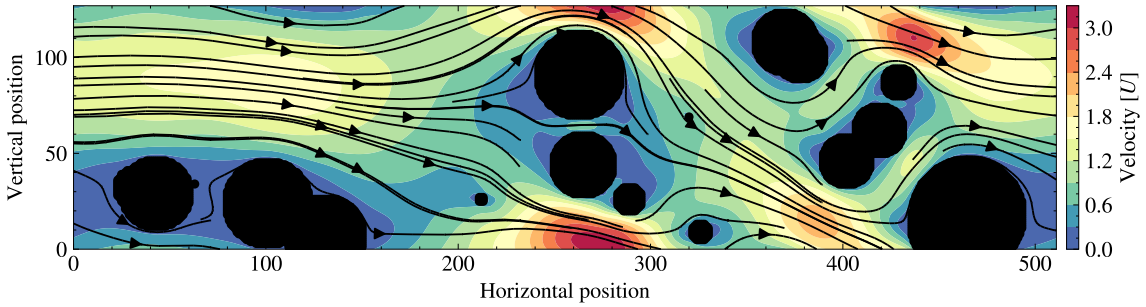

Figure 4.29: An example of a velocity field used in the investigations of this section. With periodic boundary conditions and randomly placed disks, the two-dimensional velocity field is found using the LBM. Placing an injection and receptor point, the LBM is further used to simulate the advection-diffusion equation on the velocity field, to investigate the reciprocal relation.

4.3 Reciprocal relation for reversible flow

Having studied dispersion in two specific geometries, we close this chapter with an investigation of a general relation, which holds true in all geometries. For the numerical study in this section, the lattice-Boltzmann method is used, and the geometry is chosen to be oblong with periodic boundary conditions in both directions. The two-dimensional geometry includes randomly placed disks with a random radius to obtain a non-trivial velocity profile. An example of such a geometry for a 128×512 lattice is displayed in figure 4.29. To study the reciprocal relation, the LBM is used to simulate the advection-diffusion equation, where an arbitrary point is chosen as the injection point, and a secondary point along the flow direction is chosen as the receptor point. The solution of the NSE is unit tested to conserve both mass and momentum, and the velocity profile is verified with Poiseuille flow in figure 4.30 on the next page. The conservation of mass is satisfied for simulating the ADE, which is further verified on the original reciprocal relation [55]. To verify the derived generalisations, the velocity field will be exactly reversed to validate the derivation for completely reversible flow, as complete creeping flow cannot be achieved exactly with the LBM. The Reynolds number found are of order 10^{-5}, and the reversibility is therefore satisfied.

4.3.1 Diffusion of matter versus diffusion of heat

The total solute mass, i.e. the concentration field integrated over the domain, is conserved, as the no-flux boundary condition does not allow solute to leave or enter the system. For the temperature field, this is not necessarily the case. Diffusion of temperature interacts with the boundary such that the total temperature is no longer conserved. Due to the total temperature not being conserved, the reciprocal relation previously derived does not necessarily hold for the diffusion of temperature. To the left in figure 4.31 on the following page, the reciprocal relation for the diffusion of temperature at the injection and receptor point are shown to be in excellent agreement. The simulation was performed in a general geometry, where the solute must interact with the boundary to reach the receptor

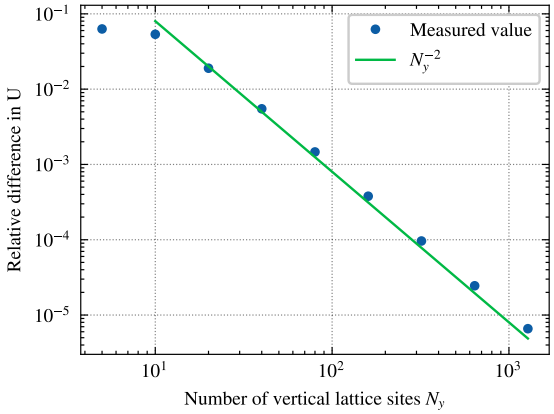

Figure 4.30: The deviation between the average velocity found numerically and analytically for Poiseuille flow follows the inverse square of the number of vertical lattice points. The horizontal axis can be interpreted as the inverse Knutsen number, which must be small to reproduce a solution of the Navier–Stokes equations. From the measured decrease, we believe the LBM is implemented correctly.

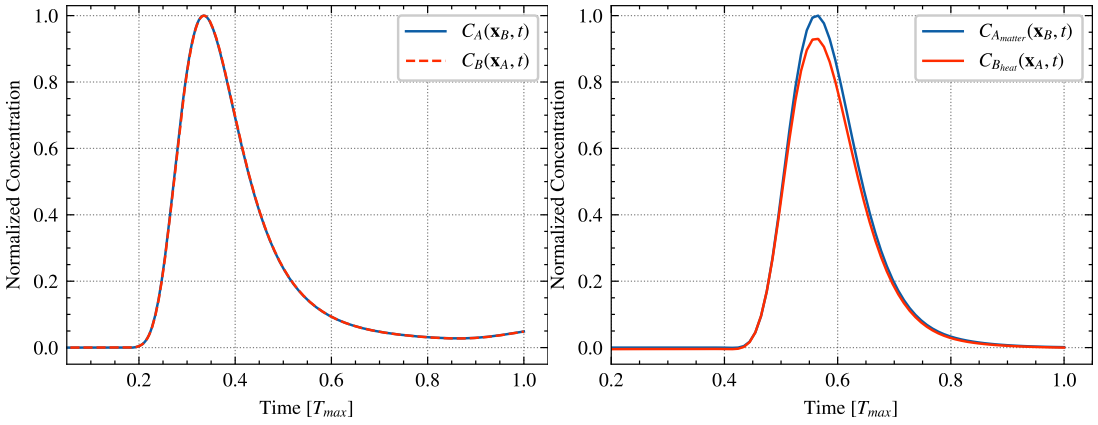

Figure 4.31: The reciprocal relation is tested for the diffusion of temperature instead of mass. To the left, we see that the relation holds when temperature is diffusing both ways. To the right, mass is diffusing one way and temperature the other. Here we see a clear deviation, where the diffusing temperature is always smaller than the mass. This is due to the absorbing boundary conditions not conserving the fluid's total temperature.

point. Based on the result, we conclude that the reciprocal relation holds for the diffusion of temperature and matter. In the derivation of the reciprocal relation, one assumes a materially closed system where the surface integrals containing the concentration vanishes (2.65), and should therefore not hold for heat diffusion when the boundary temperature is fixed. Nevertheless, based on the numerical simulation, it seems as if the relation still holds. When injecting matter one way and temperature the other, we find the curve displayed to the right of the same figure. Here, the curves do not overlap, although their shape is very similar. Due to the total temperature not being conserved, some of it is lost when interacting with the porous media in which the simulation is performed, resulting in a smaller quantity reaching the receptor point. The relation, therefore, holds approximately true when comparing the concentration profile originating from mass and temperature, compared to injecting mass or temperature at both points.

From the above figure, one can measure the deviation between the two concentration profiles as an integral over the absolute difference

$$\text{Error} = \frac{\int_0^T \left| C_{A_{\text{matter}}}(\boldsymbol{x}_B, t) - C_{B_{\text{heat}}}(\boldsymbol{x}_A, t) \right| \mathrm{d}t}{\int_0^T C_{A_{\text{matter}}}(\boldsymbol{x}_B, t) \mathrm{d}t}, \tag{4.58}$$

where T is the total simulation time. With this definition, a value of zero would be achieved for the case of matter diffusing both ways for completely reversible flow, but will take a non-zero value when heat is diffusing one way and matter the other, as we saw in figure 4.31. If most of the temperature has been absorbed by the boundary, its value will approach 1. How this error function depends on the Peclet number is displayed in figure 4.32 on the next page, for three different distances between the receptor and injection point. For large values of the Peclet number, the concentration reaches the receptor point in a shorter amount of time, with a narrower distribution. Since the main mechanism behind the deviation is believed to be due to absorption of the temperature when interacting with the boundaries, a large Peclet number should decrease the error, as it allows for less boundary interaction on the journey from injection to receptor point. This explains the behaviour observed in the figure, where the error approaches one in the limit of low Peclet numbers, meaning the heat concentration is approximately zero at the receptor point. The error approaches zero in the limit of large Peclet numbers, where the boundary interaction is negligible. With increasing distance between the receptor and injection point, the solute spreads out more before reaching its target, thus interacting more with the boundaries. This makes a larger Peclet number necessary to reach a lower error value compared to the shorter diffusion distance, as seen in the figure. Additionally, an error of 1 is reached for larger values of the Peclet number when the distance is larger, but some fluctuation is observed around this saturation value.

4.3.2 Optimizing injection method

For possible applications of the reciprocal relation, one might want to maximise the concentration reaching the receptor point relative to the total injected mass. To test different injection methods, we implement a line of measurements along the channel width in our

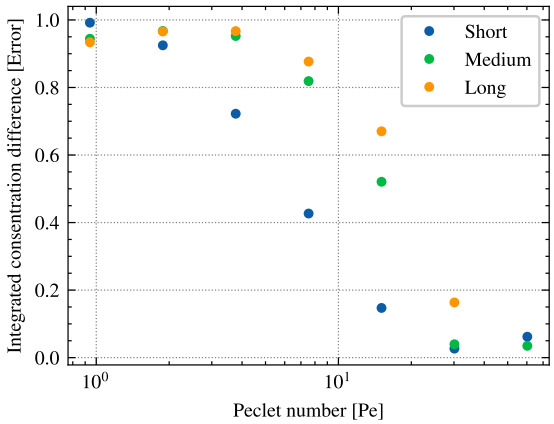

Figure 4.32: The reciprocal relation does not hold exactly when matter is diffusing one way and temperature the other, due to absorption of the temperature with the boundary. This deviation, quantified by the error function (4.58), reduces with an increasing Peclet number until it saturates close to zero. In the limit of small Peclet numbers, the error approaches one, as the entire temperature field has been equilibrated with the boundary. With increasing distances between the injection and receptor point, given by the legend, a larger Peclet number is necessary to achieve the same error value.

numerical simulation. The concentration from the initial injection is measured along this line, and is injected along the same line with reversed flow to maximise the concentration at the original injection point. For all the injection methods, the *first-in, last-out* method is employed. With this method, the first concentration to reach the receptor point will be the last one injected with reversed flow. The different injection methods are tested numerically and are defined by their cutoff value; for a cutoff value of 1/2, one only injects the concentration with the reversed flow if the value was larger than 1/2 of the maximal measured value along the line. The measured concentration with the reversed flow is displayed in figure 4.33 on the facing page. An additional injection method, labelled *max for each pos*, injects the maximal concentration at each position along the line using the *first-in, last-out* method. From the figure, we see that a single injection, only at the maximal value measured along the receptor line, will result in the maximal concentration of the initial injection point. This result appears intuitive, as the advection-diffusion equation is linear, and the sum of multiple different injections cannot give rise to a higher relative concentration than the maximal value found for the spatial point of extremal concentration. To achieve a sharp peak, one should employ a single injection at the point along the line where the total maxima was measured.

4.3.3 General injection methods

The original derivation of the reciprocal relation [55] was carried out assuming a Dirac-delta point injection in both space and time. Performing a similar calculation, one can derive an equivalent reciprocal relation for an injection $I_A(t)$ at point $\boldsymbol{x}_A$, and $I_B(t)$ at $\boldsymbol{x}_B$.

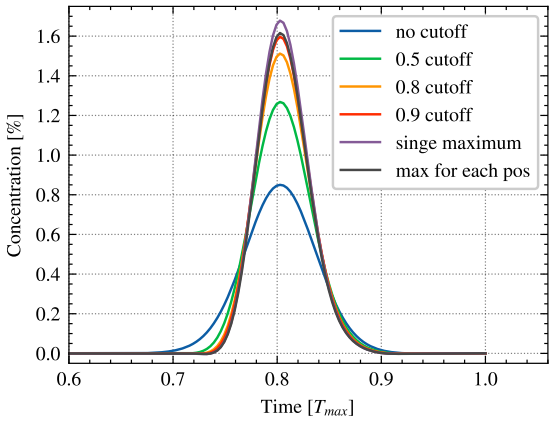

Figure 4.33: Different injection methods are tested to find the method which maximises the concentration at the initial injection point. The concentration originates from injections along a vertical line. The simulation shows that the answer one would intuitively expect, a single injection at the point where the maximal concentration was measured along the line, is the one that maximises the concentration at the receptor point.

The derivation then yields the relationship

$$\int_0^t C_A(\boldsymbol{x}_B, \tau) I_B(t-\tau) \mathrm{d}\tau = \int_0^t C_B(\boldsymbol{x}_A, \tau) I_A(t-\tau) \mathrm{d}\tau, \tag{4.59}$$

which reduces to the standard reciprocal relation if both injections are Dirac-delta distributions. We investigated the theoretical prediction numerically for a Heaviside injection at $\boldsymbol{x}_B$, and a Dirac-delta at $\boldsymbol{x}_A$, resulting in the theoretical prediction

$$\int_0^t C_A(\boldsymbol{x}_B, \tau) \mathrm{d}\tau = C_B(\boldsymbol{x}_A, t). \tag{4.60}$$

One can take the integral of the concentration measured at $C_A(\boldsymbol{x}_B, t)$ to predict the concentration at $C_B(\boldsymbol{x}_A, t)$, or likewise take the derivative of $C_B(\boldsymbol{x}_A, t)$ to find $C_A(\boldsymbol{x}_B, t)$. The theoretical prediction is tested versus simulation in figure 4.34 on the next page. To the left, the measured concentrations are displayed, and to the right, the integrated pulse injection is seen to be in excellent agreement with the measured concentration resulting from the step injection. Over both simulations, the total injected concentration amount to the same mass, and the integral is performed with respect to a time array varying from 0 to 1 over the simulation period. From the measurements, we conclude that the theoretical prediction of equation (4.60) is correct.

For a Dirac-delta injection in time with a general spatial dependence $\delta(t) f(\boldsymbol{x})$, the reciprocal relation can be expressed in terms of volume integrals

$$\int_\Omega f_B(\boldsymbol{x}) C_A(\boldsymbol{x}, t) \mathrm{d}^3\boldsymbol{x} = \int_\Omega f_A(\boldsymbol{x}) C_B(\boldsymbol{x}, t) \mathrm{d}^3\boldsymbol{x}. \tag{4.61}$$

Information regarding the exact concentration value at different positions is lost for spatially dependent injections, but the integrated amount is still equal.

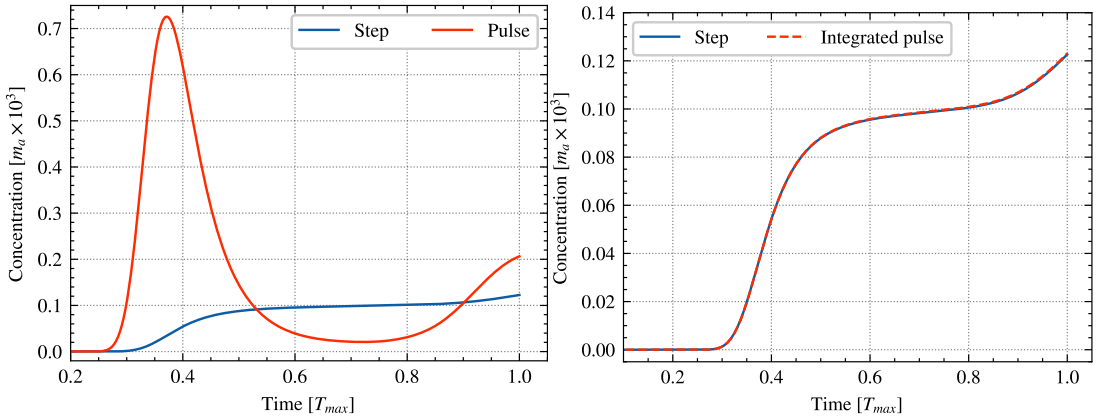

Figure 4.34: The theoretical prediction for the generalization of the reciprocal relation for time-dependent injection (4.59) is verified by a numerical simulation for a heavy-side and Dirac-delta function injection (4.60). The measured concentrations are displayed in the left figure, and the integrated concentration originating from the pulse injection, where they are shown to be in good agreement. If one were to perform an integral over the concentration originating from the pulse injection, a similar agreement would be observed.

4.3.4 Reciprocal relation for different transport scaling

The reciprocal relation is known to hold when the molecular diffusion coefficient is the same for both injections. Here we investigate if a change in the diffusion coefficient can be compensated by a change in the average velocity U, such that the reciprocal relation still holds. By performing a rescaling with a factor α of both the average velocity U and the diffusion coefficient D_m, the Peclet number remains the same, and the advection-diffusion equation takes the form

$$\frac{\partial C}{\partial t} = \alpha D_m \nabla^2 C - \alpha \nabla \cdot (\boldsymbol{u} C) + m\delta(\boldsymbol{x} - \boldsymbol{x}_0)\delta(t). \tag{4.62}$$

By additionally scaling the time by the inverse of the same constant, t/α, and using properties of the Dirac-delta function, we find that all the α's cancel each other. The regular advection-diffusion equation is obtained, which is the starting point of deriving the reciprocal relation. Thus, the reciprocal relation should hold with a different diffusion coefficient, as long as the Peclet number takes the same value, and the time is scaled by the inverse of the factor change of the diffusion coefficient. This is verified numerically in figure 4.35 on the facing page, where the two concentration profiles overlap after performing a rescaling of the time, agreeing with the theoretical prediction.

4.3.5 Reciprocal relation for time-dependent flow

The original derivation of the reciprocal relation [55] assumes a time-independent flow. Performing a similar derivation, but allowing the velocity field to depend on time, the same relation can be achieved by performing a Laplace transform instead of a Fourier

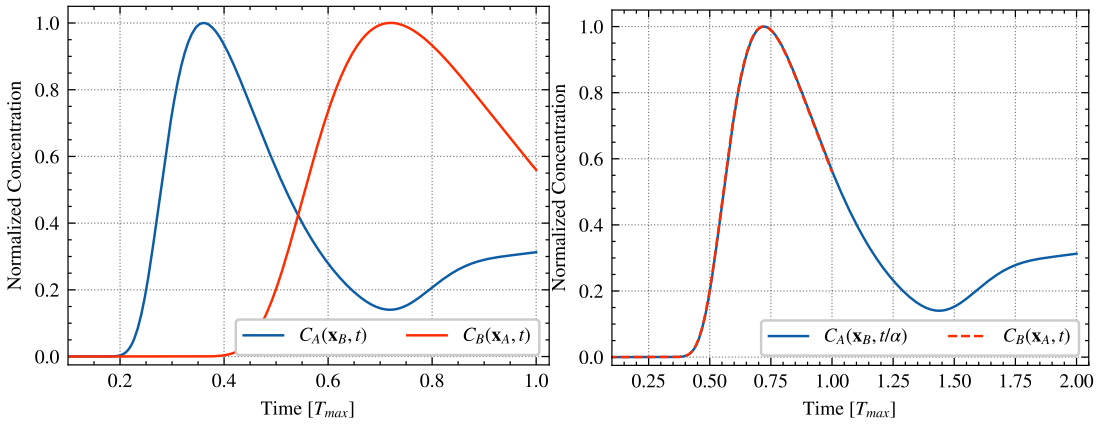

Figure 4.35: The reciprocal relation is shown to hold for a rescaling of the equation, where the Peclet number is the same, but the diffusive and advective transport rates are each scaled by a factor α. The measured concentration is displayed to the left, and displayed to the right with rescaled time. Here we arbitrarily chose $\alpha = 1/2$. The concentration in the right figure is in good agreement, and the reciprocal relation holds true as long as the Peclet number is the same for the two different injections.

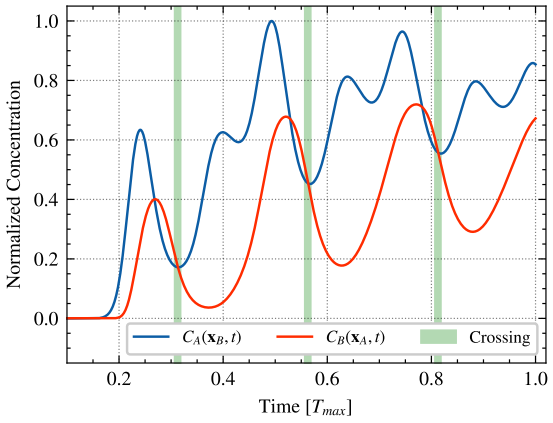

Figure 4.36: The reciprocal relation is tested for oscillating time-dependent forces, where the analytic calculation (4.63) predicts the crossing of the two concentrations at the points highlighted by the green vertical lines. This prediction is in excellent agreement with the simulation.

transform. If the velocity satisfies the equality

$$\int_0^t \mathrm{d}\tau \ \boldsymbol{u}_B(\boldsymbol{x}, t-\tau) = -\int_0^t \mathrm{d}\tau \ \boldsymbol{u}_A(\boldsymbol{x}, \tau), \tag{4.63}$$

we will still end up with the standard form of the reciprocal relation

$$\frac{1}{m_A} C_A(\boldsymbol{x}_B, t) = \frac{1}{m_B} C_B(\boldsymbol{x}_A, t). \tag{4.64}$$

Sadly, the convolution in equation (4.63) cannot be satisfied for all times t for a given solution of the NS equations. We can still make the velocity fields satisfy equation (4.63) for specific points in time. This theoretical prediction is tested with an oscillating body force

$$\boldsymbol{f}_A = \boldsymbol{f}_0 \cos(\omega t), \qquad \boldsymbol{f}_B = -\boldsymbol{f}_0 \sin(\omega t). \tag{4.65}$$

With this choice of forces at low Reynolds numbers, the convolution integral (4.63) will be satisfied for specific points in time. This is tested in a simulation and displayed in figure 4.36 on the previous page. The green vertical lines, representing the predicted crossing using (4.63), agree excellently with the crossing found numerically. Therefore, the reciprocal relation remains true for time-dependent flow, as long as the convolution is satisfied. The behaviour of the two concentrations does not appear similar, likely due to the difference in geometry around the measurement point. The analytic prediction only lets us say something about the concentration at single points in time for a single spatial position, and the behaviour outside of these points is entirely unknown.

4.3.6 Symmetry of dispersion tensor under reversal of flow

From studying Brenner's equations (2.92b) one cannot immediately determine how the interchange of $\boldsymbol{u} \to -\boldsymbol{u}$ will effect the dispersion tensor. The velocity field occurs both independently, and as a product with the Brenner field, in addition to the solution of the equation appearing both linearly and quadratically in the expression for the effective dispersion tensor (2.92a). It is therefore not trivial if the effective dispersion tensor will stay invariant under inversion of the velocity field. The derivation of Brenner theory, described in section 2.3.4 on page 19, begins with the definition of the local moments (2.71)

$$\boldsymbol{\mu}_m(\boldsymbol{r}, t) \equiv \sum_n \boldsymbol{R}_n^m \ P(\boldsymbol{R}_n, \boldsymbol{r}, t | \boldsymbol{R}_{n'}, \boldsymbol{r}') = \sum_n \boldsymbol{R}_{n'+n}^m \ P(\boldsymbol{R}_{n'+n}, \boldsymbol{r}, t | \boldsymbol{R}_{n'}, \boldsymbol{r}'), \tag{4.66}$$

where the sum was shifted to be relative to the unit cell of injection. The probability P is the conditional probability of being at the local position $\boldsymbol{r}$ in a unit cell with position $\boldsymbol{R}_n$ at a time t, given an injection at position $\boldsymbol{r}'$ within a unit cell with the position $\boldsymbol{R}_{n'}$.

For an injection $f_A(\boldsymbol{r})\delta(t)$, resulting in the probability density P_A, and likewise for the probability density P_B, the reciprocity relation takes the form

$$\int_\Omega \mathrm{d}^3\boldsymbol{r} P_B^-(\boldsymbol{r}, t) f_A = \int_\Omega \mathrm{d}^3\boldsymbol{r} P_A(\boldsymbol{r}, t) f_B, \tag{4.67}$$

where the minus sign superscript denotes the probability density with reversed velocity field. This equality can be written in the notation of Brenner theory

$$\sum_n \int_\Omega \mathrm{d}^3\boldsymbol{r} P_B^-(\boldsymbol{R}_n, \boldsymbol{r}, t) f_A(\boldsymbol{R}_n, \boldsymbol{r}_A) = \sum_n \int_\Omega \mathrm{d}^3\boldsymbol{r} P_A(\boldsymbol{R}_n, \boldsymbol{r}, t) f_B(\boldsymbol{R}_n, \boldsymbol{r}_B). \tag{4.68}$$

For a unity injection over the whole unit cell, we can write $f_A = \delta_{nA}$, and likewise for B,

$$\int_\Omega \mathrm{d}^3\boldsymbol{r} P_B^-(\boldsymbol{R}_A, \boldsymbol{r}, t|\boldsymbol{R}_B) = \int_\Omega \mathrm{d}^3\boldsymbol{r} P_A(\boldsymbol{R}_B, \boldsymbol{r}, t|\boldsymbol{R}_A). \tag{4.69}$$

The index of the unit cell can be written in terms of their distance $B - A = N$

$$\int_\Omega \mathrm{d}^3\boldsymbol{r} P_B^-(\boldsymbol{R}_{B-N}, \boldsymbol{r}, t|\boldsymbol{R}_B) = \int_\Omega \mathrm{d}^3\boldsymbol{r} P_A(\boldsymbol{R}_{A+N}, \boldsymbol{r}, t|\boldsymbol{R}_A). \tag{4.70}$$

The position of the initial injections A and B are fixed for a single measurement, but with a periodic unit cell the equality must hold for any value of their distance N. One can view this as performing the experiment with increasing distances between the unit cell, and finding that the integrated probabilities agree for each distance seperately. We therefore include a sum over N on each side of the equation, and multiply with the m'th moment of the unit cell position

$$\int_\Omega \mathrm{d}^3\boldsymbol{r} \sum_N R_N^m P_B^-(\boldsymbol{R}_{B-N}, \boldsymbol{r}, t|\boldsymbol{R}_B) = \int_\Omega \mathrm{d}^3\boldsymbol{r} \sum_N R_N^m P_A(\boldsymbol{R}_{A+N}, \boldsymbol{r}, t|\boldsymbol{R}_A). \tag{4.71}$$

Inverting the axis on the left hand side, the equality becomes

$$(-1)^m \int_\Omega \mathrm{d}^3\boldsymbol{r} \sum_N R_N^m P_B^-(\boldsymbol{R}_{B+N}, \boldsymbol{r}, t|\boldsymbol{R}_B) = \int_\Omega \mathrm{d}^3\boldsymbol{r} \sum_N R_N^m P_A(\boldsymbol{R}_{A+N}, \boldsymbol{r}, t|\boldsymbol{R}_A). \tag{4.72}$$

The terms inside the unit cell integral are identical to the definition of the local moments (4.66). The unit cell integral of the local moments define the total moments (2.78), such that

$$(-1)^m \boldsymbol{M}_m^- = \boldsymbol{M}_m. \tag{4.73}$$

Therefore, the even moments are the same with the reversed velocity field, while the odd moments change sign. This agrees with the first total moment being Ut, and must therefore change sign when reversing the velocity field. The total moments are used to calculate the dispersion tensor (2.89), where the second-order total moment appears linearly, and the first-order moment appears quadratically. Therefore, the sign change of odd moments is irrelevant, making the dispersion tensor invariant under the reversal of the velocity field

$$D_{ij} = D_{ij}^-. \tag{4.74}$$

This result has been verified on the parallel diffusion coefficient for two-dimensional channels without vertical axial symmetry. For a velocity field satisfying the time-dependent convolution integral (4.63), the above arguments still hold, but now only limited to specific points in time. It is therefore not evident whether the time-averaged dispersion tensor is invariant.

4.3.7 Discussion and possible applications

There are two interesting aspects of the reciprocity relation. Firstly, a meaningful notion of reversibility of the irreversible process of dispersion can be made. This reversibility is independent of the Peclet number, as long as the flow is reversible. The second aspect is that if a point can initially be made an injection point, the measured concentration from this injection can perfectly predict the concentration at the injection point from a second injection elsewhere in the system. Therefore, a downside of this method is that the position where one wants to predict the concentration must be accessible for injection. If one desires a concentration at that point, it would be much simpler and more efficient to inject the desired concentration directly at the point. For cases where the point is inaccessible to any form of injection, the reciprocity relation is no longer applicable.

To this end, a part of this investigation is motivated by generalising the reciprocity relation to cases where one cannot access the point directly for the injection of matter. With the theoretical generalisations derived in this section in mind, one can heat the inaccessible point with a sharply focused laser. This represents an injection of increased temperature, which will diffuse with the flow. By performing temperature measurements in the accessible region, one can use equation (4.59) with the temperature measurements and the known form of the laser injection to decide which of the measurement points will result in the maximised arrived concentration at the inaccessible point. In general, heat will diffuse faster than a solute. By reversing the flow, scaled to some factor to keep the Peclet number unchanged, the concentration arriving at the inaccessible point can be determined. Other laser injections can also be made to avoid heating the region to dangerous temperatures. This process is much more complicated than simply performing pulse injections of matter at both points, and some errors will most likely accumulate at each step. In theory, one can now apply the reciprocal relation to predict the concentration at a point inaccessible to the injection of matter.

More work is necessary to investigate if the reciprocal relation can be applied to medical prediction and placement of a solute in tissue. An obvious continuation of the investigation would be to characterise diffusion coefficients of varying solutes of medical interest and the Peclet numbers possible while still being in the creeping flow regime. To maximise the amount of solute reaching the desired target, the Peclet number should be maximised. The system already sets the length scale, but the distance between the injection and receptor point should be minimised. The diffusion coefficient is somewhat fixed but can be altered by changing the temperature and viscosity of the surrounding liquid (2.36). Therefore, the problem is equivalent to maximising the Schmidt number, ideally at low temperatures, satisfying $\mathrm{Re} < 0.01$ [55]. The process of accurately measuring concentrations and reversing velocity profiles must also be investigated experimentally.

While the extension of the reciprocal relation to time-dependent flow increases its applicability beyond the original result, it is hard to imagine its applications. The convolution requirement (4.63) is challenging to satisfy, and if satisfied, it only holds for single points in time. Still, situations where the concentration of a single position at a single point in time might be used in reaction systems or to extract information about the system. More complicated injection methods should also be employed to further verify the analytic pre-

diction of equation (4.60). An interesting continuation of the reciprocal relation would be to study its applicability to compressible flow. For compressible flow, the entropy production of the solute can be reduced compared to that of incompressible flow [93], and the reciprocal relation might apply to minimising the net entropy production of the solute.

How the reciprocal prediction breaks down at larger Reynolds number has already been studied numerically [55]. Analytical approaches were made to quantify the measured deviation, but the expressions, even for small non-zero Reynolds numbers, proved challenging to make definitive statements from. A Reynolds number of 0.01 is large enough for the non-linear term in the Navier–Stokes equations to create significant differences in the measured concentration in the injection and receptor point [55]. This somewhat strict limit for the applicability of the reciprocity relation is satisfied for many small scale naturally occurring systems [57], especially for the placement and prediction of a concentration within biological tissue.

The symmetry of the dispersion tensor under reversal of the flow is, to our knowledge, neither discussed nor derived in the literature. This may be due to the result being intuitive and assumed to hold true. Nevertheless, the derivation proposed here gives a quantitative argument for why it holds true and under what conditions. Following the result from Flekkøy [55], one would expect the symmetry to break at around $\mathrm{Re} = 0.01$. Although the result has only been verified in two-dimensional channels, the analytic expression indicates that the symmetry should persist to multiple dimensions. Investigating whether the inversion symmetry of the dispersion tensor holds true for time-dependent flows would be a natural starting point for future work.

Chapter 5

Conclusion

The spreading of a solute is enhanced by the fluid shear of the background velocity field, making it essential for various industrial applications and for describing the transport properties of pollutants and chemical agents in natural systems. This thesis aimed to extend the understanding of dispersion by investigating solute transport in flows with complex geometric confinement. Two important geometrical properties have been found to result in novel phenomena of the dispersion tensor; a decrease with Reynolds numbers for discontinuous geometries and a resonance phenomena in oscillating flows with a sinusoidal boundary. Additionally, Brenner's theory of effective diffusion in spatially periodic porous media [41, 42] has successfully been generalised to time-dependent flows, and a reciprocity relation [55] extended to different types of flow, injections and diffusion. Areas for further investigations have been proposed, with a particular focus on understanding and predicting the resonance wavelength for a broader set of parameters and geometries.

Despite the ubiquity of rough surfaces, it was unknown how fluid flow, especially with high inertia, interplay with the discontinuous boundary roughness to influence the effective dispersion. Both industrial [33, 36, 38] and natural systems [29, 30, 32] can often contain jumps and rugged shapes resulting in reticulation zones, which are known to have a large impact on the effective dispersion [25, 26]. Contrary to what has previously been found for smooth boundaries, recirculation zones were found to appear for all boundary amplitudes in our geometry, resulting in a large increase in the effective dispersion compared to a straight channel, even for small boundary amplitudes. The addition of fluid inertia could either decrease or increase the effective dispersion depending on the Peclet number, where the relative decrease was at its largest 50%. Increasing fluid inertia was believed to increase the effective dispersion [26], in clear contradiction to the measured decrease. Based on random walk simulations, the behaviour can be explained by recirculation zones being more accessible and difficult to escape with increasing Reynolds number, resulting in less spread between particles in the high Peclet regime.

Unsteady flows are routinely applied to microfluidic devices and lab on a chip technology [47, 48] to increase the dispersion [43, 44], and occur in a variety of naturally occurring systems [21, 52–54]. However, the combined effect of a varying boundary and an oscillating flow had to our knowledge not been studied. Brenner theory [41, 42] assumes a

stationary velocity field, and was therefore generalised for the purpose of this investigation. The derived theory agrees with random walk simulations and represents a new theoretical framework for calculating the effective dispersion tensor in any periodic environment with an arbitrary time dependence of the incompressible velocity field. The increase of both boundary amplitude and wavenumber were found to solely decrease the effective dispersion, except around the resonance peak and with the appearance of recirculation zones, which resulted in a large increase in the effective dispersion. The addition of a varying boundary has shown to produce novel phenomena compared to previous work. One new aspect is that the effective dispersion consists of overtones of the ground frequency, though vanishingly small for the parameter space scanned. The novel appearance of a resonance-like behaviour between the wavelength of the boundary and the oscillating driving force has not been previously observed, and allows for tuning of the dispersion. A physical explanation for the resonance wavelength was provided, although an extended, systematic investigation serves as a natural continuation of the work presented here.

The reciprocity relation allows for a notion of reversibility and the prediction of the concentration profile at a specific position within the system, independent of the magnitude of molecular diffusion [55]. Combining the results allows for the measurement of an initial time-dependent temperature injection, at a point inaccessible to the injection of matter, to be used to predict the resulting concentration profile with the reversed velocity for the diffusion of matter with a different diffusivity. The generalization can, in principle, be used to access an otherwise inaccessible point and maximize the amount of concentration at that point. While theoretically possible, successful implementation of this procedure in practical settings first requires experimental validation.

The results presented in this thesis opens up new questions and avenues of research. Specific theoretical research directions have been proposed for each system, but more investigations are also necessary to further understand the effect of geometry, not only on dispersion, but on mixing in general. This is particularly relevant to the transient regime. For small values of the molecular diffusion coefficient, the asymptotic regime is only reached after a long time $t \gg a^2/D_m$, and for processes with exceedingly high Peclet number, the relevance of asymptotic dispersion coefficients may even be questionable [94]. In the transient regime, solute filaments undergo successive stretching and folding events, and the mixing is classified as chaotic if the filament elongations grow exponentially in time. These properties cannot be captured by the dispersion tensor and must therefore be understood independently. The geometries studied here can potentially achieve chaotic mixing by extending the geometric variations to three dimensions, adding a second fluid phase, or breaking time-invariance, as already done in this work. A stretching-and-folding behaviour was observed in random walk simulations with the perturbed expression for non-reversible oscillating flow with a varying boundary, but it was not investigated whether the mixing dynamics were actually chaotic. The perturbed analytic velocity field might aid in further research on chaotic mixing. Additionally, a reaction term can be included in the advection-diffusion equation, where chaotic mixing can result in much faster reactions than what can be predicted from Taylor dispersion.

Experimentally, the results provided here can potentially be verified in Hele-Shaw cells. The systems can be made quasi-two-dimensional by having no spatial variations along the

cell's width, with the shortest side giving the channel height, similarly to the work by Roht et al. [49, 95]. Measurements of the evolution of an initial line injection of concentration can verify the resonance behaviour by including a sinusoidal boundary. The sinusoidal boundary might only be included at one side of the channel height to make measurements of the concentration's evolution from the opposite side possible. Discussions on how to realise this system experimentally are already underway with experimentalists at PoreLab.

Appendices

Appendix A

Derivation of time-dependent Brenner theory

The goal of this derivation is to find a general set of equations which can be solved to produce an expression for the dispersion tensor in an arbitrary geometry, valid for both stationary and time dependent flow. The main aspects and definitions in this derivation are equal to Brenner's original derivation, which is summarized in section 2.3.4 on page 19. For example are the local moments defined in the same way (2.71), and must still satisfy an advection-diffusion type equation (2.72). The jump conditions are still defined as in equation (2.73) and (2.74), making the jump in the local moments the same as well:

$$[\![\mu_0]\!] = 0, \qquad [\![\boldsymbol{\mu}_1]\!] = -[\![\boldsymbol{r}\mu_0]\!], \qquad \text{and} \qquad [\![\boldsymbol{\mu}_2]\!] = -\left[\!\!\left[\frac{\boldsymbol{\mu}_1\boldsymbol{\mu}_1}{\mu_0}\right]\!\!\right]. \tag{A.1}$$

The jump conditions on the gradients of the local moments also take the same form:

$$[\![\nabla\mu_0]\!] = 0, \qquad [\![\nabla\boldsymbol{\mu}_1]\!] = -[\![\nabla\boldsymbol{r}\mu_0]\!], \qquad \text{and} \qquad [\![\nabla\boldsymbol{\mu}_2]\!] = -\left[\!\!\left[\nabla\frac{\boldsymbol{\mu}_1\boldsymbol{\mu}_1}{\mu_0}\right]\!\!\right]. \tag{A.2}$$

With the total moments of order m being expressed in the jump conditions of the local moments of order m, we find

$$\frac{\mathrm{d}\boldsymbol{M}_m}{\mathrm{d}t} = -\sum_{j=1}^{d}\int_{s_j}\mathrm{d}\boldsymbol{s}\cdot\boldsymbol{u}\,[\![\boldsymbol{\mu_m}]\!] + D\sum_{j=1}^{d}\int_{s+j}\mathrm{d}\boldsymbol{s}\cdot[\![\nabla\boldsymbol{\mu}_m]\!] + \delta_{m0}\delta(t). \tag{A.3}$$

The total moment of second-order can therefore be expressed in terms of the jump conditions of the first order local moments, using equation (A.1) and (A.2). When the local moments are known, the dispersion tensor can be calculated using

$$D_{ij} = \frac{1}{2}\frac{\mathrm{d}}{\mathrm{d}t}\left(M_{2_{ij}} - M_{1_i}M_{1_j}\right). \tag{A.4}$$

In principle, we can solve these equations in time. This is equivalent to solving two linear advection-diffusion equations, but is much more demanding than the procedure that directly gives us the asymptotic dispersion coefficient from Brenner's approach. Therefore,

we will look for solutions to the above equations in the asymptotic regime, setting all exponentials and other decaying terms to zero.

So far, nothing has changed compared to the derivation of the original Brenner theory. Therefore, we will begin to solve for the local moments and allow the velocity field to be time dependent. The zeroth-order solution, representing the conservation of mass, is the same with and without time-dependent flows,

$$\mu_0 = \frac{1}{\Omega_f}. \tag{A.5}$$

The first order total moments takes the same form as in the earlier derivation in equation (2.81), but is not time dependent:

$$\frac{\mathrm{d}M_{1_i}}{\mathrm{d}t} = \frac{1}{\Omega}\int_\Omega \mathrm{d}^3 r\ u_i(t) = \langle u_i(t)\rangle. \tag{A.6}$$

Integrating both sides with respect to time gives the time-dependent part of the first order total moments

$$M_{1_i}(t) = \int_0^t \langle u_i(t')\rangle \mathrm{d}t' \equiv \chi_i(t) \tag{A.7}$$

$$M^2_{1_{ij}}(t) = \int_0^t \int_0^t \langle u_i(t')\rangle\langle u_j(t'')\rangle \mathrm{d}t'\mathrm{d}t'' \tag{A.8}$$

To satisfy the above differential equation (A.6), we guess on a solution on the form

$$\mu_1 = \frac{1}{\Omega_f}\left[\boldsymbol{\chi}(t) + \mathbf{B}(\mathbf{r},t) - \mathbf{r}\right] \tag{A.9}$$

The jump condition of the spatialy constant term χ is trivial zero $[\![\chi]\!] = 0$, thus using equation (A.1) fixes the jump condition on the unknown B_i to vanish. Additionally we can use the Gauge freedom in B_i to make it's unit cell average vanish. Using our guess as input to equation (2.72) gives the auxiliary problem

$$\partial_t B_i + u_j\nabla_j B_i - D_m\nabla^2 B_i = u_i(\boldsymbol{x},t) - \langle u_i(t)\rangle \tag{A.10}$$

$$\hat{n}_j\nabla_j B_i = \hat{n}_i. \quad \text{on} \quad \partial\Omega. \tag{A.11}$$

Comparing this expression to the original (2.92b), we see that the only difference is an additional time derivative on the left hand side. We therefore retrieve the original Brenner theory for time-independent flows.

To find the dispersion tensor we calculate the derivative of the second order total moment using equation (A.3). The jump condition in the first term takes the form

$$\left[\!\!\left[\frac{\mu_{1_i}\mu_{1_j}}{\mu_0}\right]\!\!\right] = \frac{1}{\Omega_f}\left[\!\left[\left(\chi_i(t) + C_i(\boldsymbol{r},t)\right)\left(\chi_j(t) + C_j(\boldsymbol{r},t)\right)\right]\!\right] = -\frac{1}{\Omega_f}\left(\chi_i\left[\!\left[r_j\right]\!\right] + \left[\!\left[r_i\right]\!\right]\chi_j - \left[\!\left[C_iC_j\right]\!\right]\right). \tag{A.12}$$

Where we have defined the spatial part of the first order local moment as

$$C_i \equiv B_i(\boldsymbol{r}, t) - r_i. \tag{A.13}$$

With a jump condition $[\![C_i]\!] = -[\![r_i]\!]$. The jump condition in the second term of equation (A.3) is calculated using the product rule

$$\left[\!\!\left[\nabla_k \frac{\mu_{1_i}\mu_{1_j}}{\mu_0}\right]\!\!\right] = \frac{1}{\Omega_f}\left([\![(\nabla_k C_i)C_j]\!] + [\![(\nabla_k C_j)C_i]\!]\right). \tag{A.14}$$

Rewriting the jump conditions to surface integrals and using the divergence theorem, the time derivative is given by

$$\frac{\mathrm{d}M_{2_{ij}}}{\mathrm{d}t} = \chi_i\langle u_j\rangle + \chi_j\langle u_i\rangle - \langle u_k\nabla_k(C_iC_j)\rangle + D_m\left\langle\nabla_k\left(C_j\nabla_k C_i + \nabla_k C_j C_i\right)\right\rangle. \tag{A.15}$$

Using equation (A.4) the dispersion tensor can be found. The first two terms in the time derivative of M_2 cancel with the M_1 terms, and the third term in M_2 is zero. The resulting terms are

$$D_{ij} = \lim_{t\to\infty}\left\langle D_m\left(\delta_{ij} - \nabla_i B_j - \nabla_j B_i + \nabla_k B_i \nabla_k B_j\right)\right\rangle. \tag{A.16}$$

Exactly the same as for stationary flows (2.92a). This limit is not clearly defined when the velocity is time dependent. We define instead a time averaged dispersion tensor:

$$\overline{D}_{ij} = \lim_{t\to\infty}\frac{1}{\tau}\int_t^{t+\tau} D_{ij}(t')\mathrm{d}t', \tag{A.17}$$

where the bare denotes the time averaged quantity. Hence, the dispersion tensor can be written as

$$\overline{D}_{ij} = \lim_{t\to\infty}\left\langle D_m\left[\delta_{ij} - \nabla_i\overline{B}_j - \nabla_j\overline{B}_i + \overline{\nabla_k B_i \nabla_k B_j}\right]\right\rangle. \tag{A.18}$$

For a channel or pipe, D_{xx} is the interesting part of the dispersion tensor, which gives the effective diffusion coefficient parallel with the flow. The auxiliary problem, for which we seek time-dependent solutions, then becomes

$$(\partial_t + \mathbf{u}\cdot\boldsymbol{\nabla} - D_m\nabla^2)B_x = u_x', \quad \hat{\mathbf{n}}\cdot\boldsymbol{\nabla}B_x = \hat{n}_x \quad \text{on} \quad \partial\Omega. \tag{A.19}$$

And is used to calculate the xx component of the dispersion tensor, which is equal to the effective diffusion coefficient:

$$D_{\|} = \lim_{t\to\infty}\left\langle D_m\left[1 - 2\partial_x\overline{B_x} + \overline{(\boldsymbol{\nabla}B_x)^2}\right]\right\rangle. \tag{A.20}$$

The change compared to the already established Brenner theory, is therefore only the time derivative in equation (A.10), and the time average when calculating the dispersion tensor (A.17). The more general theory derived here therefore trivally reduces to Brenner theory for stationary flows. Although the change seems small, the addition of a new dimension in which to solve the partial differential equation makes it significantly more difficult to solve analytically, and expensive to solve numerically.

Bibliography

[1] Thomas K. Goldstick, Vincent T. Ciuryla, and Leon Zuckerman. Diffusion of Oxygen in Plasma and Blood. In Jürgen Grote, Daniel Reneau, and Gerhard Thews, editors, *Oxygen Transport to Tissue — II*, Advances in Experimental Medicine and Biology, pages 183–190. Springer US, Boston, MA, 1976.

[2] E. C. Eckstein and F. Belgacem. Model of platelet transport in flowing blood with drift and diffusion terms. *Biophysical Journal*, 60(1):53–69, July 1991.

[3] R. O. Scow, E. J. Blanchette-Mackie, and L. C. Smith. Role of capillary endothelium in the clearance of chylomicrons. A model for lipid transport from blood by lateral diffusion in cell membranes. *Circulation Research*, 39(2):149–162, August 1976.

[4] Donald E. Desaulniers, Ronald S. Kaufmann, John A. Cherry, and Harold W. Bentley. 37Cl-35Cl variations in a diffusion-controlled groundwater system. *Geochimica et Cosmochimica Acta*, 50(8):1757–1764, August 1986.

[5] Chunmiao Zheng and P. Patrick Wang. MT3DMS : a modular three-dimensional multispecies transport model for simulation of advection, dispersion, and chemical reactions of contaminants in groundwater systems; documentation and user's guide. *This Digital Resource was created in Microsoft Word and Adobe Acrobat*, December 1999. Accepted: 2016-03-17T12:45:13Z Publisher: Environmental Laboratory (U.S.).

[6] K.H. Jensen, K. Berg-Sørensen, H. Bruus, N.M. Holbrook, J. Liesche, A. Schulz, M.A. Zwieniecki, and T. Bohr. Sap flow and sugar transport in plants. *Reviews of Modern Physics*, 88(3):035007, September 2016. Publisher: American Physical Society.

[7] Julia Dölger, Hanna Rademaker, Johannes Liesche, Alexander Schulz, and Tomas Bohr. Diffusion and bulk flow in phloem loading: A theoretical analysis of the polymer trap mechanism for sugar transport in plants. *Physical Review E*, 90(4):042704, October 2014. Publisher: American Physical Society.

[8] K. H. Jensen, E. Rio, R. Hansen, C. Clanet, and T. Bohr. Osmotically driven pipe flows and their relation to sugar transport in plants. *Journal of Fluid Mechanics*, 636:371–396, October 2009. arXiv: 0810.4021.

[9] Weiping Ding, Weili Li, Sijie Sun, Xiaoming Zhou, Peter A. Hardy, Suhail Ahmad, and Dayong Gao. Three-Dimensional Simulation of Mass Transfer

in Artificial Kidneys. *Artificial Organs*, 39(6):E79–E89, 2015. _eprint: https://onlinelibrary.wiley.com/doi/pdf/10.1111/aor.12415.

[10] Daniel A. Beard and Fan Wu. Apparent Diffusivity and Taylor Dispersion of Water and Solutes in Capillary Beds. *Bulletin of Mathematical Biology*, 71(6):1366–1377, August 2009.

[11] G. A. Ledezma, A. Folch, S. N. Bhatia, U. J. Balis, M. L. Yarmush, and M. Toner. Numerical Model of Fluid Flow and Oxygen Transport in a Radial-Flow Microchannel Containing Hepatocytes. *Journal of Biomechanical Engineering*, 121(1):58–64, February 1999.

[12] J B Grotberg. Pulmonary Flow and Transport Phenomena. *Annual Review of Fluid Mechanics*, 26(1):529–571, January 1994. Publisher: Annual Reviews.

[13] Nelleke Scheijen. Plastic litter in the ocean: Modeling of the vertical transport of micro plastics in the ocean. 2018.

[14] Hirofumi Hinata, Kazuki Ohno, Noa Sagawa, Tomoya Kataoka, and Hidetaka Takeoka. Numerical modeling of the beach process of marine plastics: 2. A diagnostic approach with onshore-offshore advection-diffusion equations for buoyant plastics. *Marine Pollution Bulletin*, 160:111548, November 2020.

[15] Hrissi K. Karapanagioti and Irene Klontza. Testing phenanthrene distribution properties of virgin plastic pellets and plastic eroded pellets found on Lesvos island beaches (Greece). *Marine Environmental Research*, 65(4):283–290, May 2008.

[16] David S. Hui, Benny K. Chow, Leo C. Y. Chu, Susanna S. Ng, Stephen D. Hall, Tony Gin, and Matthew T. V. Chan. Exhaled Air and Aerosolized Droplet Dispersion During Application of a Jet Nebulizer. *Chest*, 135(3):648–654, March 2009.

[17] I. Eames, J. W. Tang, Y. Li, and P. Wilson. Airborne transmission of disease in hospitals. *Journal of The Royal Society Interface*, 6(suppl_6):S697–S702, December 2009. Publisher: Royal Society.

[18] L. Liu, J. Wei, Y. Li, and A. Ooi. Evaporation and dispersion of respiratory droplets from coughing. *Indoor Air*, 27(1):179–190, 2017. _eprint: https://onlinelibrary.wiley.com/doi/pdf/10.1111/ina.12297.

[19] Geoffrey Ingram Taylor. Dispersion of soluble matter in solvent flowing slowly through a tube. *Proceedings of the Royal Society of London. Series A. Mathematical and Physical Sciences*, 219(1137):186–203, August 1953. Publisher: Royal Society.

[20] R. Aris and Geoffrey Ingram Taylor. On the dispersion of a solute in a fluid flowing through a tube. *Proceedings of the Royal Society of London. Series A. Mathematical and Physical Sciences*, 235(1200):67–77, April 1956. Publisher: Royal Society.

[21] Stephanie M. Schmidt, Mark J. McCready, and Agnes E. Ostafin. Effect of oscillating fluid shear on solute transport in cortical bone. *Journal of Biomechanics*, 38(12):2337–2343, December 2005.

[22] Kalvis M. Jansons. On Taylor dispersion in oscillatory channel flows. *Proceedings of the Royal Society A: Mathematical, Physical and Engineering Sciences*, June 2006. Publisher: The Royal Society London.

[23] G. Drazer, H. Auradou, J. Koplik, and J. P. Hulin. Self-Affine Fronts in Self-Affine Fractures: Large and Small-Scale Structure. *Physical Review Letters*, 92(1):014501, January 2004. Publisher: American Physical Society.

[24] Steve Rosencrans. Taylor Dispersion in Curved Channels. *Siam Journal on Applied Mathematics - SIAMAM*, 57:1216–1241, October 1997.

[25] Diogo Bolster, Marco Dentz, and Tanguy Le Borgne. Solute dispersion in channels with periodically varying apertures. *Physics of Fluids*, 21(5):056601, May 2009.

[26] J. Bouquain, Y. Méheust, D. Bolster, and P. Davy. The impact of inertial effects on solute dispersion in a channel with periodically varying aperture. *Physics of Fluids*, 24(8):083602, August 2012. Publisher: American Institute of Physics.

[27] B. Armaly, F. Durst, Jose Pereira, and B. Schönung. Experimental and Theoretical Investigation of Backward-Facing Step Flow. *Journal of Fluid Mechanics*, 127:473–496, January 1983.

[28] V. Cvetkovic, J. O. Selroos, and H. Cheng. Transport of reactive tracers in rock fractures. *Journal of Fluid Mechanics*, 378:335–356, January 1999. Publisher: Cambridge University Press.

[29] Aldo Fiori and Matthew W. Becker. Power law breakthrough curve tailing in a fracture: The role of advection. *Journal of Hydrology*, 525:706–710, June 2015.

[30] Seonkyoo Yoon and Peter K. Kang. Roughness, inertia, and diffusion effects on anomalous transport in rough channel flows. *Physical Review Fluids*, 6(1):014502, January 2021. Publisher: American Physical Society.

[31] R. N. Yong, A. M. O. Mohamed, and B. P. Warkentin. Principles of contaminant transport in soils. *Principles of contaminant transport in soils.*, 1992. Publisher: Elsevier Science Publishers.

[32] S. Ahmad Mirbagheri. Modeling contaminant transport in soil column and ground water pollution control. *International Journal of Environmental Science and Technology*, 1, June 2004.

[33] Martin Burschka. A diffusion-limited reaction. pages 88–100. May 2007.

[34] S.A. Rice. Diffusion-Limited Reactions, March 1985.

[35] Gea Oswah Fatah Parikesit, Fajar Prasetia, Galih Angga Pribadi, Denny Christian Simbolon, Ginar Yoga Pradhana, Aishah Rumaysa Prastowo, Alex Gunawan, Kutut Suryopratomo, and Indraswari Kusumaningtyas. Textile-based microfluidics: modulated wetting, mixing, sorting, and energy harvesting. *The Journal of The Textile Institute*, 103(10):1077–1087, October 2012. Publisher: Taylor & Francis _eprint: https://doi.org/10.1080/00405000.2012.660756.

[36] Fatemeh Ahmadi, Kenza Samlali, Philippe Q. N. Vo, and Steve C. C. Shih. An integrated droplet-digital microfluidic system for on-demand droplet creation, mixing, incubation, and sorting. *Lab on a Chip*, 19(3):524–535, 2019. Publisher: Royal Society of Chemistry.

[37] Abraham D. Stroock, Stephan K. W. Dertinger, Armand Ajdari, Igor Mezić, Howard A. Stone, and George M. Whitesides. Chaotic Mixer for Microchannels. *Science*, 295(5555):647–651, January 2002. Publisher: American Association for the Advancement of Science Section: Report.

[38] Manda S. Williams, Kenneth J. Longmuir, and Paul Yager. A practical guide to the staggered herringbone mixer. *Lab on a Chip*, 8(7):1121–1129, 2008. Publisher: Royal Society of Chemistry.

[39] J. M. Ottino, S. R. Wiggins, Abraham D. Stroock, and Gregory J. McGraw. Investigation of the staggered herringbone mixer with a simple analytical model. *Philosophical Transactions of the Royal Society of London. Series A: Mathematical, Physical and Engineering Sciences*, 362(1818):971–986, May 2004. Publisher: Royal Society.

[40] M. Mangeat, T. Guérin, and D. S. Dean. Dispersion in two-dimensional periodic channels with discontinuous profiles. *The Journal of Chemical Physics*, 149(12):124105, September 2018.

[41] H. Brenner. Dispersion resulting from flow through spatially periodic porous media. *Philosophical Transactions of the Royal Society of London. Series A, Mathematical and Physical Sciences*, 297(1430):81–133, July 1980. Publisher: Royal Society.

[42] H. Brenner and P. M. Adler. Dispersion resulting from flow through spatically periodic porous media II. Surface and intraparticle transport. *Philosophical Transactions of the Royal Society of London. Series A, Mathematical and Physical Sciences*, 307(1498):149–200, October 1982. Publisher: Royal Society.

[43] Søren Vedel and Henrik Bruus. Transient Taylor–Aris dispersion for time-dependent flows in straight channels. *Journal of Fluid Mechanics*, 691:95–122, January 2012. Publisher: Cambridge University Press.

[44] Harry M. Taylor and Edward F. Leonard. Axial dispersion during pulsating pipe flow. *AIChE Journal*, 11(4):686–689, 1965. _eprint: https://aiche.onlinelibrary.wiley.com/doi/pdf/10.1002/aic.690110422.

[45] Xiongewei Ni. A study of fluid dispersion in oscillatory flow through a baffled tube. *Journal of Chemical Technology & Biotechnology*, 64(2):165–174, 1995. _eprint: https://onlinelibrary.wiley.com/doi/pdf/10.1002/jctb.280640209.

[46] Richard F. Molloy and David T. Leighton Jr. Binary oscillatory cross-flow electrophoresis: Theory and experiments. *Journal of Pharmaceutical Sciences*, 87(11):1270–1281, November 1998. Publisher: John Wiley & Sons, Ltd.

[47] Søren Vedel, Laurits Højgaard Olesen, and Henrik Bruus. Pulsatile microfluidics as an analytical tool for determining the dynamic characteristics of microfluidic systems. *Journal of Micromechanics and Microengineering*, 20:035026, March 2010.

[48] Peder Skafte-Pedersen, David Sabourin, Martin Dufva, and Detlef Snakenborg. Multichannel peristaltic pump for microfluidic applications featuring monolithic PDMS inlay. *Lab on a Chip*, 9(20):3003–3006, October 2009. Publisher: The Royal Society of Chemistry.

[49] Y. L. Roht, H. Auradou, J.-P. Hulin, D. Salin, R. Chertcoff, and I. Ippolito. Time dependence and local structure of tracer dispersion in oscillating liquid Hele-Shaw flows. *Physics of Fluids*, 27(10):103602, October 2015. Publisher: American Institute of Physics.

[50] S. Bandyopadhyay and B. S. Mazumder. Unsteady convective diffusion in a pulsatile flow through a channel. *Acta Mechanica*, 134(1):1–16, March 1999.

[51] Aaron M. Thomas and R. Narayanan. Physics of oscillatory flow and its effect on the mass transfer and separation of species. *Physics of Fluids*, 13(4):859–866, March 2001. Publisher: American Institute of Physics.

[52] P. E. Hydon and T. J. Pedley. Axial dispersion in a channel with oscillating walls. *Journal of Fluid Mechanics*, 249:535–555, April 1993. Publisher: Cambridge University Press.

[53] D. R. Scotter and P. a. C. Raats. Dispersion in Porous Mediums Due to Oscillating Flow. *Water Resources Research*, 4(6):1201–1206, 1968. _eprint: https://agupubs.onlinelibrary.wiley.com/doi/pdf/10.1029/WR004i006p01201.

[54] S. B. Hazra, A. S. Gupta, and P. Niyogi. On the dispersion of a solute in oscillating flow of a non-Newtonian fluid in a channel. *Heat and Mass Transfer*, 32(6):481–488, August 1997.

[55] Eirik G. Flekkøy. Symmetry and reversibility in mixing fluids. *Physics of Fluids*, 9(12):3595–3599, December 1997. Publisher: American Institute of Physics.

[56] L. D Landau and Evgenii Mikhailovich Lifshits. *Fluid mechanics, by L.D. Landau and E.M. Lifshitz.* Pergamon Press, London, 1959. OCLC: 225415194.

[57] E. M. Purcell. Life at low Reynolds number. *American Journal of Physics*, 45(1):3–11, January 1977. Publisher: American Association of Physics Teachers.

[58] Mehran Kardar. *Statistical Physics of Particles*. Cambridge University Press, Cambridge, 2007.

[59] N.G.V Kampen. *Stochastic Processes in Physics and Chemistry*. January 2007.

[60] Alex Hansen, Jens Feder, and Eirik Grude Flekkøy. *Flow in Porous Media*. Cambridge University Press, 1. edition.

[61] Eirik G. Flekkøy, Alex Hansen, and Beatrice Baldelli. Hyperballistic superdiffusion and explosive solutions to the non-linear diffusion equation. *arXiv:2012.03748 [cond-mat]*, December 2020. arXiv: 2012.03748.

[62] Hannes Risken and Till Frank. *The Fokker-Planck Equation: Methods of Solution and Applications*. Springer Series in Synergetics. Springer-Verlag, Berlin Heidelberg, 2 edition, 1996.

[63] Roberto Livi and Paolo Politi. *Nonequilibrium Statistical Physics: A Modern Perspective*. Cambridge University Press, Cambridge, 2017.

[64] J. L. Garcia-Palacios. Introduction to the theory of stochastic processes and Brownian motion problems. *arXiv:cond-mat/0701242*, January 2007. arXiv: cond-mat/0701242.

[65] Lars Onsager. Reciprocal Relations in Irreversible Processes. I. *Physical Review*, 37(4):405–426, February 1931. Publisher: American Physical Society.

[66] Michael Shapiro, Itzchak J. Kettner, and Howard Brenner. Transport mechanics and collection of submicrometer particles in fibrous filters. *Journal of Aerosol Science*, 22(6):707–722, January 1991.

[67] Timm Krueger, Halim Kusumaatmaja, Alexandr Kuzmin, Orest Shardt, Goncalo Silva, and Erlend Magnus Viggen. *The Lattice Boltzmann Method: Principles and Practice*. Springer, 2016.

[68] Y. H. Qian, D. Humières, and P. Lallemand. Lattice BGK Models for Navier-Stokes Equation. *Europhysics Letters (EPL)*, 17(6):479–484, February 1992. Publisher: IOP Publishing.

[69] Xiaoyi He, Shiyi Chen, and Gary D. Doolen. A Novel Thermal Model for the Lattice Boltzmann Method in Incompressible Limit. *Journal of Computational Physics*, 146(1):282–300, October 1998.

[70] Mats G. Larson and Fredrik Bengzon. *The Finite Element Method: Theory, Implementation, and Applications*. Texts in Computational Science and Engineering. Springer-Verlag, Berlin Heidelberg, 2013.

[71] Endre Süli and David F. Mayers. *An Introduction to Numerical Analysis*. Cambridge University Press, Cambridge, 2003.

[72] Anders Logg, Kent-Andre Mardal, and Garth Wells, editors. *Automated Solution of Differential Equations by the Finite Element Method*, volume 84 of *Lecture Notes in Computational Science and Engineering*. Springer Berlin Heidelberg, Berlin, Heidelberg, 2012.

[73] Hans Petter Langtangen and Anders Logg. *Solving PDEs in Python*. Springer International Publishing, Cham, 2016.

[74] Gaute Linga. *Fluid Flows with Complex Interfaces: Modelling and Simulation from Pore to Pipe*. PhD thesis, August 2018. Publisher: University of Copenhagen.

[75] Hans Petter Langtangen, Kent-Andre Mardal, and Ragnar Winther. Numerical methods for incompressible viscous flow. *Advances in Water Resources*, 25:1125–1146, August 2002.

[76] Riccardo Mannella and Peter McClintock. Ito versus Stratonovich: 30 years later. *Fluctuation and Noise Letters*, 11, May 2012.

[77] J. M. P. Q. Delgado. A critical review of dispersion in packed beds. *Heat and Mass Transfer*, 42(4):279–310, February 2006.

[78] Charles-Henri Bruneau and Mazen Saad. The 2D lid-driven cavity problem revisited. *Computers & Fluids*, 35(3):326–348, March 2006.

[79] H. K. Moffatt. Viscous and resistive eddies near a sharp corner. *Journal of Fluid Mechanics*, 18(1):1–18, January 1964. Publisher: Cambridge University Press.

[80] Maximilien Levesque, Olivier Bénichou, Raphaël Voituriez, and Benjamin Rotenberg. Taylor Dispersion with Adsorption and Desorption. *Physical Review E*, 86(3):036316, September 2012. arXiv: 1211.5224.

[81] Jens Feder. *Fractals*. Physics of Solids and Liquids. Springer US, 1988.

[82] L. Ponson, D. Bonamy, and E. Bouchaud. Two-Dimensional Scaling Properties of Experimental Fracture Surfaces. *Physical Review Letters*, 96(3):035506, January 2006. Publisher: American Physical Society.

[83] Behzad Ghanbarian, Edmund Perfect, and Hui-Hai Liu. A geometrical aperture–width relationship for rock fractures. *Fractals*, 27(01):1940002, August 2018. Publisher: World Scientific Publishing Co.

[84] H. Xia, N. Francois, H. Punzmann, and M. Shats. Taylor Particle Dispersion during Transition to Fully Developed Two-Dimensional Turbulence. *Physical Review Letters*, 112(10):104501, March 2014. Publisher: American Physical Society.

[85] Christopher Hawkins, Luiza Angheluta, Marcin Krotkiewski, and Bjørn Jamtveit. Reynolds-number dependence of the longitudinal dispersion in turbulent pipe flow. *Physical Review E*, 93(4):043119, April 2016. Publisher: American Physical Society.

[86] Geoffrey Ingram Taylor. The dispersion of matter in turbulent flow through a pipe. *Proceedings of the Royal Society of London. Series A. Mathematical and Physical Sciences*, 223(1155):446–468, May 1954. Publisher: Royal Society.

[87] Robert J. Twiss, Gretchen M. Protzman, and Stephen D. Hurst. Theory of slickenline patterns based on the velocity gradient tensor and microrotation. *Tectonophysics*, 186(3):215–239, February 1991.

[88] Laurie E. Locascio. Microfluidic mixing. *Analytical and Bioanalytical Chemistry*, 379(3):325–327, June 2004.

[89] Sang H. Lee and Peter K. Kang. Three-Dimensional Vortex-Induced Reaction Hot Spots at Flow Intersections. *Physical Review Letters*, 124(14):144501, April 2020. Publisher: American Physical Society.

[90] Seung Hyun Lee, In Wook Yeo, Kang-Kun Lee, and Russell L. Detwiler. Tail shortening with developing eddies in a rough-walled rock fracture. *Geophysical Research Letters*, 42(15):6340–6347, 2015. _eprint: https://agupubs.onlinelibrary.wiley.com/doi/pdf/10.1002/2015GL065116.

[91] Carl M. Bender and Steven A. Orszag. *Advanced Mathematical Methods for Scientists and Engineers I: Asymptotic Methods and Perturbation Theory*. Bender,C.M.;Orszag,S.A.: Adv.Math.Methods Scientists,Eng. Springer-Verlag, New York, 1999.

[92] D. A. Edwards, M. Shapiro, H. Brenner, and M. Shapira. Dispersion of inert solutes in spatially periodic, two-dimensional model porous media. *Transport in Porous Media*, 6(4):337–358, August 1991.

[93] Evelyn Tang and Ramin Golestanian. Quantifying configurational information for a stochastic particle in a flow-field. *New Journal of Physics*, 22(8):083060, August 2020. Publisher: IOP Publishing.

[94] Joris Heyman, Daniel R. Lester, Régis Turuban, Yves Méheust, and Tanguy Le Borgne. Stretching and folding sustain microscale chemical gradients in porous media. *Proceedings of the National Academy of Sciences*, 117(24):13359–13365, June 2020. Publisher: National Academy of Sciences Section: Physical Sciences.

[95] Yanina Lucrecia Roht, Ricardo Chertcoff, Jean-Pierre Hulin, Harold Auradou, and Irene Ippolito. Reversible and Irreversible Tracer Dispersion in an Oscillating Flow Inside a Model Rough Fracture. *Transport in Porous Media*, 122(2):421–436, March 2018.